

ALMA MATER STUDIORUM - UNIVERSITÀ DI BOLOGNA

FACOLTÀ DI SCIENZE MATEMATICHE FISICHE E NATURALI

DOTTORATO DI RICERCA IN FISICA
XXII CICLO

Study of diffuse flux of high energy neutrinos through showers with the ANTARES neutrino telescope

Author: **Giada Carminati**

Ph.D. Coordinator:
Prof. Fabio Ortolani

Promoter:
Prof. Maurizio Spurio

Bologna - May 4th 2010

A mia zia Lia

E quindi uscimmo a riveder le stelle.
Dante Alighieri (Inferno - Canto XXXIV)

Contents

Introduction	5
1 High Energy Astronomy	9
1.1 Composition and Energy Spectrum of Cosmic Rays	10
1.1.1 The GZK Cutoff	12
1.2 Production of Gamma-Rays and Neutrinos	13
1.3 Origin of the Bulk of Cosmic Rays	15
1.3.1 Shock Acceleration and Supernova Explosion	16
1.3.2 Candidate Galactic Neutrino Sources	17
1.4 Origin of Ultra High Energy Cosmic Rays	18
1.4.1 Acceleration Scenarios and Source Candidates	18
1.4.2 Decay Scenario	20
1.4.3 Cosmogenic Neutrinos	22
2 The ANTARES neutrino telescope	23
2.1 Cherenkov Radiation	24
2.2 Detector Layout	25
2.3 Detector Status	29
2.4 Detector Acquisition	30
2.4.1 Signal Digitization	30
2.4.2 Data Transmission	31
2.4.3 Data filtering and storage	32
2.5 Detector Calibration	32
2.5.1 Time Calibration	32
2.5.2 Charge Calibration	33
2.5.3 Position Calibration	34
2.6 Optical Background	36

3	Parameterization of Atmospheric Muons	39
3.1	Cosmic Ray Interaction with the Earth's Atmosphere	39
3.2	Primary Cosmic Ray Models	42
3.3	Parametric Formulae of Underwater Muons	45
3.3.1	Muon Energy Loss in Water	46
3.3.2	Flux of Muon Bundles	47
3.3.3	Energy Spectrum	47
3.3.4	Lateral Spread	49
3.3.5	Multiplicity	50
3.4	Comparison of Parametric Formulae with Experimental Data	50
4	The Simulation of Underwater Atmospheric Muons: MUPAGE	53
4.1	Program Structure	53
4.2	Generation of Muon Bundles on the Can Surface	56
4.2.1	Sampling of the Bundle Direction and of the Impact Point	56
4.2.2	Hit-or-Miss Method to Sample the Impact Point	58
4.3	Single Muons	59
4.4	Multiple Muons	60
4.4.1	Radial Distance of Muons with Respect to the Bundle Axis	60
4.4.2	Coordinates of the Multiple Muons on the Can Surface	60
4.4.3	Arrival Time of the Muons in the Bundle	62
4.4.4	Muon Energy for MultimMuon Events	63
4.5	Livetime of the Simulation	63
4.6	Comparison of Angular Distributions with ANTARES data	64
5	Ultra High Energy Neutrinos	67
5.1	Atmospheric Neutrinos	68
5.2	Diffuse Neutrino Flux	69
5.3	Neutrino Oscillation Effects on the Diffuse Neutrino Flux	70
5.4	Neutrino Interactions	72
5.5	Earth's Opacity to Neutrinos	74
6	Diffuse Neutrino Flux Analysis	77
6.1	Monte Carlo Samples	77
6.1.1	Atmospheric Muons	78
6.1.2	Atmospheric CC Muon Neutrinos	78

6.1.3	CC Electron Neutrinos	80
6.1.4	NC Neutrinos	83
6.2	Rejection of the Background Signal	83
6.2.1	Number of lines	84
6.2.2	Fit Quality Parameters	84
6.2.3	Amplitude	85
6.2.4	Summary of the Selection Criteria	87
6.3	Comparison between Monte Carlo Atmospheric Muons and Data	88
6.4	Efficiencies and Purities of the Selection Criteria	89
7	Sensitivity to the Diffuse Neutrino Flux through Showers	91
7.1	Diffuse Neutrino Flux Sensitivity	91
7.2	The Real Detector	93
7.3	Monte Carlo Samples for Different ANTARES Setups	94
7.3.1	9Line Configuration	94
7.3.2	10Line Configuration	95
7.4	Diffuse Neutrino Flux Analysis for Different Setups	95
7.5	Conclusion and Outlook	98
A	ANTARES Analysis Chain	101
A.1	Monte Carlo Event Generators	101
A.1.1	MUPAGE	101
A.1.2	Genhen	102
A.2	Cherenkov Light Production and Detector Simulation	103
A.2.1	KM3	103
A.2.2	Geasim	103
A.3	Trigger Selection	104
A.4	Reconstruction Algorithm	105
A.4.1	Fitting Procedure	106
A.4.1.1	Particle Track	106
A.4.1.2	Bright Point	107
A.4.1.3	Fit Function	108
A.4.1.4	Minimization Procedure	109
A.4.2	Event Display	109
	References	113

Summary

119

Introduction

Astronomy, with several thousand years of history, is one of the oldest of the natural sciences. Most of our knowledge of the Universe comes from the observations of the photons through the entire electromagnetic spectrum. However, the ultra high energy domain remains largely unexplored by conventional astronomical methods, because gamma-ray astronomy observations are limited by the high energy photon interactions with the 2.7 K cosmic microwave background radiation. As a result, the Universe is opaque to gamma-rays from extragalactic sources; photons with energy higher than 10^6 GeV cannot even survive the journey from the Galactic Center to the Earth.

On the contrary, the observation of high energy neutrinos may help to explain the dynamics of the most energetic phenomena that occur in the Universe. Due to their nature (weakly interacting and neutral charge), neutrinos can escape from hot dense sources without being absorbed during their propagation to the Earth or deflected by extragalactic, galactic and geo-magnetic fields. Therefore, neutrinos act as cosmic messengers which point straight back to their source and may identify extragalactic and galactic sources of cosmic rays. However, due to their small interaction cross sections, a large target mass is essential to detect them. For this reason cosmic neutrino detectors employ enormous volumes of natural material such as deep seawater or ice.

A neutrino telescope such as ANTARES can be considered as a fixed target experiment: A cosmic muon neutrino produced in a cosmic source (Supernova Remnants, Active Galactic Nuclei, Gamma-Ray Bursts, ...) which arrives from the hemisphere opposite to the detector location, crosses the Earth and interacts by a charged current process with a nucleon of the medium surrounding the telescope and induces a muon. Above a few TeV, the neutrino-induced upward going muon is (almost) collinear with the incident neutrino and can travel up to 10 km before reaching the detector. The Cherenkov light emitted by the muon with an angle $\theta_C \simeq 42^\circ$ in deep seawater or ice is detected by a three-dimensional array of photomultiplier tubes (PMTs). The ANTARES detector, located in the Mediterranean Sea approximately 40 km offshore Toulon (France), comprises 885 PMTs placed

on 12 flexible strings anchored to the seabed and kept vertical by buoys.

Neutrino telescopes are optimized to detect neutrino-induced muons, and most of the studies conducted so far have focussed on muon reconstruction to discover the cosmic sources which emit neutrinos. However, the detection of electron neutrinos as well as all-flavor neutrinos produced by neutral current interactions is also possible. These events are characterized by showers: Electromagnetic showers are generated from secondary electrons in the charged current reactions of electron neutrinos, while hadronic showers are produced in all-flavor neutral current reactions.

Through the detection of showers, a search for the integrated contribution from all neutrino sources, which may produce a diffuse high energy neutrino flux, can be done. The only way to detect this diffuse flux of high energy neutrinos is to look for an excess of high energy events in the measured energy spectrum induced by atmospheric neutrinos.

Nevertheless, the most abundant signal seen by a neutrino telescope is due to high energy downward going muons produced in the extensive air showers resulting from interactions between cosmic rays and atmospheric nuclei. Although the shielding effect of the sea reduces their flux, at the ANTARES site the atmospheric muon flux is about six orders of magnitude larger than the atmospheric neutrino flux. Therefore, atmospheric muons represent a dangerous background in the search for neutrino events.

This thesis presents a Monte Carlo event generator to simulate underwater/ice atmospheric muons, known as the MUPAGE code. Based on parametric formulae which permit to save computing time with respect to a full Monte Carlo generation, MUPAGE produces the muon event kinematics on the surface of a virtual cylinder surrounding the active volume of a generic underwater/ice neutrino telescope. The generated output file can subsequently be used as input in the following steps of a detector-dependent Monte Carlo simulation, which includes production of Cherenkov light in water/ice and simulation of the signal in the detection devices.

Using MUPAGE, a Monte Carlo simulation of atmospheric muons corresponding to an active detector time of 1 year is used to optimize selection criteria to distinguish cosmic neutrino-induced showers from the background. This novel technique, presented for the first time in this thesis, takes advantage of the different topology of shower events with respect to muon tracks. The spatial extension of the Cherenkov light emitted by hadronic and electromagnetic showers is significantly smaller than the typical size of the detector, hence the showers can be considered as point-like light sources. On the other hand, a particle track is considered as a straight line in space. Rejecting all the signal due to muon tracks induced by atmospheric muons and by atmospheric muon neutrinos, this technique

permits to estimate the sensitivity of the ANTARES detector to the diffuse flux of high energy (anti-)electron neutrinos.

This thesis is organized as follows. Chapter 1 discusses an overview of the knowledge of cosmic rays as well as the mechanisms for their production in candidate sources. Chapter 2 presents the ANTARES neutrino telescope. Chapter 3 starts with a brief description of the interaction of cosmic rays with the atmospheric nuclei and the subsequent creation and propagation of secondary particles through the atmosphere. This is followed by the parameterization of underwater/ice atmospheric muons, which considers also the contribution of multiple muons in a bundle. The details of the MUPAGE code, the Monte Carlo event generator of underwater/ice atmospheric muons derived from these formulae, are described in Chapter 4. Chapter 5 discusses an overview of high energy neutrino interactions and the propagation through the Earth, introducing the theoretical models which describe the atmospheric neutrino as well as the cosmic neutrino flux. Chapter 6 presents the diffuse neutrino flux analysis, describing the Monte Carlo data sample used to define the selection criteria for the rejection of the background signal. To conclude, in Chapter 7 the sensitivity to the diffuse electron neutrino flux of the ANTARES detector is estimated and an outlook for further developments is given.

Chapter 1

High Energy Astronomy

High energy astronomy derived from the fundamental necessity of extending conventional astronomy beyond the optical and, more in general, electromagnetic messengers. Also known as astroparticle physics, this relatively young field of astronomy opens a new window on the Universe, focussing on high energy cosmic rays, gamma-rays, gravitational waves and neutrinos.

Neutrinos are of particular interest because they only interact through the weak nuclear force. Hence they can cross long distances and penetrate regions which are opaque to photons. Furthermore, due to their neutral electric charge, they are not deflected by any magnetic fields in the Universe, and therefore point straight back to their source. Thus neutrinos act as cosmic messengers which can provide information on the dynamics of the most energetic phenomena of the Universe and possibly the identification of cosmic ray sources.

However, the small interaction cross section of neutrinos requires a large target mass to detect them. This is the reason why cosmic neutrino detectors employ enormous volumes of natural material such as deep seawater or ice. After a pioneering paper published by Markov [1] half a century ago, the technology is finally in place for neutrino astronomy to become a reality.

The main results concerning the composition and energy spectrum of cosmic rays are presented in § 1.1. § 1.2 discusses the production of gamma-rays and neutrinos in astrophysical objects. Acceleration models and candidate cosmic ray and neutrino sources are described in § 1.3 and § 1.4, divided in two ranges of energy: up to and above 100 TeV respectively.

1.1 Composition and Energy Spectrum of Cosmic Rays

The Earth's exposure to radiation from space was discovered in 1912 by Hess¹. In the following decades, cosmic rays were studied with balloon experiments and later with satellites. However, with increasing energy, the cosmic radiation arrives too infrequent to be detected directly by the small detectors carried in balloons or spacecraft. In 1938 Pierre Auger constructed a ground-based experiment discovering extensive air showers, caused by the interaction of high energy charged particles with the atmosphere. The energy contained in these showers turned out to be several orders of magnitude higher than the energy of the cosmic rays measured with balloons. Cosmic ray experiments have therefore been built on larger and larger scales, in order to detect particles at the highest energies.

The cosmic radiation incident at the top of the terrestrial atmosphere is composed of all stable charged particles and nuclei. Technically, *primary* cosmic rays refer to those particles accelerated at astrophysical sources, and *secondaries* refer to those particles produced by spallation of primaries with interstellar gas. Thus, electrons, protons and nuclei synthesized in stars (such as He, C, O, Fe) are primaries. Nuclei such as Li, Be and B are secondaries. Antiprotons and positrons are also in large part secondary. About 79% of the primaries are free protons and about 70% of the rest are helium nuclei [2].

Apart from particles associated with solar flares, the cosmic radiation originates outside the solar system. The incoming charged particles are 'modulated' by the solar wind which decelerates and partially excludes the lower energy extrasolar cosmic rays from the inner solar system. There is a significant anticorrelation between solar activity (which has an alternating eleven-year cycle) and the intensity of the cosmic rays with energies below about 10 GeV. In addition, the lower energy cosmic rays are affected by the geomagnetic field, which they must penetrate to reach the top of the atmosphere. Thus the intensity of any component of the cosmic radiation in the GeV range depends both on location and time.

The cosmic ray spectrum extends over 13 orders of magnitude, from about 10^8 eV up to roughly 10^{21} eV. With increasing energy, the flux decreases: at 10^{11} eV, one particle $\text{m}^{-2} \text{s}^{-1}$ bombards the atmosphere; the flux at 10^{15} eV is only one particle $\text{m}^{-2} \text{year}^{-1}$. At energies higher than 10^{20} eV, the flux is only one particle $\text{km}^{-2} \text{century}^{-1}$.

The lowest energy cosmic rays are detected directly by experiments on board of satellites or high altitude balloons before they are absorbed in the atmosphere. High energy cosmic rays however are detected indirectly through the extensive air showers by an array

¹Victor Franz Hess was awarded the Nobel Prize for his discovery of cosmic radiation in 1936.

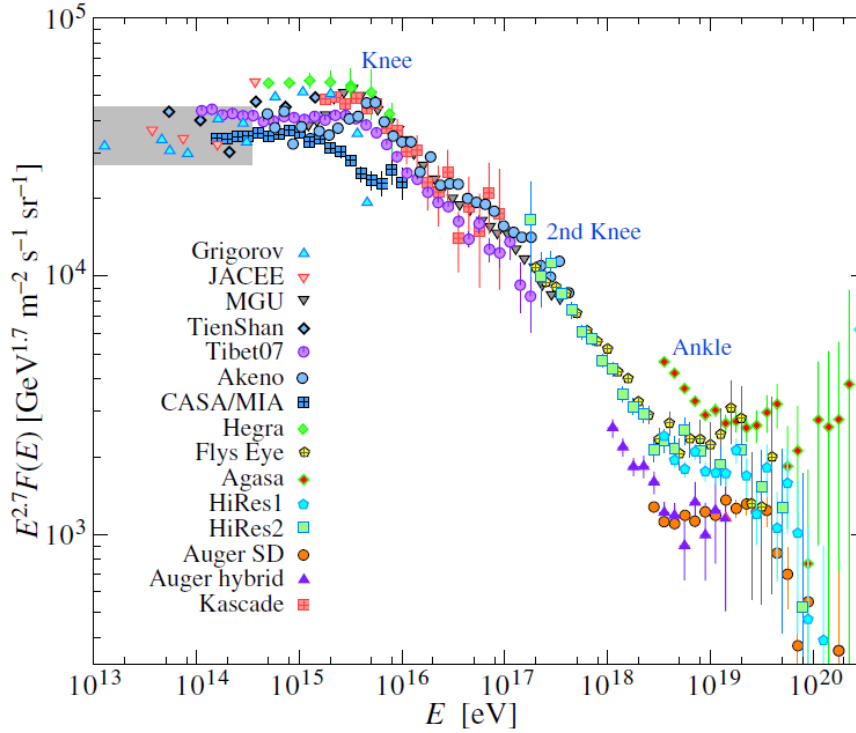


Figure 1.1: The all-particle spectrum from air shower measurements. The shaded area shows the range of the direct cosmic ray spectrum measurements. Figure taken from [2].

of particle detectors at ground level.

Figure 1.1 shows the measured all-particle spectrum for energies above 10^{13} eV. The flux has been multiplied by $E^{2.7}$ in order to display the features of the steep spectrum that are otherwise difficult to discern.

Above 10 GeV, the flux of the all-particle spectrum is well described by a broken power-law,

$$\frac{dN}{dE} \propto E^{-\gamma} \quad (1.1)$$

where N is the number of observed events, E the energy of the primary particle and γ is the spectral index. The spectral index is about 2.7 up to 3×10^{15} eV. Above this energy, the spectral index steepens to about 3.1, introducing the feature known as the *knee* of the spectrum. The feature around 10^{19} eV is called the *ankle* of the spectrum and above this energy the spectral index is again about 2.7.

The change in the slope in the knee region can be explained phenomenologically by assigning a cutoff energy to the cosmic ray components. This also explains why at around 4×10^{17} eV, the slope becomes even steeper at the so-called *second knee*. For relativistic nuclei with electric charge Ze and energy E in a magnetic field B , the gyroradius is given

by the Larmor radius $R_L = E/ZeB$. The propagation of cosmic rays in the Galaxy is described by the Leaky Box model [3]. In the galactic magnetic field, protons with energy up to 10^{18} eV have a Larmor radius which is smaller than the size of the Galaxy and can remain confined. Up to these energies, cosmic rays are therefore thought to have a galactic origin, while at higher energies they can escape from the Galaxy. Heavier nuclei have larger charges and must therefore be accelerated to larger energies to achieve the same Larmor radius than protons. Consequently, the heavier element cutoff lies at higher energies and the composition of cosmic rays for energies above the knee shows a domination of heavier nuclei over the protons.

Concerning the ankle region, one possible explanation of the flattening of the spectrum could be the result of higher energy population of particles overtaking a lower energy population, e.g. an extragalactic flux which starts to dominate over the galactic flux [4]. Furthermore, dimensional analysis related to the Larmor radius and to the fact that, given the microgauss magnetic field of our Galaxy, no structures are large or massive enough to reach the energies of the highest energy cosmic rays, limits their sources to extragalactic objects [5].

1.1.1 The GZK Cutoff

In the highest energy region, not only deflection by the intergalactic magnetic field, but also the energy losses of cosmic rays in the intergalactic radiation fields, such as microwave, infrared and radio backgrounds, become important. Soon after the discovery of the Cosmic Microwave Background radiation (CMB) [6], Greisen [7], Zatsepin and Kuz'min [8] independently predicted that there would be a cutoff in the spectrum of protons around 6×10^{19} eV due to photo-production of pions due to interactions with the photons of the CMB. This phenomenon, known as the GZK cutoff, also limits the possible distance of any source to several tens of Mpc, the so-called GZK zone.

If cosmic rays are of extragalactic origin, their expected arrival direction distribution is isotropic for energies below the GZK cutoff. But when their energies exceed the GZK cutoff energy, the cosmic rays are hardly deflected by the intergalactic and/or galactic magnetic field, and their arrival directions should point back to their sources in the sky, if the sources are within the GZK zone. Thus a correlation of their arrival directions with the galactic structure and/or the larger scale of galaxy clusters may be expected [9]. The Pierre Auger Collaboration reported [10] a correlation of the arrival directions of cosmic rays with energies exceeding 6×10^{19} eV with the positions of nearby Active Galactic Nuclei (AGN) at distances smaller than 75 Mpc. Although this result suggests an anisotropy in the arrival

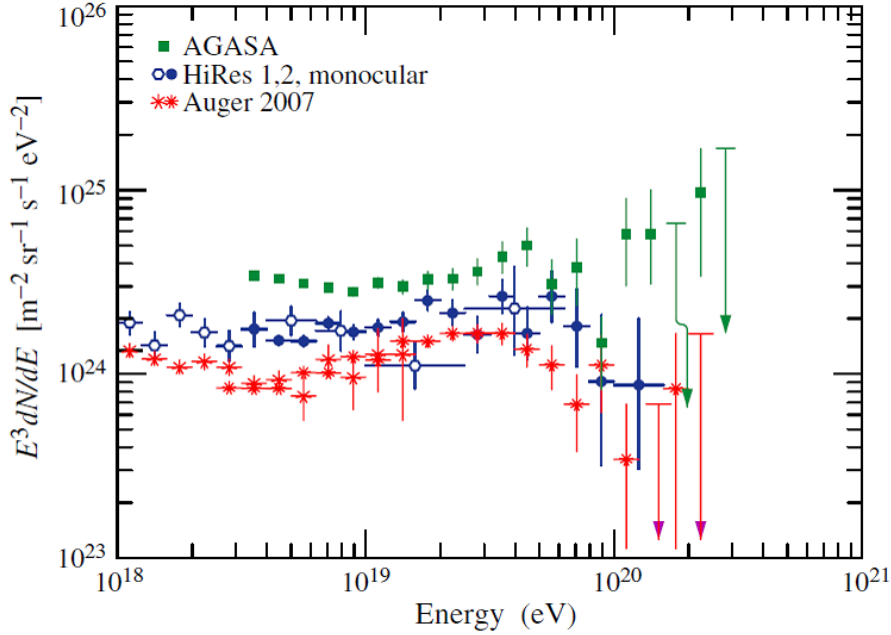


Figure 1.2: Expanded view of the high energy end of the cosmic ray spectrum. The most recent measurements from AGASA [11], HiRes [12] and Auger [13] are shown. Figure taken from [2].

directions of the cosmic rays, it does not unambiguously identify AGN as the sources of cosmic rays. Furthermore, it is not confirmed by the other ground-based array experiments such as HiRes.

Although several experiments have detected cosmic rays above 10^{20} eV, the spectral shape above the ankle is not well determined. The AGASA experiment [11] claimed 11 events above 10^{20} eV, while the HiRes [12] and Auger [13] spectra show a significant steepening of the cosmic ray spectrum above 4×10^{19} eV, which is consistent with the prediction of the GZK cutoff.

Figure 1.2 gives an expanded view of the high energy end of the spectrum, showing the results of the three of ground-based experiments. This figure shows the differential flux multiplied by a power of the energy, a procedure that enables one to see structure in the spectrum more clearly, but amplifies small systematic differences in energy assignments into sizable normalization differences.

1.2 Production of Gamma-Rays and Neutrinos

In general, the acceleration of charged particles by astrophysical sources is described by two models. The model which describes acceleration of electrons is the so-called *lep-*

tonic model [14]. Acceleration of protons or other nuclei is described by the so-called *hadronic model* [5]. An adequate description of the current experimental situation concerning gamma-rays can be provided by both models [15]. Since neutrinos are only produced in the hadronic model, only this model will be discussed.

In the hadronic model, high energy neutrinos and gamma-rays are produced in the decay of pions which are created in collisions of energetic protons with dense matter or photon fields.

Accelerated protons interact with photons in the surrounding of the cosmic ray emitters predominantly via the Δ^+ resonance:

$$p + \gamma \rightarrow \Delta^+ \rightarrow \pi^0 + X \quad (1.2a)$$

$$p + \gamma \rightarrow \Delta^+ \rightarrow \pi^\pm + X \quad (1.2b)$$

Protons can also interact with ambient matter (other protons, neutrons and nuclei), giving rise to the production of charged and neutral mesons:

$$p + p \rightarrow \pi^0 + X \quad (1.3a)$$

$$p + p \rightarrow \pi^\pm + X \quad (1.3b)$$

Neutral pions decay into photons (observed at Earth as γ -rays) with a probability of almost 98.8%:

$$\pi^0 \rightarrow \gamma\gamma \quad (1.4)$$

Charged pions decay into neutrinos with almost 100% probability:

$$\begin{aligned} \pi^+ &\rightarrow \nu_\mu + \mu^+ \\ &\quad \hookrightarrow \bar{\nu}_\mu + \nu_e + e^+ \end{aligned} \quad (1.5a)$$

$$\begin{aligned} \pi^- &\rightarrow \bar{\nu}_\mu + \mu^- \\ &\quad \hookrightarrow \nu_\mu + \bar{\nu}_e + e^- \end{aligned} \quad (1.5b)$$

Therefore, in the framework of the hadronic model and in the case of *transparent sources*, the energy escaping from the sources is distributed between cosmic rays, γ -rays and neutrinos. A source is referred to as transparent if its size is larger than the proton mean free path, but smaller than the meson decay length. For these sources, protons have large probability of interacting once, and most secondary mesons can decay.

Since the cosmic ray acceleration mechanism also produces neutrinos and high energy photons, γ -ray sources are in general also candidates for neutrino sources. In the hadronic

model, the spectral indices of the cosmic ray energy spectrum and the γ -ray and neutrino spectra are related. It is expected [16] that for nearby sources, they are almost identical. Hence, γ -ray measurements provide crucial information about primary cosmic rays, and they constrain the expected neutrino flux.

1.3 Origin of the Bulk of Cosmic Rays

After one century of research, the question of the origin of cosmic rays continues to be regarded as an unsolved problem. Although the general aspects of the origin of cosmic rays are considered fairly well-understood, major gaps and uncertainties remain. In general, the level of uncertainty increases with the cosmic ray energy.

One of the difficulties to distinguish among the various possible scenarios is due to the fact that the cosmic ray nuclei do not travel in straight lines, but are diffused by the tangled magnetic fields in the Galaxy. Since cosmic rays with energy below 10^{20} eV do not point back to their sources it is impossible to identify the sources in this way. However, for the majority of the cosmic rays (i.e. those with energy from 1 to 10^5 GeV per nucleon) many aspects concerning the origin can be understood in terms of shock acceleration and diffusive propagation in turbulent magnetic fields in the Galaxy.

The presence in the cosmic radiation of a much greater proportion of secondary nuclei as spallation products of the abundant primary nuclei, implies that cosmic rays travel distances thousands of times greater than the thickness of the galactic disk during their lifetime. This suggests diffusion in a containment volume that includes some or all of the galactic disk. The fact that the amount of matter traversed decreases as energy increases suggests that the highest energy cosmic rays spend less time in the Galaxy than the lowest energy ones. It also suggests that cosmic rays are accelerated before most propagation occurs. If, on the contrary, acceleration and propagation occurred together, one would expect a constant ratio of secondary/primary cosmic rays.

Nevertheless, acceleration and transport of cosmic rays are expected to be closely related. In particular, in the shock acceleration model by supernova blast waves, diffusive scattering of particles by irregularities in the magnetic field plays a crucial role in the acceleration as well as the propagation process. Moreover, since acceleration occurs as the supernova remnant expands into the interstellar medium, there is no sharp division between acceleration and propagation.

1.3.1 Shock Acceleration and Supernova Explosion

The basic idea of the statistic acceleration mechanism is to transfer macroscopic kinetic energy of moving magnetized plasma to individual charged particles in the medium due to repeated collisionless scattering (*encounters*). Although in each individual encounter the particle may either gain or lose energy, there is an average net gain of energy after multiple encounters. Thereby the energy particle is increased significantly and the non-thermal energy distribution characteristic of particle acceleration is achieved.

In the original paper proposed by Fermi in 1949 [17], charged particles collide with moving clouds of plasma and begin to diffuse by scattering on the irregularities in the magnetic field. However, this mechanism, nowadays referred to as the second-order Fermi mechanism, is not a very efficient acceleration process because the average fractional energy gain is proportional to $(u/c)^2$, where u is the relative velocity of the cloud with respect to the frame in which the cosmic ray ensemble is isotropic, and c is the light speed.

A more efficient version of the Fermi mechanism is realized when encounters of particles with plane shock fronts are considered. In this case, the average fractional energy gain of a particle per encounter is of the first order in the relative velocity between the shock front and the isotropic cosmic ray front. Currently, the ‘standard’ theory of cosmic ray acceleration – the so-called Diffusive Shock Acceleration Mechanism (DSAM) – is therefore based on the first-order Fermi acceleration mechanism. An important feature of DSAM is that particles emerge out of the acceleration site with a characteristic power-law spectrum with a spectral index that depends only on the shock compression ratio, and not on the shock velocity.

The ejected material from a supernova explosion moves out through the interstellar medium in the form of shock waves at which acceleration can occur. The acceleration hypothesis is motivated by the fact that the power release in supernovae is about 2×10^{35} W. The total power required to supply all the galactic cosmic rays is about 5×10^{33} W. Even if there are large uncertainties in these numbers, it appears plausible that an efficiency of few per cent would be enough for supernova blast waves to energize all the galactic cosmic rays.

The finite lifetime of the supernova blast wave as a strong shock, however, limits the maximum energy per particle than can be achieved with this mechanism. For a supernova with a typical size of 5 pc, the maximum energy is about 10^4 GeV per nucleus. Thus, since the maximum achieved energy is proportional to the charge per nucleus, according to this acceleration mechanism the cosmic ray composition becomes progressively enriched

in heavier nuclei as energy increases beyond the knee region.

The case for supernova explosions as the powerhouse for cosmic rays becomes stronger with the realization that the first-order Fermi acceleration naturally produces a spectrum of cosmic rays close to what is observed. Nevertheless the measured spectral index ($\gamma \sim 2.7$) is steeper than the source spectrum ($\gamma \sim 2$), because of the energy dependence of cosmic ray diffusion out of the Galaxy, according to their gyromagnetic radii.

The steepening of the spectrum in the knee region is explained by the end-point of this kind of acceleration mechanism. To conclude, this model explains a large part of the spectrum observed from the Earth.

1.3.2 Candidate Galactic Neutrino Sources

The operation of second-generation Imaging Air Cherenkov Technique (IACT) Telescopes, such as H.E.S.S. [18], VERITAS [19] and MAGIC [20], disclosed the very high energy gamma-ray sky, revealing a large number of TeV γ -ray sources. Galactic TeV sources are mainly associated with SuperNova Remnants (SNRs) and X-Ray Binaries, as well as and with their jetty subclasses: Pulsar Wind Nebulae (PWN) and microquasars [21]. In particular, SNRs and microquasars show peculiar TeV γ -ray emissions that suggest interactions of accelerated protons on dense media or local radiation fields, that could also produce TeV neutrino fluxes [22].

A phenomenological approach [23] determines the cosmic ray flux accelerated by SNRs, required to produce the observed TeV γ -ray flux in the hadronic scenario. In this approach, interactions between cosmic ray protons and ambient hydrogen clouds result in the production of mesons which subsequently decay producing photons and neutrinos. Since both γ -ray and neutrino fluxes depend linearly on the flux of primary cosmic rays, there is also a linear relation between the γ -ray and the neutrino flux (with a factor of about 2 for neutrinos, as the photo-production of pions gives the same amounts of π^+ , π^- and π^0).

If the energy content of the galactic microquasar jets is dominated by electron-proton plasma, there is the possibility [24] that protons, accelerated at energies larger than 100 TeV by internal shocks within the microquasar jets themselves, could produce TeV neutrino fluxes through photo-meson interactions with ambient X-ray radiation. Depending on source parameters, the expected neutrino flux range [25] is $\Phi_\nu \simeq 10^{-12} \div 10^{-10}$ $\text{TeV}^{-1} \text{ cm}^{-2} \text{ s}^{-1} \text{ sr}^{-1}$.

1.4 Origin of Ultra High Energy Cosmic Rays

The simplest set of assumptions for particle acceleration in the form of DSAM (§ 1.3.1) does not disclose the origin of cosmic rays with energies greater than roughly 10^{17} eV. For these Ultra High Energy Cosmic Rays (UHECRs), one has to invoke shocks on larger scales, namely extragalactic shocks. This acceleration scenario is referred to as the *bottom-up* scenario. In order to trivially solve the problem of maximum energy achievable, a non-acceleration mechanism is also possible, referred to as the *top-down* decay scenario.

In the bottom-up scenario, charged particles are accelerated from lower energies to the required energies in certain special astrophysical environments. Examples are acceleration in shocks associated with SNRs, AGN, powerful radio-galaxies, and so on, or acceleration in the strong electric fields generated by rotating neutron stars with high surface magnetic fields. On the other hand, in the top-down scenario energetic particles simply arise from the decay of certain sufficiently massive particles originating from physical processes in the early Universe, and no acceleration mechanism is invoked at all.

1.4.1 Acceleration Scenarios and Source Candidates

In one possible bottom-up scenario, the supernova blast wave mechanism itself may actually give energies higher than 10^{17} eV. Particles could be accelerated by interactions with multiple SNRs as they move through the interstellar medium. Moreover, supernovae probably do not occur in the average interstellar medium. A notable example is Supernova 1987A, which exploded into an environment formed by the wind of its progenitor. This could raise the maximum energy limit by one or two orders of magnitude [26].

Irrespective of the acceleration mechanism taken into account, a simple dimensional argument was given by Hillas [27], which allows one to restrict attention to only a few classes of astrophysical objects as possible sources capable of accelerating particles to a given energy. In any acceleration scenario, there must be a magnetic field B to keep the particles confined within the acceleration site. Thus, the size R of the acceleration region must be larger than the diameter of the orbit of the particle. This argument shows that to achieve a given maximum energy, the acceleration site must have either a large magnetic field or a large size (Figure 1.3). Thus, only a few astrophysical sources such as AGN, radio-galaxies and pulsars satisfy the conditions necessary for acceleration up to 10^{20} eV.

Estimates of the typical values of R and B for the central regions of AGN give $R \sim 0.02$ pc and $B \sim 5$ G. These values yield a cutoff energy of approximately 10^{19} eV for protons. However, the energy of accelerated protons is severely degraded due to the photo-

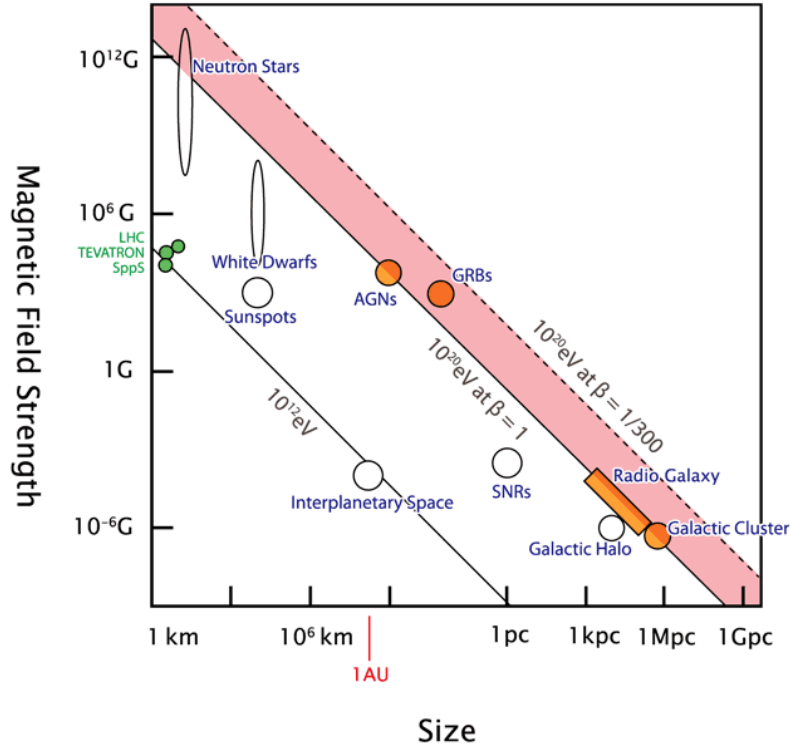


Figure 1.3: Hillas Diagram: Theoretical upper limits of the energy of the particle are determined by the size and strength of celestial objects.

pion production in interactions with the intense radiation field in and around the central engine of the AGN. In addition, there are energy losses due to synchrotron and Compton processes. So neither protons nor heavy nuclei are likely to escape from the central regions of AGN with such extremely high energies. Nevertheless, the associated ultrahigh energy neutrinos from the pion decay can escape from AGN cores. The integrated contribution from all AGN may then produce a diffuse high energy neutrino flux that may be detectable with a neutrino telescope [28].

The only way to detect this diffuse flux of high energy neutrinos is to look for an excess of high energy events in the measured energy spectrum induced by atmospheric neutrinos. It has been pointed out by Waxman and Bahcall [29] that a comparison from the observations of the diffuse flux of γ -rays and UHECRs leads to an upper bound on the diffuse neutrino flux of

$$E_\nu^2 \Phi_\nu < 4.5 \times 10^{-8} \text{ GeV cm}^{-2} \text{ s}^{-1} \text{ sr}^{-1} \quad (1.6)$$

More details about the Waxman-Bahcall upper limit are given in § 5.2.

Other promising acceleration sites for UHECRs [30] are the so-called hot-spots of

Fanaroff-Riley type II radio-galaxies [31]. The hot-spot is interpreted as a gigantic shock wave injected by jets emanating from a central active galactic nucleus at relativistic speeds. The energy loss due to photo-pion production at the source is not significant at hot-spots because the density of the ambient soft photons is thought to be relatively small. Depending on the magnetic field strength, a maximum energy of up to 10^{21} eV seems to be possible. However, it seems difficult to invoke the radio-galaxies as sources of the observed Extremely High Energy Cosmic Rays (EHECRs) above 10^{20} eV, due to their large cosmological distances (> 100 Mpc) from Earth and the GZK effect.

Acceleration to extremely high energy near the event horizons of spinning supermassive black holes associated with presently inactive quasar remnants has been suggested by Boldt and Ghosh [32]. The required effective electromotive force would be generated by black-hole-induced rotation of externally supplied magnetic field lines threading the horizon.

Another type of sources are gamma-ray bursts (GRBs) which are very short, typically tens of seconds long, intense flashes of MeV gamma-rays. Various models have been proposed in order to describe what causes these apparent explosions and which processes take place during the explosion that leads to the observations. A comprehensive review is reported in [33]. On the basis of energetics and dynamical considerations, GRBs were suggested to be UHECR sources [34] via a Fermi mechanism occurring in internal shocks.

GRBs are expected to emit neutrinos during several stages of their evolution [35]. Since GRB neutrino events are correlated both in time and in direction with γ -rays, their detection is practically background free. A neutrino telescope, triggered by satellite alerts, could therefore detect them.

Other candidates, motivated by radio observations, are starburst galaxies, common throughout the Universe, where an exceptionally high rate of star formation has been observed. The high rate of supernova explosions expected in these regions could enrich the ambient gas with highly relativistic electrons and protons that interact with the interstellar medium. Such hidden accelerators of cosmic rays could represent pure high energy neutrino injectors. A cumulative flux of $E_\nu^2 \Phi_\nu < 2 \times 10^{-8 \pm 0.5} \text{ GeV cm}^{-2} \text{ s}^{-1} \text{ sr}^{-1}$ has been calculated [36], in agreement with the Waxman-Bahcall upper limit (Eq. 1.6).

1.4.2 Decay Scenario

As previously mentioned, the shock acceleration mechanism is a self-limiting process: For any given set of values of the acceleration region size R and the magnetic field strength B , simple criterion of Larmor containment of a particle of charge Ze within the acceleration region implies that there is a maximum energy $E \sim ZeBR$ up to which the particle can

be accelerated before escaping from the acceleration region.

Because of this difficulty, there is the possibility that the extremely high energy events may represent a fundamentally different component of cosmic rays in the sense that these particles may not be produced by any acceleration mechanism at all. These particles may simply be the result of the decay of some supermassive X particles with mass $m_X \gg 10^{20}$ eV originating from extremely high energy processes in the early Universe. The sources of the massive X particles could be topological defects such as cosmic strings or magnetic monopoles that could be formed in the symmetry-breaking phase transitions associated with Grand Unified Theories at the end of inflation. Alternatively, the X particles could be certain supermassive metastable relic particles of lifetime comparable to or larger than the age of the Universe, which could be produced in the early Universe through, for instance, particle production processes associated with inflation. A comprehensive review of the top-down scenario can be found, e.g., in [37]. It has to be remarked that mounting observations pointing out protons as the dominant particles for the EHECRs do not necessarily rule out superheavy particles as the sources of the highest energy cosmic rays.

Extremely high energy neutrinos are also predicted in a wide variety of top-down scenarios invoked to produce EHECRs. There are several ways neutrinos can be produced in the fragmentation of ultra high energy jets. The X particles can decay into quarks, gluons and leptons [38], which ultimately materialize into, among other particles, nucleons, γ -rays and neutrinos with energies up to m_X . Consequently, besides the photo-production of pions and subsequent muon decay, neutrinos can be produced by heavy quark decays. Bottom and charm quarks decay semileptonically about 10% of the time. Furthermore, top quarks produced in the jets decay nearly 100% of the time to bW^\pm . The W -bosons then decay semileptonically approximately 10% of the time to each neutrino species. In this scenario, the neutrino flux greatly exceeds the proton flux at energies larger than 10^{20} eV.

In the Z -burst scenario [39], ultrahigh energy neutrinos could be the sources of the GZK air showers. In this scenario, cosmic neutrinos will annihilate on the non-relativistic relic antineutrinos (and viceversa) at the Z resonance. The Z -boson decays hadronically about 70% of the time, creating a so-called Z -burst which contains photons and nucleons with energy near or above the GZK cutoff energy of roughly 5×10^{19} eV. If the Z -burst points in the direction of the Earth and it occurs within the GZK distance of Earth (< 100 Mpc), the photons and the nucleons produced by the Z -boson decay may easily initiate a super-GZK air shower at Earth.

Diffuse high energy neutrino flux measurements and the search for super-PeV neutrinos

can be used to constrain the top-down scenario.

1.4.3 Cosmogenic Neutrinos

In addition to neutrinos generated by high energy cosmic accelerators, there are high energy neutrinos induced by the propagation of cosmic rays in the local Universe after their interaction with the CMB [40]. The subsequent pion decay will produce a flux of so-called GZK or cosmogenic neutrinos. Since neutrinos carry approximately 5% of the proton energy, this flux is similar to the Waxman-Bahcall bound above 5×10^{18} eV [41]. In general, about 1% of cosmogenic neutrinos from the UHECR flux is expected.

The detection of these neutrinos will test the hypothesis that the UHECRs are protons (or possibly somewhat heavier nuclei) of extragalactic origin. On the other hand, an absence of the GKZ cutoff would reflect into an absence of cosmogenic neutrinos.

Chapter 2

The ANTARES neutrino telescope

A high energy neutrino detector behaves like a telescope when the neutrino direction is reconstructed with an angular precision of 1 degree or better. This is the case for high energy charged current muon neutrino interactions. The accurate measurement of the (anti)muon neutrino direction permits the association with (known) sources. It also allows the neutrino telescopes to face some of the most fundamental questions in high energy physics beyond the Standard Model: the nature of Dark Matter through the indirect search for weakly interacting massive particles (WIMPs); the study of sub-dominant effects of neutrino oscillations and the violation of Lorentz invariance; the study of relic particles such as magnetic monopoles or nuclearites in cosmic radiation; the coincident emission of neutrinos and gravitational waves.

A neutrino telescope is basically a three-dimensional set of arrays of photomultipliers designed to collect the Cherenkov light (§ 2.1) emitted by neutrino interaction products. The information provided by the number of photons detected and their arrival times is used to infer the neutrino track direction and energy.

The ANTARES (Astronomy with a Neutrino Telescope and Abyss environmental Research) is currently the most sensitive high energy neutrino observatory studying the Southern Hemisphere including the particularly interesting region of the Galactic Center. The ANTARES field of view has a sky coverage of 3.5π sr. ANTARES is also a unique deep-sea marine observatory providing continuous high-bandwidth monitoring of a variety of sensors dedicated to acoustic, oceanographic and Earth science studies.

The ANTARES Collaboration currently comprises 29 particle physics, astrophysics and sea science institutes from seven countries (France, Germany, Italy, the Netherlands, Romania, Russia and Spain).

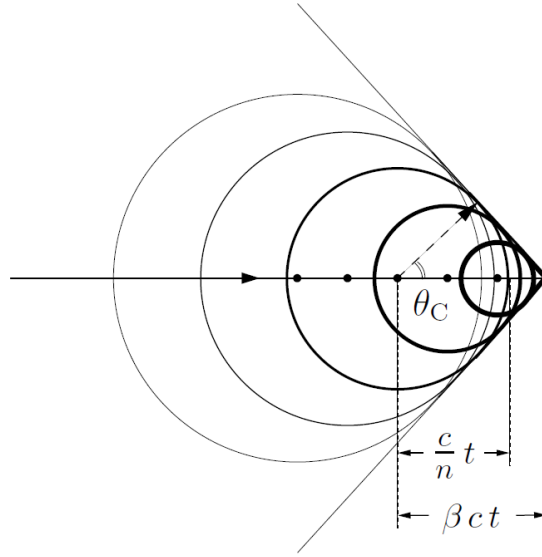


Figure 2.1: Schematic view of the production of Cherenkov radiation by a relativistic charged particle.

2.1 Cherenkov Radiation

Cherenkov radiation [42] is created when a charged particle passes through a medium with a speed larger than the speed of light in the medium. In this situation, the charged particle infers a polarization of the molecules along its trajectory. When the dipoles induced by the polarization restore themselves to equilibrium, a coherent radiation is emitted in a cone (Figure 2.1).

The angle of the Cherenkov cone depends on the refraction index n of the medium and the speed $v = \beta c$ of the particle, and can be geometrically calculated. During a time t , the particle will travel a distance $d_v = \beta ct$, while the light will travel a distance $d_c = (c/n)t$. The ratio between d_c and d_v determines the Cherenkov angle θ_C :

$$\cos \theta_C = \frac{1}{\beta n} \quad (2.1)$$

As high energy neutrinos are relativistic particles ($\beta \sim 1$) and the refraction index of sea water is $n \simeq 1.364$, the Cherenkov angle in sea water is $\theta_C \simeq 43^\circ$.

The number of Cherenkov photons N emitted by a particle with unit charge per unit distance x and unit wavelength λ is [43]

$$\frac{d^2 N}{dx d\lambda} = \frac{2\pi\alpha}{\lambda^2} \left(1 - \frac{1}{\beta^2 n^2} \right) \quad (2.2)$$

where α is the fine-structure constant. Hence a relativistic muon in water emits about 3.5×10^4 Cherenkov photons per meter in the 300 – 600 nm wavelength range.

	Mediterranean Sea water	
	$\lambda = 473 \text{ nm}$	$\lambda = 375 \text{ nm}$
absorption length	$60 \pm 10 \text{ m}$	$26 \pm 3 \text{ m}$
effective scattering length	$270 \pm 30 \text{ m}$	$120 \pm 10 \text{ m}$

Table 2.1: Light propagation parameters for Mediterranean Sea water.

The group velocity of Cherenkov light in a medium v_g depends not only on the photon wavelength and the refractive index of the medium, but also on the wavelength dependence of the refractive index:

$$v_g = \frac{c}{n} \left(1 + \frac{\lambda}{n} \frac{dn}{d\lambda} \right) \equiv \frac{c}{n_g} \quad (2.3)$$

where n_g is the group refractive index of the medium and c is the speed of light. In sea water in particular, for photons with a wavelength of 460 nm, the group refractive index is approximately 1.38.

Propagation of light through a medium is governed by absorption and scattering. The first effect reduces the intensity of the Cherenkov light emitted by the charged particle; the second effect influences the direction of the Cherenkov photons. Both phenomena depend on the photon frequency. Photon absorption is characterized by the absorption length λ_{abs} of the medium, defined as the average distance at which a fraction of e^{-1} of the photons is unabsorbed. Photon scattering in a medium is characterized by the scattering length λ_{scat} of the medium defined similarly as λ_{abs} , and by the mean scattering angle $\langle \theta_{scat} \rangle$. These quantities can be combined into an effective scattering length $\lambda_{scat}^{eff} = \lambda_{scat} / (1 - \langle \cos \theta_{scat} \rangle)$, where $\langle \cos \theta_{scat} \rangle$ is the mean cosine of the scattering angle. The light propagation parameters for Mediterranean Sea water for photons with different wavelengths are summarized in Table 2.1.

2.2 Detector Layout

The ANTARES detector [44] is located at a depth of 2.475 km in the Mediterranean Sea, south-east off the coast from Toulon, France (Figure 2.2). An electro-optical cable of about 40 km length serves as the power and data transmission line between the detector and the ANTARES control room in La Seyne-sur-Mer.

ANTARES is equipped with 885 photomultipliers (PMTs), arranged in triplets on 12 flexible vertical strings.

The basic element is the Optical Module (OM) [46], as shown in Figure 2.3. Each OM consists of a pressure-resistant glass sphere with a diameter of 43 cm and 15 mm thickness,

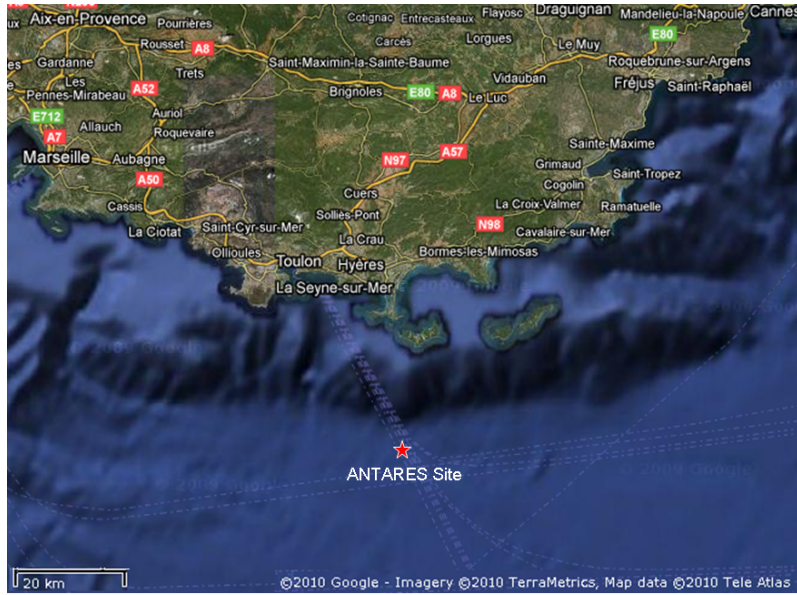


Figure 2.2: The ANTARES detector is located at a depth of 2475 m in the Mediterranean Sea, about 40 km offshore from Toulon, France ($42^{\circ}48'N$, $6^{\circ}10'E$). Satellite picture taken from Google Maps [45].

that contains a Hamamatsu R7081-20 PMT. The Hamamatsu R7081-20 is a hemispherical PMT with a diameter of 25 cm and an effective sensitive area of about 440 cm^2 . It contains 14 amplification stages and has a nominal gain of 5×10^7 at a high voltage of 1760 V. The PMT is sensitive to single photons in the 300 – 600 nm wavelength range; the peak quantum efficiency is about 25% between 350 and 450 nm. The charge resolution and the Transit Time Spread (TTS) of the PMT with respect to a single photon are approximately 40% and about 1.3 ns respectively. The dark count rate at the 0.25 photoelectron level is about 2 kHz. The PMT is surrounded by a μ -metal cage to minimize the influence of the magnetic field of the Earth on its response. The high voltage is provided by the electronics board mounted on the PMT socket, which also contains a LED calibration system. A transparent silicon rubber gel provides the optical and mechanical contact between the PMT and the glass. The glass hemisphere behind the PMT is painted black and contains a penetrator which provides the power and data transmission connection to the outside.

The OMs are grouped in triplets to form a storey or floor, as shown in Figure 2.4. They are mounted at equidistant angles around a titanium Optical Module Frame (OMF), and point downwards at 45° with respect to the vertical. The OMs are connected to the Local Control Module (LCM). The titanium cylinder at the center of the OMF houses the data transmission electronics of the OMs, as well as various instruments for calibration and monitoring. A storey may also contain extra instruments that are mounted on the OMF,

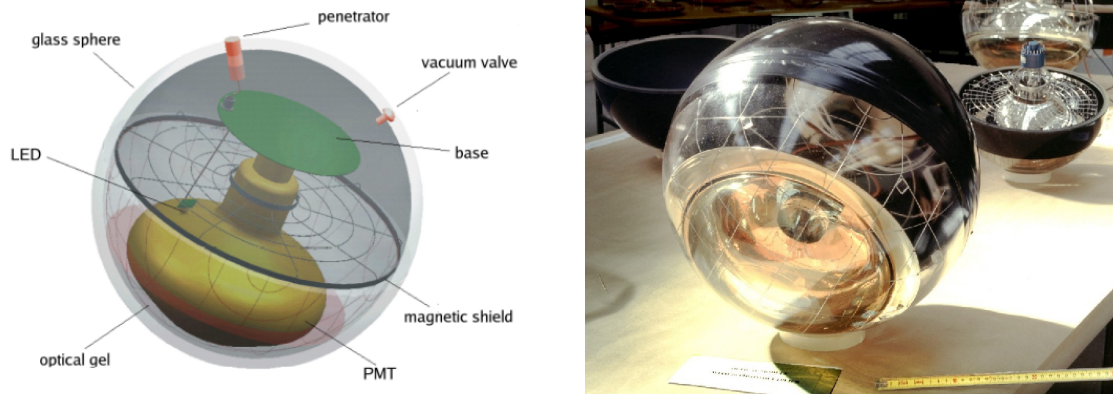


Figure 2.3: Schematic view (left) and picture (right) of an ANTARES optical module.

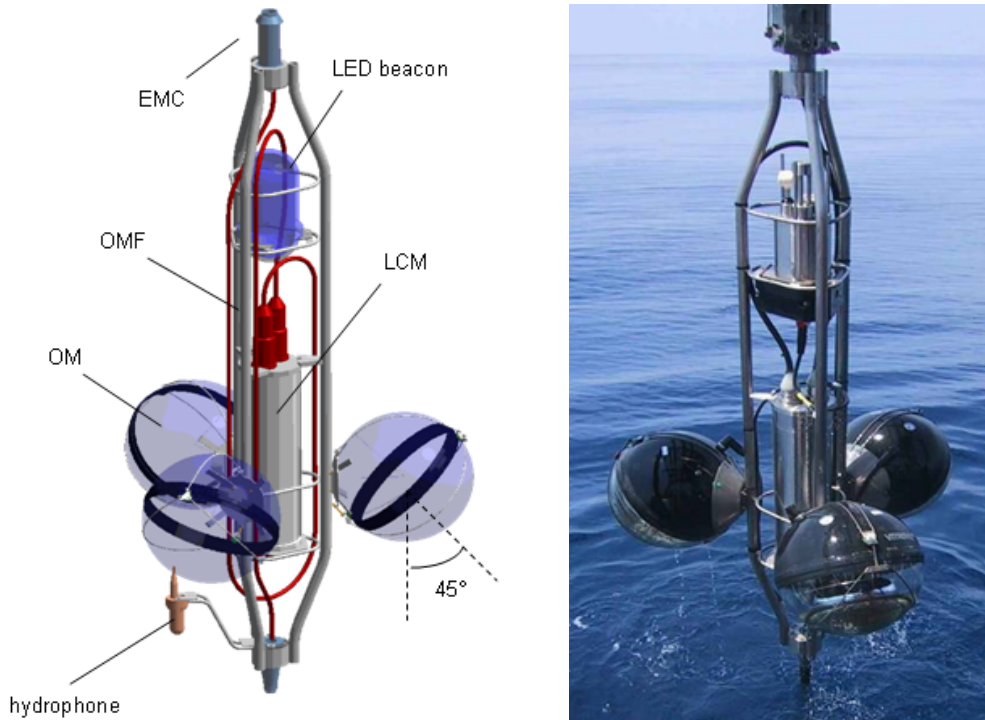


Figure 2.4: Schematic view (left) and picture (right) of an ANTARES storey.

such as a LED beacon or an acoustic hydrophone.

Storeys are serially connected with Electro-Mechanical Cables (EMCs), which contain electrical wires for power distribution and optical fibres for data transmission. The distance between adjacent storeys is 14.5 m. Five storeys linked together constitute a sector, an individual unit in terms of power supply and data transmission. In each sector, one of the five LCMs is a Master LCM (MLCM). The data distribution between all LCMs in the

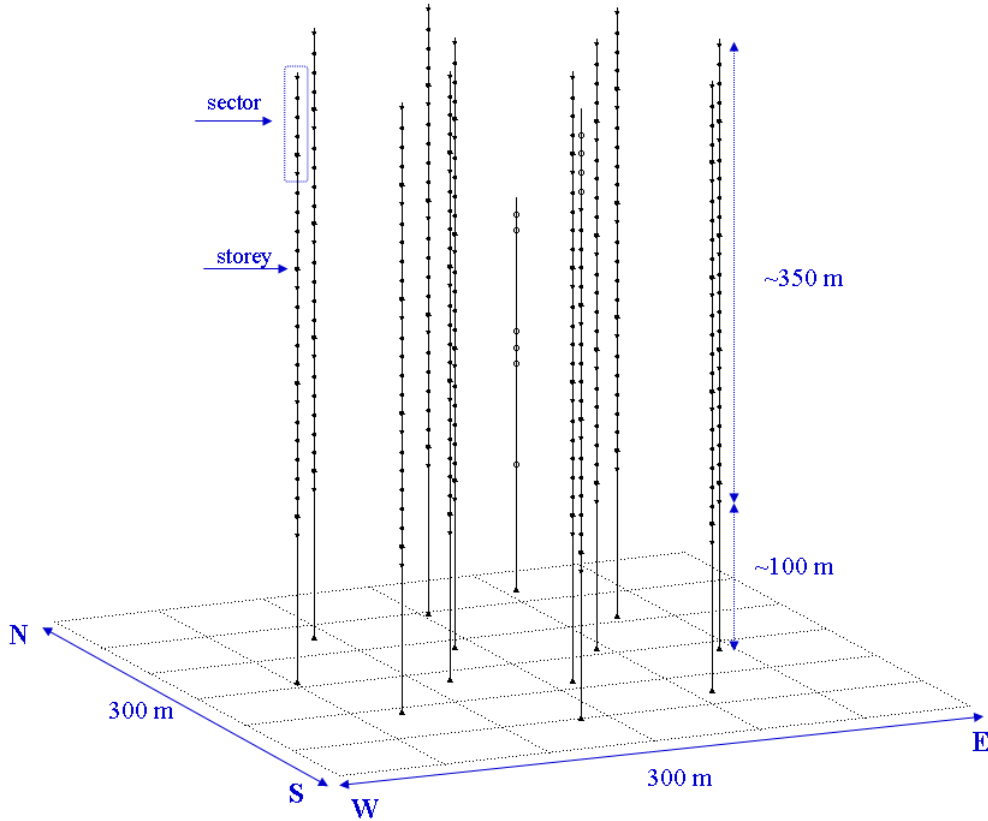


Figure 2.5: Schematic view of the ANTARES layout.

sector and the String Control Module is handled by the MLCM.

Five sectors linked together form an individual detector line. Each line is anchored to the seabed by a Bottom String Socket (BSS) and kept vertical by a buoy at the top of the line and by the buoyancy of the individual OMs. A string is 480 m long, since roughly 100 m from the seabed are left empty to allow for the development of the Cherenkov cone for upward going particles. The BSS contains a String Control Module (SCM), a String Power Module (SPM), calibration instruments and an acoustic release system. The acoustic release allows for the recovery of the complete detector line including BSS except for a dead-weight. The SPM houses the individual power supplies for all five sectors in the line. The SCM contains data transmission electronics to distribute data between each sector and the onshore control room.

The complete detector consists of 12 detector lines in a octagonal configuration, plus a dedicated instrumentation line (IL), as shown in Figures 2.5 and 2.6. The IL and the top sector of Line 12 do not contain OMs. Instead, they are equipped with various instruments for acoustic neutrino detection and for monitoring of environmental parameters. The av-

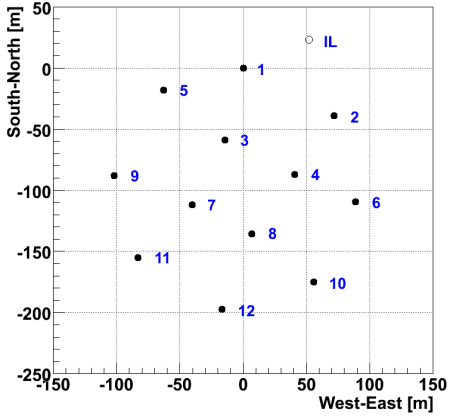


Figure 2.6: Schematic view of the ANTARES detector, as seen from above.

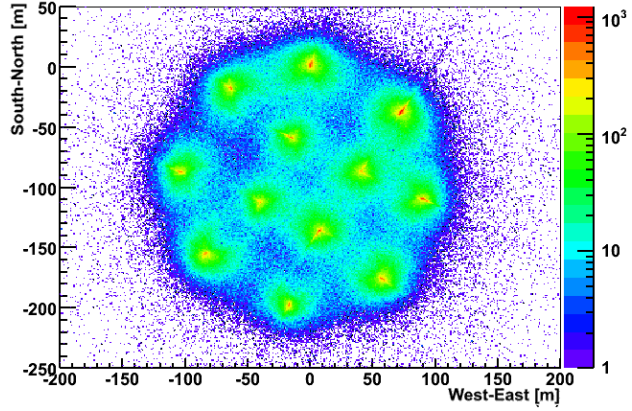


Figure 2.7: Fingerprints of ANTARES.

erage horizontal distance between lines is approximately 60 m. The BSS of each line is connected to the Junction Box (JB), which is the distribution point of power and data between the detector lines and the ~ 40 km long Main Electro-Optical Cable (MEOC) to the onshore control room in La Seyne-sur-Mer.

Figure 2.7 shows x and y coordinates of track fits at the time of the first triggered hit (§ 2.4.3). The track fits are dominated by downward going atmospheric muons or muon bundles. The structure of the detector becomes visible because the efficiency of the trigger algorithm is higher for tracks that pass closer to a detector line. For comparison, the x and y coordinates of the ANTARES lines are shown in Figure 2.6.

2.3 Detector Status

The ANTARES detector has been fully operational since May 28th 2008. Prior to its completion, ANTARES has taken data in intermediate configurations. An overview is given in Table 2.2. Data taking started in 2006 with the connection of Line 1 on March 2nd and Line 2 on September 21st. On January 29th 2007, after the connection of Lines 3 – 5, ANTARES surpassed the Baikal telescope as the largest neutrino telescope on the Northern Hemisphere. The detector doubled in size on December 7th 2007 with the connection of Lines 6 – 10 and the IL. Finally, ANTARES was completed on May 28th 2008 with the connection of Lines 11 and 12. Detector lines which showed significant problems during operation have been recovered, repaired, redeployed and reconnected as shown in the table. The detector was not operational between June 25th and September 5th 2008 due to a fault in the Main Electro-Optical Cable (MEOC).

Detector line	Connection date	Not operational
Line 1	March 2 nd 2006	
Line 2	September 21 st 2006	
Line 3	January 29 th 2007	
Line 4	January 29 th 2007	March 3 rd 2008 – May 28 th 2008
Line 5	January 29 th 2007	
Line 6	December 7 th 2007	October 27 th 2009 – present
Line 7	December 7 th 2007	
Line 8	December 7 th 2007	
Line 9	December 7 th 2007	July 2 nd 2009 – present
Line 10	December 7 th 2007	January 7 th 2009 – November 6 th 2009
Line 11	May 28 th 2008	
Line 12	May 28 th 2008	March 12 th 2009 – November 14 th 2009
IL	December 7 th 2007	

Table 2.2: Operational timeline of the ANTARES detector. The entire detector was not operational between June 25th and September 5th 2008 due to a fault in the MEOC.

2.4 Detector Acquisition

The transport of data and control signals between the PMTs and the onshore control room and vice versa is handled by the Data Acquisition (DAQ) system [47]. The DAQ system involves several steps, such as the signal digitization, the data transmission and the data filtering and storage.

2.4.1 Signal Digitization

A photon that hits the photo-cathode of a PMT can induce an electrical signal on the anode of the PMT. The probability for this to happen is characterized by the quantum efficiency of the PMT. If the amplitude of the signal exceeds a certain voltage threshold, the signal is read out and digitized by a custom designed front-end chip, the Analogue Ring Sampler (ARS), located in the LCM. The voltage threshold is set to a fraction of the single photoelectron average amplitude to suppress the PMT dark current, typically 0.3 photoelectrons. The time the signal crosses the threshold is timestamped by the ARS with respect to a reference time, provided by a local clock. All clocks in the detector are synchronized with a 20 MHz onshore master clock. A Time-to-Voltage Converter (TVC) is used to measure the time of the signal within the 50 ns interval between two subsequent clock pulses. The TVC provides a voltage which is digitized with an 8-bit Analogue-to-Digital Converter (ADC) to achieve a timestamp accuracy of about 0.2 ns. Each ARS contains two TVCs which operate in flip-flop mode to eliminate electronic dead-time. Ad-

ditionally, the charge of the analogue signal is integrated and digitized by the ARS over a certain time period by using an Analogue-to-Voltage Converter (AVC). The integration gate is typically set to 35 ns to integrate most of the PMT signal and to limit the contribution from electronic noise. The combined time and charge information of a digitized PMT signal is called a *hit*, and amount to 6 bits. Each PMT is read out by two alternately operating ARS chips to minimize electronic dead-time. All 6 ARS chips in an LCM are read out by a Field Programmable Gate Array (FPGA). The FPGA arranges the hits produced in a certain time window into so-called dataframes, and buffers these dataframes in a 64 MB Synchronous Dynamic Random Access Memory (SDRAM). The length of the time window is set to a value much larger than the time it takes for a muon to traverse the complete detector, typically 13.1072 ms ($2^{19} \times 25$ ns) or 104.8576 ms ($2^{22} \times 25$ ns).

2.4.2 Data Transmission

Each LCM contains a Central Processing Unit (CPU) which is connected to the onshore computer system. Each CPU runs two programs that manage the data transfer to shore. The DaqHarness program handles the transfer of dataframes from the SDRAM to the onshore control room. The ScHarness program handles the transfer of calibration and monitoring data, referred to as slow control data. Communication between all offshore CPUs and the onshore control room is done via optical fibers using the Transmission Control Protocol and Internet Protocol (TCP/IP). Each LCM CPU in a sector is connected via a bi-directional Fast Ethernet link (100 Mb/s) and an electro-optical converter to the MLCM. In the MLCM, these links are electro-optically converted and passed to an electronic data router (switch). The switch merges the 5 bi-directional Fast Ethernet links (4 LCM and 1 MLCM CPU) into two uni-directional Gigabit Ethernet links (1 Gb/s), one for incoming control signals and one for outgoing data. The gigabit signals are electro-optically converted using an optical wavelength which is unique for each MLCM in a detector line. The incoming and outgoing optical links of the 5 MLCMs in a detector line are routed to the String Control Module, where they are (de)multiplexed into a single optical fiber using Dense Wavelength-Division Multiplexing (DWDM). The optical fiber from each String Control Module runs through the Junction Box and the Main Electro-Optical Cable to the onshore control room, where they are (de)multiplexed into separate MLCM channels using the same wavelengths as in a detector line. The uni-directional optical MLCM channels from all demultiplexers are linked to an onshore switch via electro-optical converters. Finally, the switch is connected to a computer farm which accommodates the detector control and the data processing systems.

2.4.3 Data filtering and storage

The DAQ system is designed according to the so-called All-Data-To-Shore concept. This concept entails that no offshore signal selection is done except for the ARS threshold criterion, and all detected hits are transferred to shore. However, since the vast majority of detected signals is due to the optical background in the detector (§ 2.6), the data are filtered in the onshore computing farm to reduce the data storage demands. This is done by sending all dataframes that belong to the same time window to a common processor in the onshore computer farm. The complete set of dataframes from all ARS chips in the detector that correspond to the same time window is referred to as a timeslice, which consequently contains all hits that were detected in the same time window. Each timeslice is handled by a different processor, each of which accommodates a `dfilter` program. The `dfilter` program collects all dataframes corresponding to the same timeslice, and applies a trigger algorithm to search for signals that can be attributed to a charged particle which traversed the detector. Hence data filtering is done using software rather than hardware, which has advantages in terms of flexibility and detection sensitivity. Different trigger algorithms can be applied in parallel to search for specific signatures. The output from every datafilter is passed to the `dwriter` program that formats the data using the ROOT software package [48] and stores them in a database for offline analysis. Similarly, the slow control data are collected and processed by the `scDataPolling` program, and written to the database by the `dbwriter` program.

2.5 Detector Calibration

The precision with which the direction and energy of charged particles which traverse the detector can be determined, depends on the accuracy with which the photon arrival times at the PMTs and the location of those PMTs are measured. ANTARES is designed to achieve an angular resolution smaller than 0.3° for muons above 10 TeV [49]. To realize this resolution, the ANTARES detector comprises several independent calibration systems that are able to measure and monitor the absolute and relative timing of PMT signals and the location of all PMTs.

2.5.1 Time Calibration

The relative timing of the photon arrival times on the PMTs are needed to reconstruct the neutrino direction. Hence the offset of each local clock, caused by the optical path length to shore, has to be known. The offsets are obtained by an internal clock calibration system.

A calibration signal sent by the onshore master clock is echoed back along the same optical path by each LCM, to measure the relative offset of each LCM with an accuracy of 0.1 ns. A second calibration system based on a blue (470 nm) LED inside each OM is used to calibrate the time offset between the PMT photo-cathode up to the read-out electronics. The internal LED system is used in dedicated data-taking runs to monitor the relative variation of the PMT transit time. Finally, a calibration system based on optical beacons in the detector is used to calibrate the relative time offsets between PMTs. The system comprises four blue (472 nm) LED beacons located on storeys 2, 9, 15 and 21 of each detector line, and two green (592 nm) LASER beacons on the BSS of Lines 7 and 8. A small PMT in each LED beacon and a photo-diode in each LASER beacon measure the time of emission. Dedicated data-taking runs in which one or several beacons are flashed are performed regularly (typically once per week), to monitor the relative time offsets between the PMTs and the influence of water on the light propagation.

Measurements obtained by the internal LED and optical beacon systems have shown that the contribution of the detector electronics to the photon arrival time resolution is less than 0.5 ns [49]. Therefore the time resolution is dominated by the TTS of the PMTs ($\sigma_{\text{TTS}} \simeq 1.3$ ns), and the light scattering and chromatic dispersion by the sea water ($\sigma_{\text{sea}} \simeq 1.5$ ns, for an optical path length of 40 m).

The presence of ^{40}K (§ 2.6) in the sea water provides a convenient calibration source, which is used to verify the time offsets between the triplet of PMTs within a storey, as well as the long term stability of the PMT efficiencies. A mean coincidence rate of 16 ± 2 Hz has been observed. This agrees with the expected rate of 19 ± 3 Hz, obtained by Monte Carlo simulations [50].

Absolute timing is needed to correlate the reconstructed neutrino direction with specific sources in the Universe. This is achieved by synchronizing the onshore master clock to the Global Positioning System (GPS) time with an accuracy of 100 ns [47].

2.5.2 Charge Calibration

The charge calibration and threshold tuning of the PMTs and their associated front-end electronics enables to translate signal amplitudes into units of number of photoelectrons (p.e.), which are used in the track and energy reconstruction.

All the ARSs (§ 2.4.1) have been calibrated prior to deployment, measuring the transfer functions of the Analogue-to-Voltage Converter (AVC). This AVC transfer function is an important parameter for the correction of the so-called walk of the PMT signal, and for the measurement of the amplitude of each PMT pulse. The principal component used in

the on-shore calibration procedure is a pulse generator which directly sends signals to a pair of ARSs operating in a flip-flop mode. The generated pulse has a triangular shape with 4 ns rise time and 14 ns fall time, somewhat similar to the electrical pulse of a PMT with variable amplitude. The transfer functions of the dynamic range of the AVCs are linear and can therefore be parameterized by their slope and intercept. The distributions of these two parameters for a large sample of ARS chips have demonstrated that they are homogenous [51]. This implies that the same parameters can be used for all ARSs.

After the deployment, special data-taking runs reading the PMT current at random times enable the measurement of the so-called pedestal value of the AVC channel. The single photoelectron peak can be studied using randomly triggered events, since the optical activity due the ^{40}K decays and bioluminescent bacteria (§ 2.6) produces, on average, single photons at the photo-cathode level. The knowledge of the photoelectron peak and the pedestal is used to estimate the charge over the full dynamical range of the AVC. The AVC channel values of the pedestal and the single photoelectron peak are used to convert the analogue charge measurements of the PMT signals into photoelectron units.

Furthermore, since the ^{40}K coincidence rate is constant, it can be used to monitor the time evolution of the detector response. The ^{40}K coincidence rate has shown a regular decrease indicating a gain decrease of the PMTs. The PMT gain drop is thought to be due to ageing of the photo-cathode. Indeed, after the period between July and September 2008 when the detector was off for cable repair, the gains seem to have partially recovered when the PMTs were switched off [51].

2.5.3 Position Calibration

Each detector line is anchored to a BSS on the seabed and kept vertical by the buoyancy of the individual OMs and a top buoy. Nevertheless, due to the sea current and the flexibility of the Electro-Mechanical Cables, the radial displacement of a detector line can be considerable and real time positioning of each line is needed. This is achieved through two independent systems: an acoustic positioning system and a tiltmeter-compass system.

The acoustic positioning system consists of a three-dimensional array of acoustic emitters and receivers (hydrophones). The emitters, capable of sending high frequency (40 – 60 kHz) acoustic signals, are located on the BSS of each line. An additional independent autonomous emitter is located approximately 145 m from the detector array. Five hydrophones are located on Storeys 1, 8, 14, 20 and 25 of each detector line. Dedicated acoustic runs are performed every 2 minutes, during which the transit times between each emitter and the receivers are recorded. The distances between emitters and receivers are

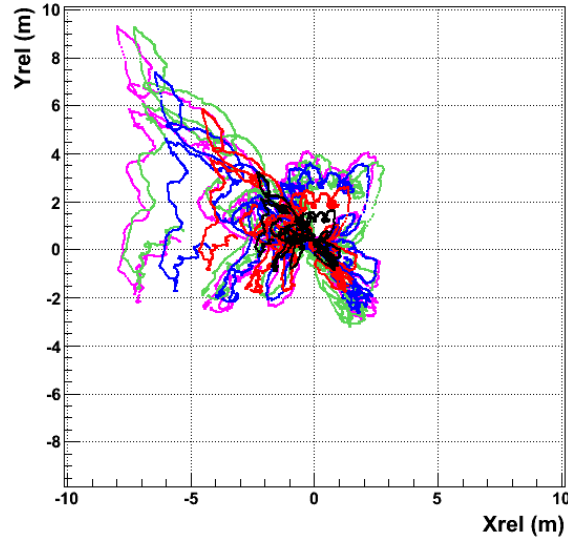


Figure 2.8: The horizontal movements of all hydrophones on Line 10 relative to the bottom of the line during February 2010; black points represent the hydrophone on Storey 1, red on Storey 8, blue on Storey 14, green on Storey 20 and magenta on Storey 25.

calculated using the sound velocity which is monitored by several sound velocity profilers located throughout the detector. The calculated distances are then used to triangulate the position of each acoustic receiver relative to the acoustic emitters with an accuracy of 10 cm [52].

The tiltmeter-compass system comprises a tiltmeter and a compass in each LCM. The two perpendicular tilt angles of a storey, the pitch and roll angles along the North-South and East-West axes, are monitored by a tiltmeter with an accuracy of 0.2° . The heading angle of a storey with respect to the North-South axis is monitored with a compass with an accuracy of 1° . The tiltmeter-compass data are also read out every 2 minutes.

The shape of each detector line is reconstructed by performing a global chisquare-like fit using information from both of these systems. The line shape is used to calculate the relative position of each PMT in the detector line with respect to the BSS. The absolute position of the BSS of each line is determined during the connection of a line to the Junction Box with a Remotely Operated Vehicle (ROV). This is done by acoustic positioning and water pressure measurements by the ROV, and the GPS location of the ship.

Figure 2.8 shows the movement of various storeys on a line, relative to its center axis. The extent of the displacement depends on the intensity of the sea current. For typical currents of few centimeters per second, the displacement is a few meters for the topmost storeys.

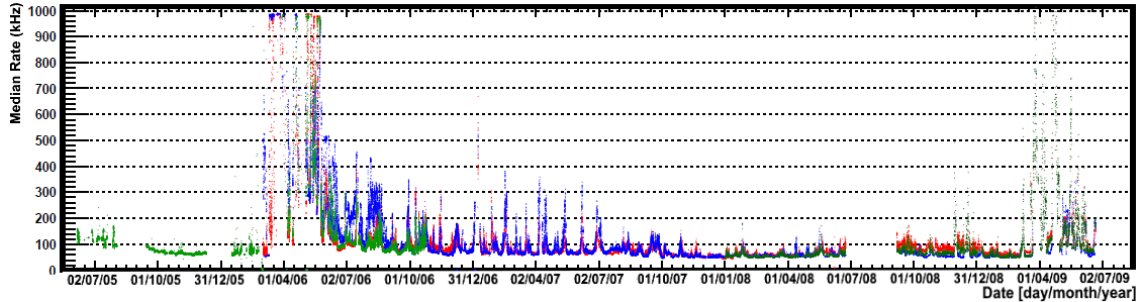


Figure 2.9: Median rate (in kHz) of measured single photon counts for Line 1 and IL, since July 2005 until June 2009. The green, red and blue lines indicate the median counting rates in storey 1 of the IL, the bottom of Line 1 (Storey 1, OM 1) and the top of Line 1 (Storey 25, OM 1) respectively.

2.6 Optical Background

Sea water contains two naturally occurring and independent sources of visible light, which have to be taken into account in neutrino telescoping: the radioactive potassium isotope ^{40}K and bioluminescence.

Monitoring of the sea water salinity at the ANTARES shows that it is constant at about 3.9%. This implies that sea water consists for about 400 ppm of potassium. About 0.012% of potassium consists of the long-lived radioactive isotope ^{40}K , which has a half-life of 1.3 billion years. It can decay to ^{40}Ca through beta decay (89% of the time) and to ^{40}Ar through electron capture and emission of an energetic photon (11% of the time). In the beta decay ($^{40}\text{K} \rightarrow e^- + \bar{\nu}_e + ^{40}\text{Ca}$), the maximum electron energy of 1.3 MeV lies above the Cherenkov threshold in water. In the electron capture ($^{40}\text{K} + e^- \rightarrow ^{40}\text{Ar}^*$, followed by $^{40}\text{Ar}^* \rightarrow ^{40}\text{Ar} + \gamma$), the photon energy of 1.46 MeV is sufficiently high to Compton scatter an electron above the Cherenkov threshold. A dedicated Monte Carlo simulation indicates that the counting rate for each PMT in the ANTARES detector due to ^{40}K events is constant at 34 ± 7 kHz [53].

The median counting rate per PMT for a number of arbitrary PMTs in ANTARES, as measured between 2005 and 2009, is shown in Figure 2.9. The corresponding mean counting rate per PMT, the so-called *baseline rate* (which on average varies between 60 and 100 kHz), is higher than what is expected from ^{40}K alone, and is highly time dependent. It is assumed that the surplus and time variations are due to bioluminescence, light produced by organisms living in the water. The amount of bioluminescent light detected in ANTARES is expected to be correlated to the amount of luminescent organisms in the water, and hence to the sea current velocity. Furthermore, occasionally the baseline

rate increases up to several MHz for short periods of time. These so-called bursts can last for seconds and are thought to be produced by organisms hitting the PMTs. The fraction of time during which the instantaneous background rate exceeds the baseline rate by at least 20% is referred to as the *burst fraction*.

Chapter 3

Parameterization of Atmospheric Muons

The most abundant signal seen by a neutrino telescope is due to high energy downward going muons produced in the extensive air showers resulting from interactions between primary cosmic rays and atmospheric nuclei. Although the shielding effect of the sea reduces their flux, at the ANTARES site the atmospheric muon flux is about six orders of magnitude larger than the atmospheric neutrino flux (Figure 3.1). These atmospheric muons represent a dangerous background for track reconstruction as their Cherenkov light can mimic fake upward going tracks. On the other hand, they are a useful tool to test offline analysis software, to check the understanding of the detector and to estimate systematic uncertainties.

This chapter starts with a brief description of the interaction of cosmic rays with the atmospheric nuclei and the subsequent creation and propagation of secondary particles through the atmosphere (§ 3.1). The primary cosmic ray models used as first inputs in the Monte Carlo simulations of underwater atmospheric muons are discussed in § 3.2. Particular interest is given to the HEMAS parameterization [54] from which parametric formulae [55] have been derived (§ 3.3) and compared to experimental data of some neutrino telescopes (§ 3.4). These formulae have been subsequently used to develop a fast event generator, called MUPAGE [56]. This code is one of the main topics of this thesis and it will be presented in the following chapter.

3.1 Cosmic Ray Interaction with the Earth's Atmosphere

Cosmic rays with an energy above about 10^{12} eV are capable of generating cascade showers containing thousands of secondary particles through interactions with the atmosphere.

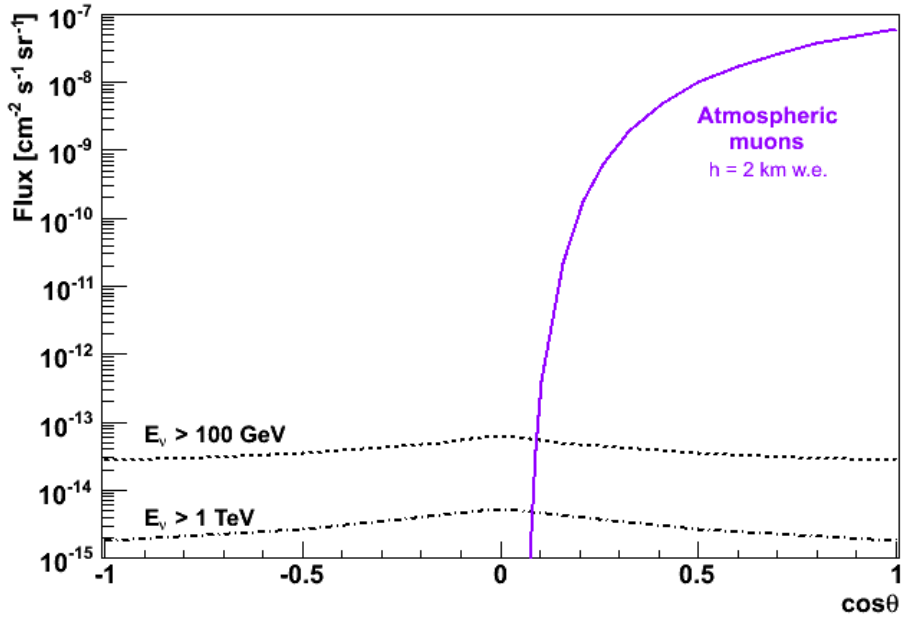


Figure 3.1: Different contributions to muon background as a function of the zenith angle. Atmospheric muons at a depth of 2 km w.e. are from MUPAGE [56] and atmospheric neutrino-induced muons are from calculations by Bartol [57]: The dotted line stands for $E_\nu > 100$ GeV and the dashed-dotted line for $E_\nu > 1$ TeV.

During the propagation of the air showers in the atmosphere, the number of particles initially increases until it reaches a maximum, after which it attenuates as more and more particles fall below the energy threshold for further particle production (about 1 GeV).

The initial interaction is

$$CR + N \rightarrow \pi^\pm, \pi^0, K^\pm, K^0, p, n, \dots, \text{exotic particles}$$

A cosmic-ray-induced air shower can be described by three components: electromagnetic, muonic and hadronic. The classic discussion by Greisen is reported in [58]. The shower consists of a core of high energy hadrons that continually feed the electromagnetic part of the shower, primarily by photons from decay of neutral pions and eta particles. Each high energy photon generates an electromagnetic subshower through pair production and bremsstrahlung interactions with the atmosphere. However, as the shower develops, the number of electrons and positrons declines rapidly after reaching a maximum because radiation and pair production processes subdivide the energy down to the critical energy after which electrons quickly lose the remaining energy by ionization. Nucleons and other high energy hadrons contribute further to the hadronic cascade. Lower energy charged pions and kaons decay to feed the muonic component.

Below 100 GeV, most pions and kaons produced in the atmosphere decay before they

interact. The pion decays (and their branching ratios) are the same decays which produce astrophysical neutrinos and γ -rays, namely

$$\pi^+ \rightarrow \mu^+ + \nu_\mu \quad (\sim 100\%) \quad (3.1a)$$

$$\pi^- \rightarrow \mu^- + \bar{\nu}_\mu \quad (\sim 100\%) \quad (3.1b)$$

$$\pi^0 \rightarrow \gamma\gamma \quad (\sim 98.8\%) \quad (3.1c)$$

Kaons decay with almost 63.5% probability to:

$$K^+ \rightarrow \mu^+ + \nu_\mu \quad (3.2a)$$

$$K^- \rightarrow \mu^- + \bar{\nu}_\mu \quad (3.2b)$$

These meson decays significantly contribute to the production of atmospheric muon neutrinos.

Another particular important semileptonic decay channel to take into account, with almost 40.6% of branching ratio, is

$$K_L^0 \rightarrow \pi^+ + e^- + \bar{\nu}_e \quad (3.3a)$$

$$K_L^0 \rightarrow \pi^- + e^+ + \nu_e \quad (3.3b)$$

which is the dominant source of atmospheric electron neutrinos for energies higher than 10 GeV when muon decay is unimportant. Muons indeed are nearly stable and rarely interact catastrophically, but only lose energy relatively slowly by ionization of the medium. Therefore, muons give the dominant signal deep in the atmosphere, underground and underwater.

Production of heavier flavors, especially charm, eventually becomes important for muon and neutrino fluxes at very high energy. Above 1–10 TeV, the semileptonic decays of very short-lived charmed particles like D mesons and Λ baryons are the dominant sources, despite their low production rate. The main contribution comes from the D meson decay modes, in the charged (almost 9% of probability)

$$D^+ \rightarrow \bar{K}^0 + l^+ + \nu_l \quad (3.4a)$$

$$D^- \rightarrow K^0 + l^- + \bar{\nu}_l \quad (3.4b)$$

and in the neutral (roughly 3-4% of probability) channels

$$D^0 \rightarrow K^- + l^+ + \nu_l \quad (3.5a)$$

$$\bar{D}^0 \rightarrow K^+ + l^- + \bar{\nu}_l \quad (3.5b)$$

and from the Λ_c baryon decay mode (roughly 2% probability):

$$\Lambda_c^+ \rightarrow \Lambda^0 + l^+ + \nu_l \quad (3.6)$$

where l can be only e or μ .

The role of D_s meson decay

$$D_s^+ \rightarrow l^+ + \nu_l \quad (3.7a)$$

$$D_s^- \rightarrow l^- + \bar{\nu}_l \quad (3.7b)$$

is almost negligible (of order to 10^{-3}) for the production of e and μ , but has a branching ratio of almost 7% for the production of τ and ν_τ [59].

Because of the short lifetime of these particles, heavy meson and baryon decays are not inhibited by interactions with the atmosphere for energies below about 10^8 GeV. Muons and neutrinos generated in heavy flavor decay are called *prompt leptons*. The energy at which the contribution of prompt muons to the sea level flux becomes equal to that of muons from π, K decays is expected to be between 10 TeV and 10^3 TeV, depending on the charm production model [60].

3.2 Primary Cosmic Ray Models

The two main ingredients that have to enter in the Monte Carlo simulations of atmospheric muons are the cosmic ray energy spectrum and composition, and the properties of the inelastic interactions of nucleons with air nuclei. Then, the particles must be propagated in the atmosphere and in the overburden medium of the detector.

Although the general features of the muon spectrum measured at ground level are well understood, differences between Monte Carlo computations and experimental data up to 25–30% exist [61]. These differences could reside either in an incorrect knowledge of the cosmic ray energy spectrum and composition or in the adopted interaction model.

Concerning the cosmic ray composition, different models have been introduced with the intent of reproducing the cosmic ray energy spectrum behavior for mass group elements. It is customary in the Monte Carlo computations to account for five mass groups of primaries, namely H, He, C+N+O, Mg+Si, Fe. This selection follows the fact that these nuclei are the ones synthesized by nuclear-fusion processes occurring in different stages of massive star evolution and are subsequently spread out in the Galaxy during supernova explosions.

The most common parameterizations of the primary cosmic rays are: NSU [62], polygonato [63], HEMAS [54] and FLUKA [64].

The HEMAS code was developed to simulate the muon flux underground and it was extensively used by the MACRO experiment at Gran Sasso (Italy) in the study of the muon flux and the muon bundle rate [65] at an average depth of 3400 m w.e. Hadronic interactions in the atmosphere are handled with the hadronic interaction code DPMJET [66]. In HEMAS, the energy spectrum assumed to generate each mass group is represented by a function of the form

$$\Phi(E) = K_i E^{-\gamma_i} \quad (3.8)$$

where K_i and γ_i have different values depending on the mass group and E is the energy per particle. Furthermore, for the same nucleus, they have different values before and after the knee energy E_k . The values of the constants are reported in Table 3.1.

Nucleus	Z	A	K_1 [m ² s sr GeV] ⁻¹	γ_1	K_1 [m ² s sr GeV] ⁻¹	γ_2	E_k [GeV]
H	1	1	3000	2.56	2.1×10^6	3	3×10^6
He	2	4	20100	2.74	6×10^6	3.12	2×10^6
CNO	7	14	600	2.5	3.7×10^7	3.24	3×10^6
Mg-Si	12	24	877	2.5	6.3×10^7	3.25	3×10^6
Fe	26	56	311	2.36	4.1×10^6	3	2.7×10^6

Table 3.1: The constants used in the HEMAS model.

Figure 3.2 shows the comparison of Monte Carlo input spectra, considering the convolution of the all particle groups (*all-particle*). The plot represents the differential spectra multiplied by $E^{2.7}$ as a function of energy per particle. The value 2.7 is very close to the weighted average of the spectral indices of the elements with Z from 1 to 28 deduced by the best fits to experimental data as presented in [67]: $\gamma_Z = -(2.684 \pm 0.008)$. The ‘theoretical’ spectra will thus appear almost horizontal with a trend to increase (decrease) according to their spectral indices having values smaller (larger) than the above chosen value. Moreover, by using a logarithmic scale along the y -axis it is straightforward to appreciate the percentage deviations of one model from the others, that can vary from 10% to 100% in absolute value.

The polygonato and the NSU models show the apparent major difference in the shape of the knee that is much sharper in the former one. The HEMAS parameterization tends to overestimate the individual spectra and in particular the Fe spectrum with respect to the other models, as a consequence of a flatter spectral index. However, the knee position in the all-particle spectrum seems to coincide with that of the polygonato and NSU model.

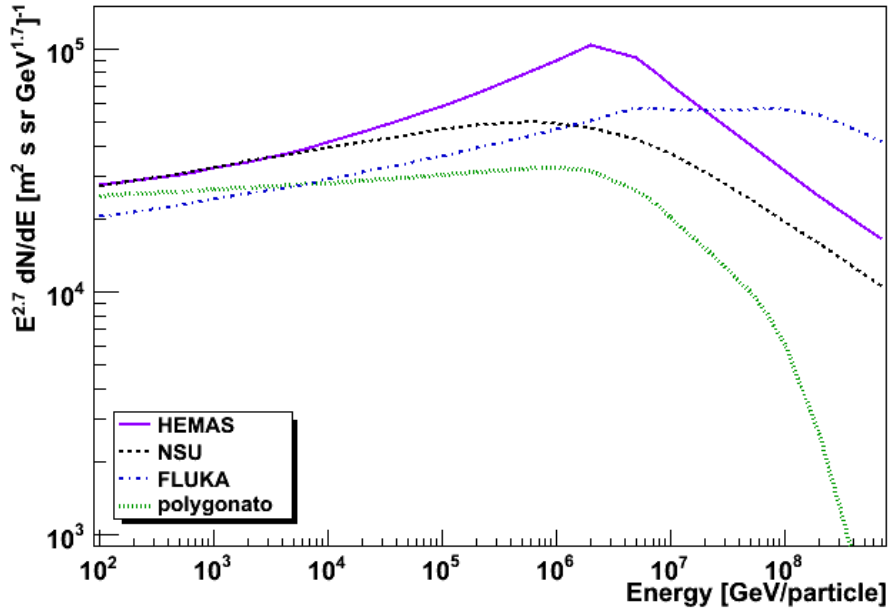


Figure 3.2: Parameterizations of the all-particle input spectra of Monte Carlo computations cited in the legend: HEMAS [54], NSU [62], FLUKA [64] and polygonato [63].

The FLUKA model overestimates the contribution of medium nuclei (CNO, Mg-Si and Fe) by assuming softer spectral indices for their spectra. The effect is that the knee of the all-particle spectrum is smoother and displaced at a higher energy than in the other models.

The all-particle spectrum as a function of energy resulting from measurements by some direct and indirect experiments is shown in Figure 3.3 compared to the Monte Carlo predictions. As already mentioned, the ‘theoretical’ spectra have been multiplied by $E^{2.7}$ and for comparison so are the experimental data. As a consequence, if the energy normalization of an experiment is overestimated (underestimated) by a factor κ , the flux intensity will be overestimated (underestimated) by a factor $\kappa^{1.7}$. This emphasizes the deviations between experimental data sets and ‘theoretical’ models.

Although the HEMAS parameterization seems to overestimate the overall flux with respect to the other parameterizations as well as the observations, it should be remarked that the observable variables are obtained after the unfolding with the interaction model. For this reason, HEMAS in combination with the DMPJET interaction model have been preferred over other models, since they were deeply used and cross-checked with the results of the underground MACRO experiment. Additionally, the input primary cosmic ray spectrum is based on a phenomenological model obtained by MACRO [65]. Moreover, HEMAS is optimized to reproduce the multiplicity distribution of muons in bundles and

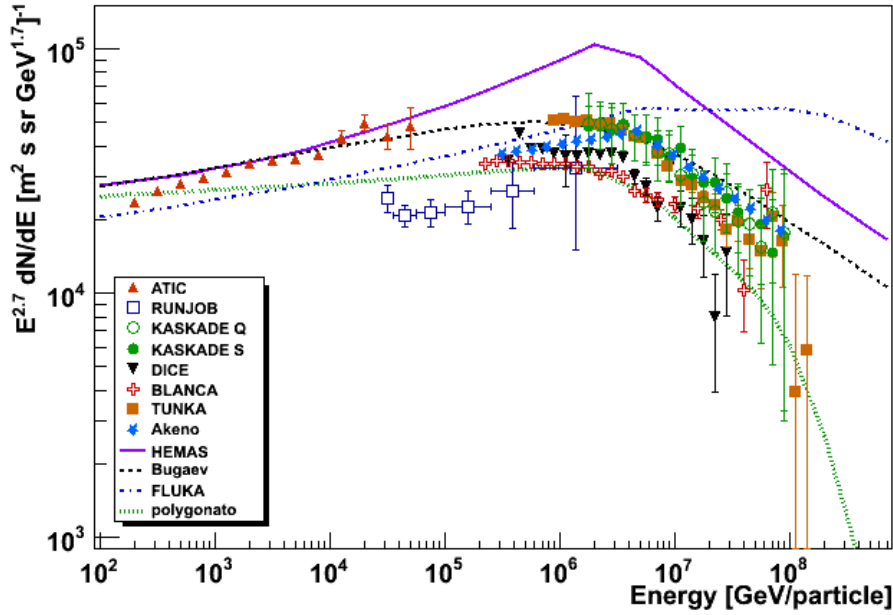


Figure 3.3: All-particle input spectra deduced by direct (ATIC [68] and RUNJOB [69]) and indirect (KASKADE [70], DICE [71], CASA-BLANCA [72], TUNKA [73] and Akeno [74]) measurements and the parameterizations used in the Monte Carlo simulations (HEMAS [54], NSU [62], FLUKA [64] and polygonato [63]).

the lateral distribution of muons inside the bundle at different depths of standard rock.

3.3 From the HEMAS Model to the Parametric Formulae of Underwater Muons

A parameterization of the multiple muon flux and energy spectra [55] has been deduced from the results of a full Monte Carlo simulation of the primary cosmic ray flux, interactions and shower propagation in the atmosphere. The latest version of the HEMAS code was used: HEMAS-DPM [75].

The reliability of the code is restricted to secondary particles with energies above 500 GeV. Muons that have a lower energy at sea level are discarded because their survival probability for depths larger than 1.5 km w.e. is very small, and completely negligible at 2 km w.e.

The so-called prompt muons (§ 3.1) and other short-lived particles produced in the interactions of cosmic rays with the atmosphere are not included in the Monte Carlo simulation. An unknown uncertainty factor due to these processes should be included for muon residual energies higher than roughly 10 TeV.

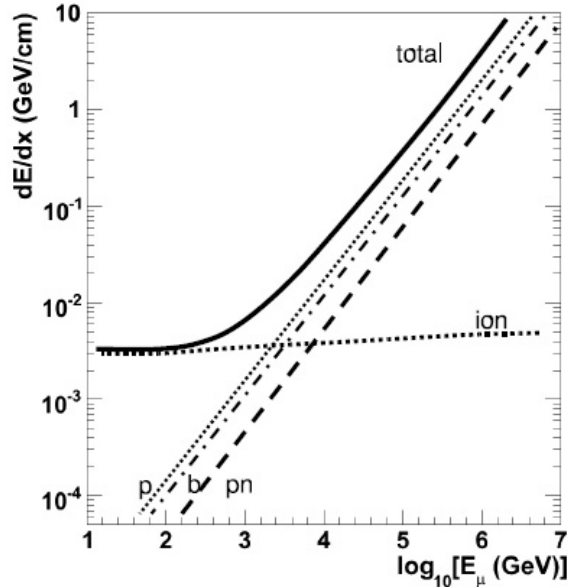


Figure 3.4: Muon energy loss in water from [76]: p = e^+e^- pair production; b = bremsstrahlung; pn = photo-nuclear interaction; ion = ionization.

3.3.1 Muon Energy Loss in Water

Muons that traverse through matter lose energy by ionization and by radiative processes: bremsstrahlung, direct production of e^+e^- pairs, and photo-nuclear interactions. In the ionization process, the muon interacts with the electric field generated by the electron cloud of the atom. In the radiative processes, the muon interacts with the nuclear electric field of the atom.

The total muon energy loss may be expressed as a function of the amount of matter traversed X as [2]

$$-\frac{dE_\mu}{dX} = a + bE_\mu \quad (3.9)$$

where a is the ionization loss and b is the fractional energy loss by the three radiative processes. Figure 3.4 shows the energy loss due to different interactions in water as a function of the muon energy. As can be seen, ionization is nearly independent of energy, whereas the radiative processes are proportional to the muon energy.

The quantity $\epsilon = a/b$ defines a critical energy below which continuous ionization loss is more important than radiative losses.

In the full Monte Carlo simulation, the muons in the atmospheric showers that reached the sea level were propagated down to 5 km of water using MUSIC [76], a three-dimensional muon propagation code which uses recent and accurate cross sections of the muon interactions with matter.

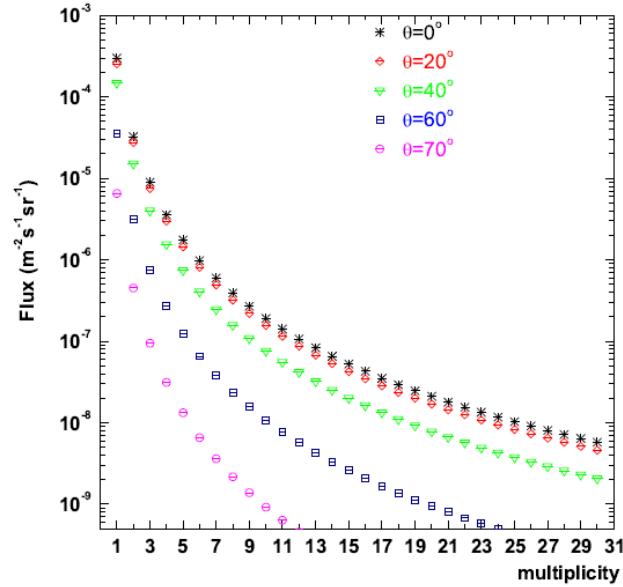


Figure 3.5: Flux of muon bundles as function of multiplicity m at depth $h = 2.5$ km w.e. for five different zenith angles, $\theta = 0^\circ, 20^\circ, 40^\circ, 60^\circ$ and 70° as computed with Eq. (3.10).

3.3.2 Flux of Muon Bundles

The flux of single and multiple muons (so-called muon bundles) with multiplicity m is obtained as a function of vertical depth h and zenith angle θ [77], using two free parameters (K and ν), as:

$$\Phi(m, h, \theta) = \frac{K(h, \theta)}{m^{\nu(h, \theta)}} \quad (3.10)$$

The validity range of the vertical depth h is between 1.5 and 5 km w.e., the validity range of the zenith angle θ is up to 85 degrees.

Figure 3.5 shows how the flux of muon bundles of increasing multiplicity m decreases with the zenith angle.

3.3.3 Energy Spectrum

Assuming a power-law for the primary beam energy, the expected muon energy distribution, at a slant depth $X = h/\cos\theta$, is described by [78]:

$$\frac{dN}{d(\log_{10} E_\mu)} = G \cdot E_\mu e^{bX(1-\gamma)} [E_\mu + \epsilon(1 - e^{-bX})]^{-\gamma} \quad (3.11)$$

where γ is the spectral index of the primary cosmic rays and ϵ is defined from the parameters of the muon energy loss formula (Eq. 3.9). γ and ϵ are used as free fit parameters and b is fixed. $G = G(\gamma, \epsilon)$ represents a normalization constant so that the integral over the muon energy spectrum (Eq. 3.11) from 1 GeV to 500 TeV is equal to one.

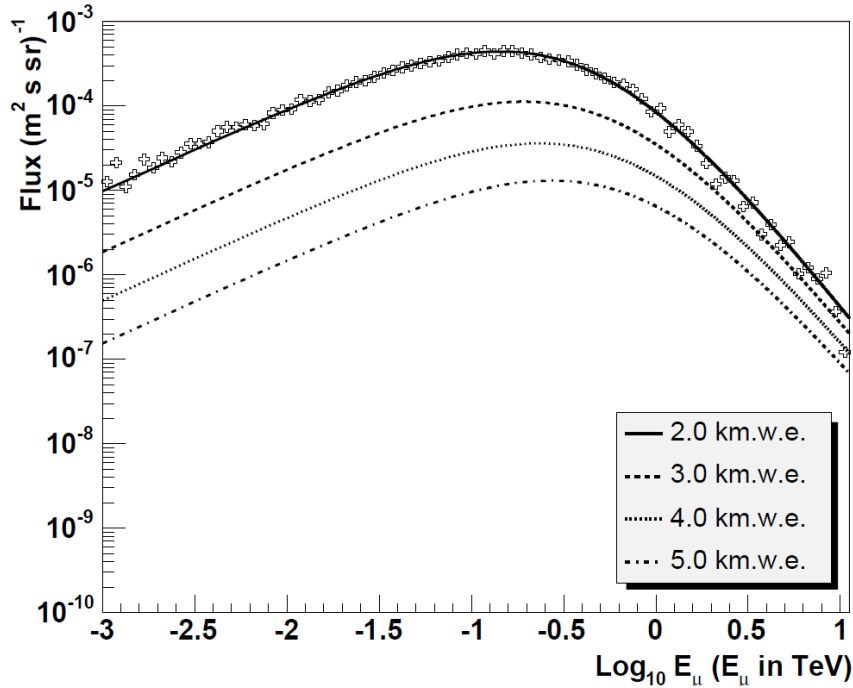


Figure 3.6: Differential energy spectra (normalized to unit area) of vertical ($\theta = 0^\circ$) single muons at different depths ($h = 2, 3, 4$ and 5 km w.e.). The marker points (superimposed to $h = 2$ km w.e.) correspond to the values obtained with the full Monte Carlo simulation. Figure taken from [55].

Figure 3.6 shows the energy distribution of vertical ($\theta = 0^\circ$) single muons at various depths. The energy spectrum is evaluated by multiplying the normalized energy distribution (Eq. 3.11) with the flux (Eq. 3.10) of vertical single muons: $\Phi_1 = \Phi(m = 1, h, \theta = 0^\circ)$. For instance, at $h = 3$ km w.e., $\Phi_1 = 1.6 \times 10^{-4} (\text{m}^2 \text{ s sr})^{-1}$. The total muon flux is $\Phi_T = \sum_m \Phi(m, h = 3 \text{ km w.e.}, \theta = 0^\circ) = 2.2 \times 10^{-4} (\text{m}^2 \text{ s sr})^{-1}$. Note that, as each integrated energy spectrum is normalized to 1, Eq. (3.11) gives only the shape of the distribution.

The situation is more complicated for multiple muons. Particles resulting from hadron-air interactions are produced in clusters. The number of charged hadrons follows a negative binomial distribution, whose characteristic depends on their primary energy. The transverse momentum p_t of the mesons follows in part an exponential-law distribution and in part a power-law distribution [75, 79]; most of the energy is concentrated in the very forward region (i.e. near the longitudinal axis). Muons produced in the decay of secondary mesons which reach a given water depth h follow the energy distribution of the parent mesons. As a consequence, in a muon bundle, the most energetic muons are expected to arrive closer to the shower axis. This effect is shown in Figure 3.7, obtained from the Monte

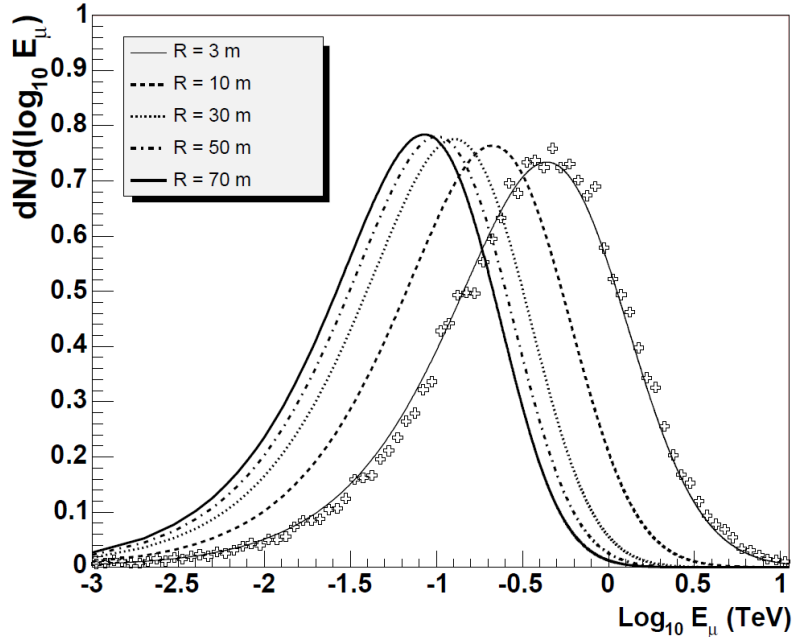


Figure 3.7: Differential energy spectra (normalized to unit area) of double muons ($m = 2$) assuming vertical direction ($\theta = 0^\circ$) and depth $h = 3.5$ km w.e., at five different distances from the bundle axis: $R = 3, 10, 30, 50$ and 70 m. The marker points (superimposed to $R = 3$ m) correspond to the values obtained with the full Monte Carlo simulation. Figure taken from [55].

Carlo parameterization in [55] assuming the vertical direction and a depth $h = 3.5$ km w.e.

Hence, the energy spectrum (Eq. 3.11) of muon bundles depend not only on the vertical depth h and on the zenith angle θ , but also on the muon bundle multiplicity m and on the muon radial distance R from the shower axis.

3.3.4 Lateral Spread

The muon lateral distribution in a plane perpendicular to the shower axis can be described as [54]

$$\frac{dN}{dR} = C \frac{R}{(R + R_0)^\alpha} \quad (3.12)$$

where R is the distance from the shower axis and C , R_0 and α are parameterization constants.

Figure 3.8 shows the normalized lateral distribution of vertical double muons at different depths h as obtained from Monte Carlo parameterization in [55].

The average distance of all muons in a bundle to the shower axis depends on the bundle multiplicity m , on the vertical depth h and on the zenith angle θ . At a given depth, the average distance to the shower axis of each muon in a bundle slightly decreases when the

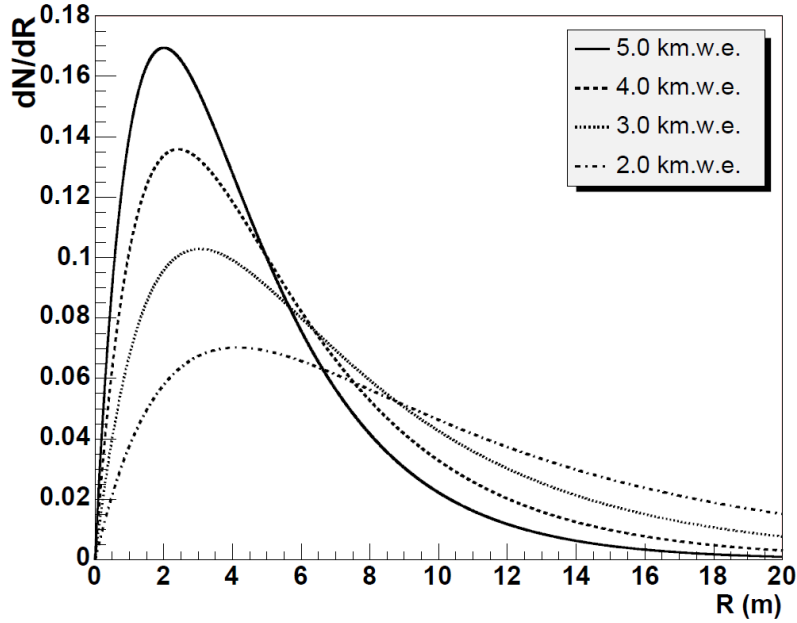


Figure 3.8: Lateral distribution (normalized to unit area) for vertical double muons ($m = 2$) at four different depths ($h = 2, 3, 4$ and 5 km w.e.). Figure taken from [55].

multiplicity m increases. This can be qualitatively understood because bundles with high multiplicities are generally produced by primary parents of high energies.

3.3.5 Multiplicity

The distribution of the muon multiplicities in a bundle depends on the vertical depth h and on the zenith angle θ . The dependence of the multiplicity distribution on these two variables is the following: for a fixed zenith angle θ , bundles with high multiplicity are suppressed when h increases; for a fixed vertical depth h , bundles with high multiplicity are suppressed when θ increases (Figure 3.9). In both cases the number of muons in the bundle decreases because increasing h or θ is equivalent to increasing the path length in the water through which muons travel.

3.4 Comparison of Parametric Formulae with Experimental Data

A comparison of the zenith distribution evaluated at a fixed depth using Eq. (3.10) with some experimental data has been performed [80]. Figure 3.10 shows a comparison between the predicted muon zenith angular distribution at three different depths and the measurements of the ANTARES [81] and Baikal [82] underwater neutrino telescopes and

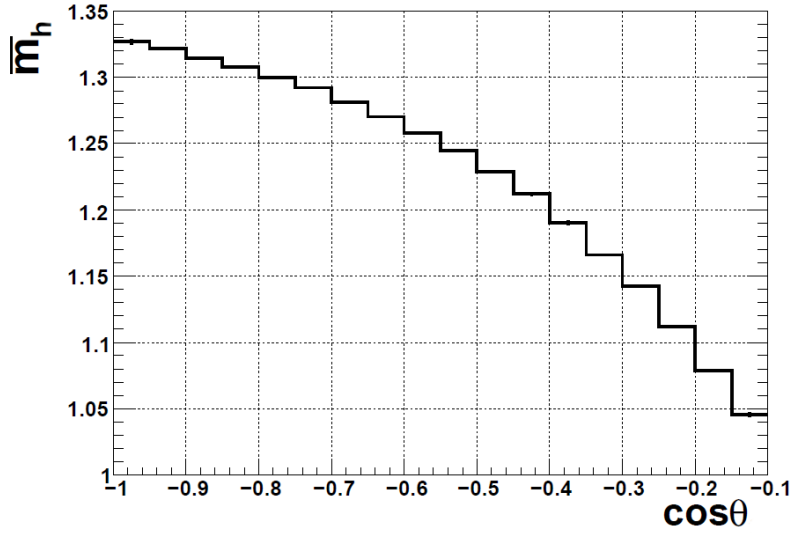


Figure 3.9: Average muon event multiplicity \bar{m}_h as function of the cosine of the zenith angle θ at the fixed sea depth $h = 2$ km for energies larger than 20 GeV. Figure taken from [81].

the AMANDA-II [83] under-ice experiment. The AMANDA data (triangular markers) superimposed to the line at a vertical depth $h = 1.68$ km w.e. have been converted to intensities relative to the underwater depths, taking into account the lower ice density $\rho_{ice} = 0.917$ g cm $^{-2}$.

The comparison demonstrates that the analytical solution provides a good represen-

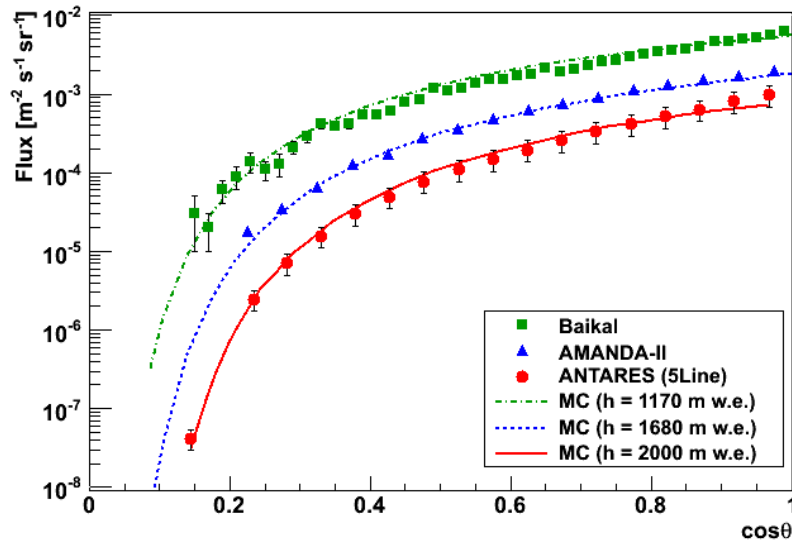


Figure 3.10: Muon flux as a function of the cosine of zenith angle θ as measured by ANTARES [81], AMANDA-II [83] and Baikal [82] at three different depths. The results obtained by the parametric formulae at the three depths are superimposed as full lines.

tation of the experimental data so far collected. This is true also in the case of the Baikal experiment, at a depth $h = 1.17$ km w.e., nominally outside the range of validity of the parameterization. Note that not all experiments have declared their systematic uncertainties.

Chapter 4

The Simulation of Underwater Atmospheric Muons: the MUPAGE Code

The development of an event generator of atmospheric muons for neutrino telescopes deduced from the parametric formulae introduced in Chapter 3 is one of the main topics of this thesis. This chapter describes MUPAGE (MUon GEnerator from PArametric formulae), a standalone C++ code, already published in [56]. It produces, in an ASCII table, the muon event kinematics on the surface of the so-called *can*, an imaginary cylinder surrounding the active volume of a generic underwater/ice neutrino telescope. The ASCII table can subsequently be used as input in the following steps of a detector-dependent Monte Carlo simulation, which includes production of light in water/ice and simulation of the signal in the detection devices. Some applications of MUPAGE can be found in [84].

§ 4.1 presents the structure of the MUPAGE code. § 4.2 describes the generation of events on the surface of the can, in which a *Hit-or-Miss* method [85] is applied. Events can be single muons (§ 4.3) or the more complex multiple muons (§ 4.4). There is neither bias nor ordering (in energy, multiplicity and zenith angle) in the simulation. All events have the same weight, thus the output file reproduces a real data file. For each run the livetime is computed as described in § 4.5. In § 4.6, using MUPAGE as event generator, the angular distributions of reconstructed atmospheric muon tracks have been computed and subsequently compared with the ANTARES data.

4.1 Program Structure

MUPAGE needs some input parameters, as described in [56], such as the detector configuration (Figure 4.1), the density of the detector medium and the ranges of the various

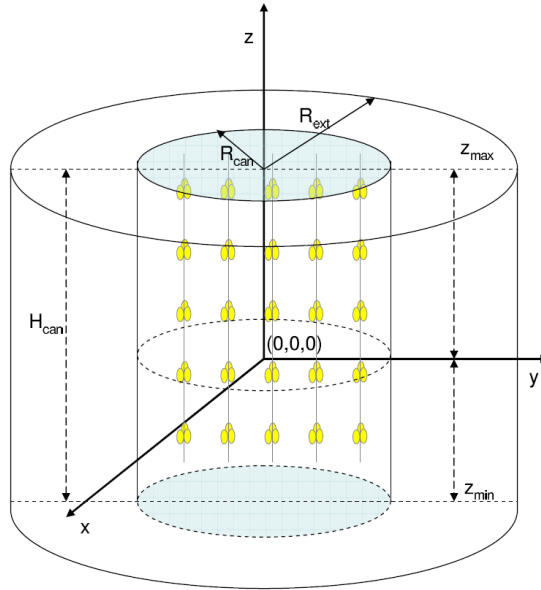


Figure 4.1: Sketch of the geometrical meaning of some input parameters. The cylinder surrounding the instrumented volume is the *can*, with radius R_{can} and height H_{can} . The events are generated on an extended can, with $R_{ext} = R_{can} + R_{ecr}$ [56]. The lower disk is at a depth H_{max} with respect to the sea/ice surface. The origin of the detector coordinate system lies on the cylinder axis, but it does not necessarily coincide with the center of the cylinder.

simulation parameters (e.g. multiplicity, zenith angle, muon energy).

As shown in Figure 4.1, the radius of the generation volume must be increased by a quantity R_{ecr} , in order to accept *peripheral* muons in large bundles. These peripheral muons are due to the high multiplicities of bundles (which at roughly 2 km w.e. depth can reach up to 10^3 muons per bundle) and to the fact that muons can be hundreds of meters far from the shower axis. The radius of the generation cylinder is thus $R_{ext} = R_{can} + R_{ecr}$. In the following, the can refers to the extended can.

A MUPAGE event is a bundle of muons with multiplicity m_c on the can. As schematically described by the flowchart in Figure 4.2, the bundle multiplicity, direction and impact point of the shower axis on the can surface are generated first. Then, for each muon in the bundle, the distance from the shower axis, the energy and the coordinates of the impact point on the can surface are calculated. Since the multiplicity m of the bundle is generated according to the muon flux, it can happen that some muons in the bundle do not geometrically intercept the can surface. Therefore they are not written in the output file.

The output file thus contains all the information about each generated event: the coordinates of the muon impact point on the can surface, the direction cosines of the muon, the muon energy and the time delay at the can surface of the i^{th} muon in the

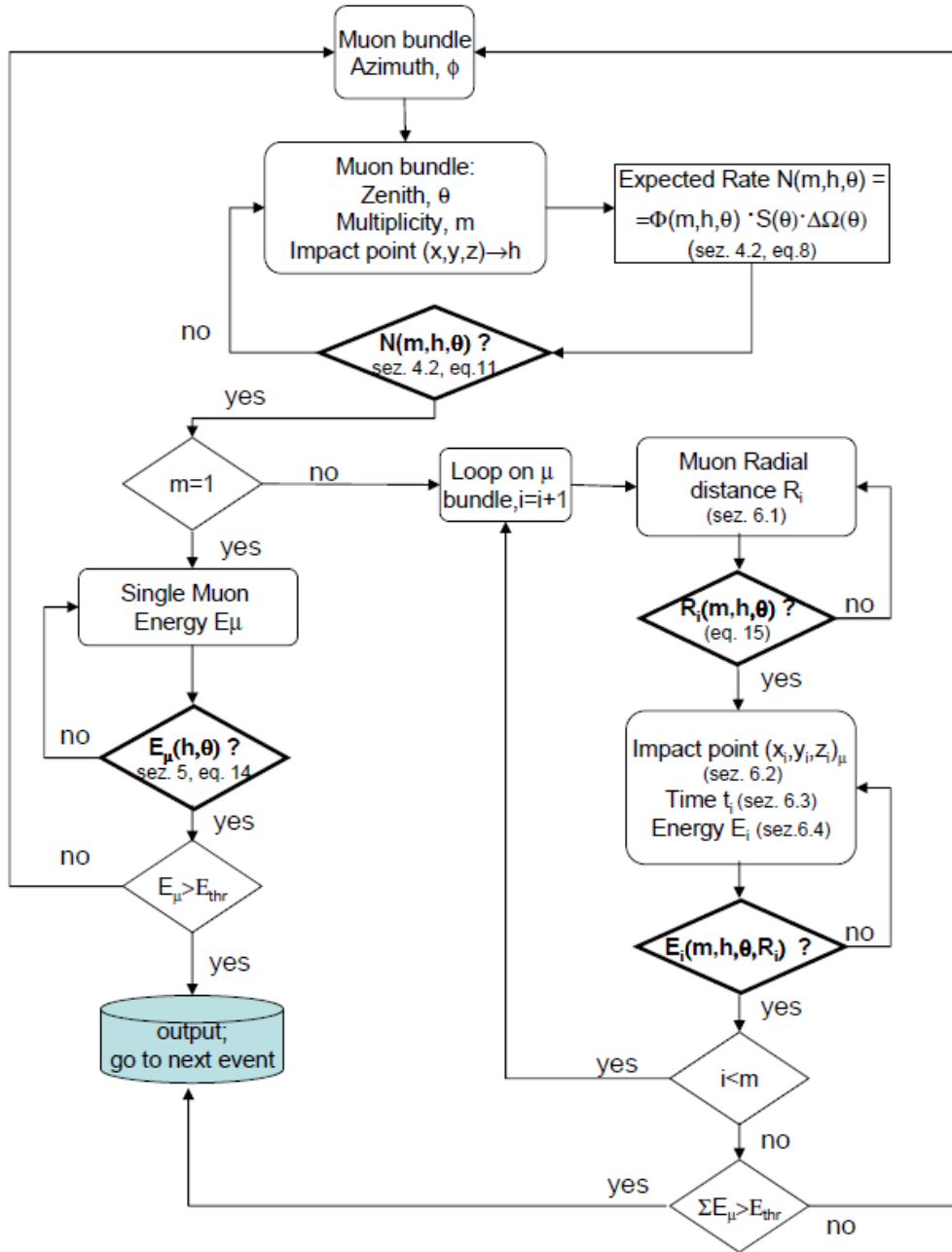


Figure 4.2: Flowchart of the MUPAGE event generator. The smooth-angle rectangles indicate the extraction of uniformly distributed random values. The decisional rhombuses in bold select values according to formulas reported in § 3.3.2, § 3.3.3 and § 3.3.4, with a Hit-or-Miss method. The procedure is iterated for N_{gen} events.

bundle with respect to the first muon in the same bundle ($i = 1$). It is assumed that all muons in the same bundle travel parallel to the shower axis with the speed of light, and that they intersect with any plane perpendicular to the shower axis at the same time.

Since MUPAGE generates the events according to their abundance, no weighting of the events is needed and the output file reproduces a real data file: Each set of events corresponds to a certain observation time period, the so-called *lifetime* (§ 4.5), which is reported in a second ASCII output file.

4.2 Generation of Muon Bundles on the Can Surface

4.2.1 Sampling of the Bundle Direction and of the Impact Point

As a first step, a generic bundle with muon multiplicity $m^* \in [m_{min}, m_{max}]^1$, random zenith angle $\theta^* \in [\theta_{min}, \theta_{max}]^2$ and azimuth angle $\phi \in [0, 2\pi]$ in the detector frame is generated. The zenith angle is defined as the angle with respect to the positive z -axis. The azimuth angle is the angle in the x - y plane. Variables that have to be selected by a Hit-or-Miss method, as described in the following, will be denoted with a *. The pseudorandom number generator used in the program is the Mersenne Twister algorithm [86] and it is included in the ROOT libraries (TRandom3 class) [48].

The bundle axis with direction (θ^*, ϕ) intercepts the can in a random point of coordinates (x^*, y^*, z^*) . To calculate this point, one has to generate first a random point (X_R, Y_R) in the plane perpendicular to the shower which includes the origin. As L_x and L_y in Figure 4.3 are defined as $L_x = 2R_{ext}$ and $L_y = H_{can} \sin \theta^* + 2R_{ext} \cos \theta^*$, the coordinates X_R and Y_R can assume the values:

$$-R_{ext} \leq X_R \leq R_{ext} \quad (4.1a)$$

$$-\left(\frac{H_{can}}{2} \sin \theta^* + R_{ext} \cos \theta^*\right) \leq Y_R \leq \frac{H_{can}}{2} \sin \theta^* + R_{ext} \cos \theta^* \quad (4.1b)$$

As muons are downward going particles, events on the lower disk of the can ($z^* = Z_{min}$ in Figure 4.1) are not considered. Therefore the point (X_R, Y_R) on the plane perpendicular to the shower direction can be on the upper disk or on the lateral surface of the can. It lies on the upper disk (grey area of Figure 4.3) if:

$$Y_R > \frac{H_{can}}{2} \sin \theta^* - R_{ext} \cos \theta^* \quad (4.2)$$

and

$$\frac{X_R^2}{R_{ext}^2} + \frac{[Y_R - (H_{can}/2) \sin \theta^*]^2}{(R_{ext} \cos \theta^*)^2} \leq 1 \quad (4.3)$$

¹ m_{min} and m_{max} are given as input parameters, as described in [56]. The default values are $m_{min} = 1$ and $m_{max} = 100$.

² θ_{min} and θ_{max} are given as input parameters, as described in [56]. Because MUPAGE is based on the parametric formulae described in § 3.3 and in [55], the validity range of zenith angle θ is $[0^\circ, 85^\circ]$.

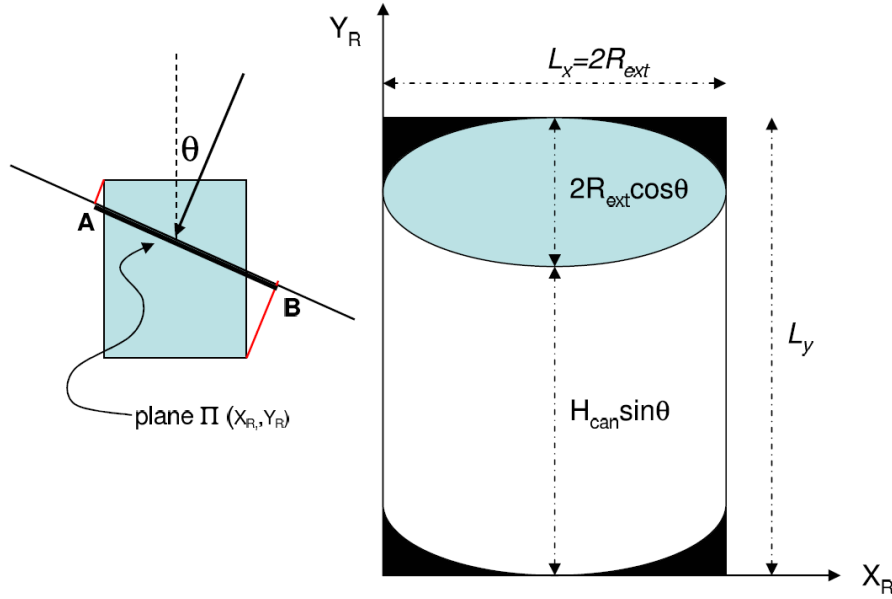


Figure 4.3: Left: sketch of the plane Π perpendicular to the shower axis. The muon bundle has zenith angle θ with respect to the detector z -axis. The interception point of the shower axis is uniformly distributed on the can projection on the plane Π and is generated outside the black region. The events generated in the grey area lie on the upper disk of the can; the events generated in the white are lie on the can lateral surface.

Therefore, if both conditions of Eqs. (4.2) and (4.3) are valid, the shower axis impacts on the upper disk of the can and its coordinates (x^*, y^*, z^*) are:

$$x^* = -X_R \quad (4.4a)$$

$$y^* = \frac{Y_R}{\cos \theta^*} - \frac{H_{can}}{2} \tan \theta^* \quad (4.4b)$$

$$z^* = Z_{max} \quad (4.4c)$$

Otherwise, i.e. if Eqs. (4.2) and (4.3) are not both valid, the shower axis hits the lateral surface. In this case, the intersection point has coordinates:

$$x^* = R_{ext} \cos \phi' \quad (4.5a)$$

$$y^* = R_{ext} \sin \phi' \quad (4.5b)$$

$$z^* = \frac{Y_R + \cos \theta^* \sqrt{R_{ext}^2 - X_R^2}}{\sin \theta^*} + \frac{Z_{min} + Z_{max}}{2} \quad (4.5c)$$

where $\phi' = \phi + \frac{3}{2}\pi - \arccos\left(-\frac{X_R}{R_{ext}}\right)$. The points (x^*, y^*, z^*) are distributed uniformly on the can surface (with the exclusion of the lower disk).

4.2.2 Hit-or-Miss Method to Sample the Impact Point

The procedure described in § 4.2.1 extracts uniformly h^* , θ^* and m^* , but the muon flux $\Phi(h, \theta, m)$, Eq. (3.10), decreases with increasing depth h , zenith angle θ and muon multiplicity m . A Hit-or-Miss method [85] is used to reproduce the correct dependence of the number of events on these variables. For each set of parameters (h^*, θ^*, m^*) , the number of events arriving on the projected area $S(\theta^*)$ in a small solid angle $\Delta\Omega(\theta^*)$ centered around θ^* is computed as:

$$N_{proj}(h^*, \theta^*, m^*) = \Phi(h^*, \theta^*, m^*) \cdot S(\theta^*) \cdot \Delta\Omega(\theta^*) \quad (4.6)$$

where

$$S(\theta^*) = \pi R_{ext}^2 \cdot \cos \theta^* + 2R_{ext}H_{can} \cdot \sin \theta^* \quad (4.7a)$$

$$\Delta\Omega(\theta^*) = 2\pi[\cos(\theta^* - 0.5^\circ) - \cos(\theta^* + 0.5^\circ)] \quad (4.7b)$$

A random number u is then generated according to:

$$0 < u < N_{max} \simeq \Phi(H_{min}, \theta_{min}, m_{min}) \cdot S(\theta') \cdot \Delta\Omega(\theta') \quad (4.8)$$

N_{max} corresponds to the set of values (h, θ, m) for which the function $\Phi(h, \theta, m) \cdot S(\theta) \cdot \Delta\Omega(\theta)$ is maximum. This function has a maximum for the minimum value of the detector depth ($h = H_{min}$), corresponding to the can upper disk, and for the minimum value of the range of muon multiplicities ($m = m_{min}$). The maximization in terms of the θ variable is more complex, due to the not trivial dependence of $\Phi(h, \theta, m) \cdot S(\theta) \cdot \Delta\Omega(\theta)$ on θ .

In order to save computing time, the maximum of $\Phi(H_{min}, \theta, m_{min}) \cdot S(\theta) \cdot \Delta\Omega(\theta)$ is computed as the product of the maximum of the functions $\Phi(H_{min}, \theta, m_{min})$ and $S(\theta) \cdot \Delta\Omega(\theta)$. The former has a maximum in correspondence of θ_{min} . The latter has a maximum, from Eqs. (4.7), for zenith angle

$$\theta' = \frac{\pi}{2} + \frac{1}{2} \arctan \left(-\frac{R_{ext}}{2H_{can}} \right) \quad (4.9)$$

Using this approximation, N_{max} is evaluated as in Eq. (4.8). The parameter set (h^*, θ^*, m^*) is accepted if:

$$u < N_{proj}(h^*, \theta^*, m^*) \quad (4.10)$$

In the following, to simplify the notation, (h, θ, m) will be used and the impact point coordinates become (x, y, z) .

Figure 4.4 shows that the number of generated events on the can surface decreases with increasing depth h , as expected.

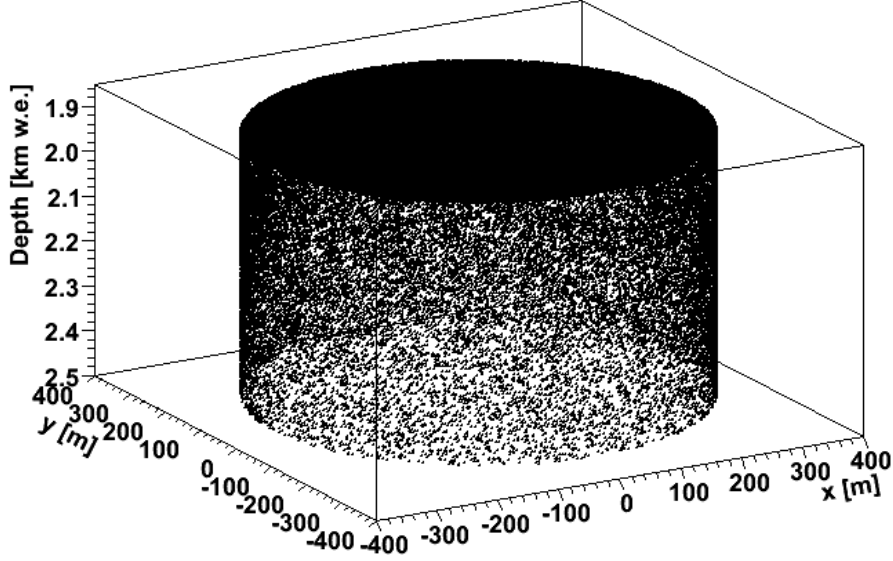


Figure 4.4: Events generated on the can surface of the ANTARES detector (see Chapter 2) after the application of the Hit-or-Miss method described in the text.

4.3 Single Muons

The underwater/ice flux of atmospheric muons is dominated by events reaching the detector with multiplicity $m = 1$, the so-called *single muons*. In this case the muon direction is assumed to be coincident with the shower axis and the impact point is (x, y, z) . The arrival time of the muon on the can surface is $t = 0$. The muon energy E is extracted according to Eq. (3.11), whose parameters depend on the vertical depth h of the impact point on the can surface and on the muon zenith angle θ .

A value of $\log_{10} E^*$ is randomly generated in the range between $\log_{10} E_{min} = -3$ and $\log_{10} E_{max} \sim 2.7$ ($E_{min} = 0.001$ TeV and $E_{max} = 500$ TeV). The value E^* is accepted (or rejected) according to the Hit-or-Miss method: a random number u' is generated between 0 and the maximum of Eq. (3.11) at depth h and zenith θ :

$$0 < u' < \left(\frac{dN}{d(\log_{10} E_\mu)} \right) (h, \theta; E_\mu^{max}) \quad (4.11)$$

The maximum of Eq. (3.11) corresponds to $E_\mu^{max} = \frac{\epsilon(1 - e^{-bX})}{\gamma - 1}$, where ϵ defines the critical energy below which continuous ionization loss is more important than radiative losses (parameters a and b , respectively, of Eq. (3.9)), and γ is the spectral index of the primary cosmic rays (Eq. 3.11). The value E^* is accepted if:

$$u' < \frac{dN}{d(\log_{10} E_\mu)} (h, \theta; E^*) \quad (4.12)$$

4.4 Multiple Muons

4.4.1 Radial Distance of Muons with Respect to the Bundle Axis

For events with muon multiplicity $m > 1$, the distance R of each muon from the bundle axis (in a plane perpendicular to the axis) is calculated, according to the radial distribution, Eq. (3.12). R depends on the depth h , the bundle multiplicity m and the zenith angle θ . It is useful to define a new reference frame *Bundle Axis Frame*, shortened as *BAF*, where the z_{BAF} -axis points in the direction of the shower axis (Figure 4.5). Each muon is located in a point (X, Y) of the plane Π perpendicular to the shower axis. The distance of the point (X, Y) from the origin of the *BAF* is called R_i (the muon radial distance). R_i^* is sampled randomly between R_{min} and R_{max} (both values from input parameters). The Hit-or-Miss method is used to accept (or reject) the value R_i^* . A random number u'' is generated between 0 and the maximum of the lateral distribution function (dN/dR) at the given h , θ and m . R_i^* is accepted if:

$$u'' < \frac{dN}{dR}(h, \theta, m, R_i^*) \quad (4.13)$$

The coordinates in the *BAF* are computed from the selected R_i as $X = R_i \cdot \cos \beta$ and $Y = R_i \cdot \sin \beta$, where β is a random number between 0 and 2π .

4.4.2 Coordinates of the Multiple Muons on the Can Surface

The shower axis (*SA*) intercepts the can in the impact point (computed in § 4.2.1) with coordinates $(x, y, z) = (x_{SA}, y_{SA}, z_{SA})$. Then, referring to Figure 4.5, for each muon in the bundle:

- (X, Y) = coordinates of the muon in the *BAF*;
- (x_μ, y_μ, z_μ) = coordinates of the muon in the laboratory frame;
- $(v_x, v_y, v_z) \equiv (\sin \theta \cos \phi, \sin \theta \sin \phi, \cos \theta)$ = direction of the muon in the laboratory frame;
- (x_i, y_i, z_i) = projection of the point (x_μ, y_μ, z_μ) on the can surface.

When the point (X, Y) in the *BAF* is known, the point (x_μ, y_μ, z_μ) in the laboratory frame can be computed using a general matrix \mathbf{A} resulting from the composition of three rotations [87]. In the so-called ‘X-convention’ the rotations are defined by the Euler angles (Φ, Θ, Ψ) , where the first rotation is by an angle Φ around the z -axis, the second one is by an angle $\Theta \in [0, \pi]$ around the x -axis and the third one is by an angle Ψ around the z -axis

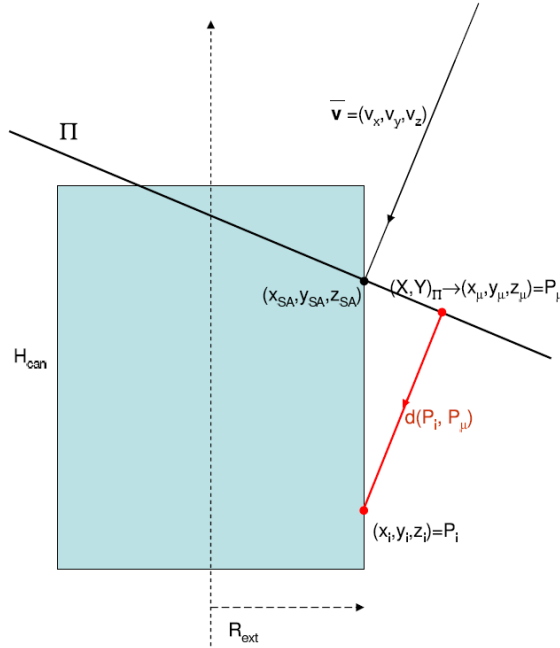


Figure 4.5: Lateral view of the can (the rectangle). The shower axis has direction (v_x, v_y, v_z) and intercepts the detector in the point (x_{SA}, y_{SA}, z_{SA}) . m muons are generated on the plane Π perpendicular to the shower axis and $m_c \leq m$ intercept the can. A muon has coordinates (X, Y) in the *BAF* and $(x_{\mu}, y_{\mu}, z_{\mu})$ in the laboratory frame. The point (x_i, y_i, z_i) is the projection of the point $(x_{\mu}, y_{\mu}, z_{\mu})$ along the muon direction on the can. The time delay of each muon is evaluated from the distance between the points (x_i, y_i, z_i) and $(x_{\mu}, y_{\mu}, z_{\mu})$.

(again). There is a univocal relationship between the three Euler angles and the zenith (θ) and azimuth (ϕ) angles:

$$\Phi = -\pi/2 \quad (4.14a)$$

$$\Theta = \theta \quad (4.14b)$$

$$\Psi = \phi + \pi/2 \quad (4.14c)$$

The transformation of the point (X, Y) in the *BAF* into the point $(x_{\mu}, y_{\mu}, z_{\mu})$ in the laboratory frame is defined as:

$$\begin{pmatrix} x_{\mu} \\ y_{\mu} \\ z_{\mu} \end{pmatrix} = \mathbf{A} \begin{pmatrix} X \\ Y \\ 0 \end{pmatrix} \quad (4.15)$$

where the matrix \mathbf{A} is related to the Euler angles according to [87]

$$\mathbf{A} = \begin{pmatrix} \cos \Phi \cos \Psi - \cos \Theta \sin \Phi \sin \Psi & \cos \Phi \sin \Psi + \cos \Theta \sin \Phi \cos \Psi & \sin \Theta \sin \Phi \\ -\sin \Phi \cos \Psi - \cos \Theta \cos \Phi \sin \Psi & -\sin \Phi \sin \Psi + \cos \Theta \cos \Phi \cos \Psi & \sin \Theta \cos \Phi \\ \sin \Theta \sin \Psi & -\sin \Theta \cos \Psi & \cos \Theta \end{pmatrix}$$

The coordinates of the impact point of each muon on the can are obtained using the projection of each point (x_μ, y_μ, z_μ) along the direction (v_x, v_y, v_z) . This is done using the straight line defined by the three parametric equations $(x_i, y_i, z_i) = (x_\mu, y_\mu, z_\mu) + k(v_x, v_y, v_z)$, where $k = (Z_{max} - z_\mu)/v_z$.

The impact point of the i^{th} muon in the bundle is on the upper disk of the can if the straight line intercepts the plane $z = Z_{max}$ with $x_i^2 + y_i^2 \leq R_{ext}^2$. In this case, the coordinates are:

$$(x_i, y_i, z_i) = (x_\mu + kv_x, y_\mu + kv_y, Z_{max}) \quad (4.16)$$

If $x_i^2 + y_i^2 > R_{ext}^2$, the impact point (x_i, y_i, z_i) lies on the can lateral surface or it does not intercept the can at all.

The intersection of the straight line with the lateral surface of the can (defined by equation $x^2 + y^2 = R_{ext}^2$) gives a second degree equation $a\Lambda^2 + 2b\Lambda + c = 0$, with $a = v_x^2 + v_y^2$, $b = v_x x_\mu + v_y y_\mu$ and $c = x_\mu^2 + y_\mu^2 - R_{ext}^2$. The solutions are $\Lambda_\pm = (-b \pm \sqrt{\Delta})/a$, with $\Delta = b^2 - ac$. If $\Delta < 0$, the i^{th} muon does not intercept the can. For $\Delta \geq 0$ the two possible impact points are:

$$(x_i, y_i, z_i) = (x_\mu + \Lambda_+ v_x, y_\mu + \Lambda_+ v_y, z_\mu + \Lambda_+ v_z) \quad (4.17a)$$

$$(x_i, y_i, z_i) = (x_\mu + \Lambda_- v_x, y_\mu + \Lambda_- v_y, z_\mu + \Lambda_- v_z) \quad (4.17b)$$

As atmospheric muons are downward going, the solution with the larger value z_i is chosen. If $z_i < Z_{min}$, the i^{th} muon does not intercept the can. The number of muons intercepting the can surface determines the bundle multiplicity $m_c \leq m$ at the can.

4.4.3 Arrival Time of the Muons in the Bundle

All muons in the bundle are assumed to arrive at the same time on the plane Π perpendicular to the shower axis. In general, each muon reaches the can surface at a different time.

The distance between the impact point of the i^{th} muon $P_i(x_i, y_i, z_i)$ and the coordinates of that muon on the plane Π in the laboratory frame $P_\mu(x_\mu, y_\mu, z_\mu)$ is:

$$d(P_i, P_\mu) = \text{sign} \cdot \sqrt{(x_i - x_\mu)^2 + (y_i - y_\mu)^2 + (z_i - z_\mu)^2} \quad (4.18)$$

The arrival time of the first muon in the list ($i = 1$) on the can surface is taken as $t_1 = 0$. All the remaining muons, labeled with $i = 2, \dots, m_c$, can intercept the can earlier ($t_i < 0$) or later ($t_i > 0$). The relative time is computed from the distance $d(P_i, P_\mu)$ defined by Eq. (4.18). Since distances are intrinsically positive, the evaluation of the relative delay

between muons in the bundle requires the definition of the sign in Eq. (4.18). Referring to Figure 4.5, if $z_\mu < z_i$ the distance is assumed positive ($sign = 1$), otherwise it is negative ($sign = -1$). The delay t_i of the i^{th} muon with respect to the first one is:

$$t_i = \frac{d(P_i, P_\mu) - d(P_1, P_{\mu 1})}{c} \quad (4.19)$$

where c is the speed of light. Since the distances can be either positive or negative, also t_i (in ns) will assume either positive or negative values.

4.4.4 Muon Energy for MultimMuon Events

The last step is the choice of the energy of each muon in a multimMuon bundle according to the energy distribution, Eq. (3.11). The muon energy extracted from this distribution depends on vertical depth h , zenith angle θ , on the multiplicity m of the shower and on the radial distance R of the muon from the shower axis. The steps described in § 4.3 for the energy of single muons are repeated for the evaluation of the energy of each muon in the bundle.

4.5 Livetime of the Simulation

MUPAGE automatically computes the detector livetime corresponding to the number of generated events N_{gen} on the can surface. The number of simulated events $N(\Delta\Omega_i)$ in a small solid angle $\Delta\Omega_i = 2\pi(\cos\theta_{1i} - \cos\theta_{2i})$, with multiplicity $m = m_{min}$ and with shower axis intercepting the can upper disk, are evaluated in 33 bins¹. The expected rate of muon events with multiplicity m_{min} on the can upper disk with area πR_{ext}^2 at the depth H_{min} , and in the solid angle $\Delta\Omega_i$ is:

$$\dot{N}_{MC}(\Delta\Omega_i) = \Phi(H_{min}, \theta_i, m_{min}) \cdot S \cdot \Delta\Omega_i \quad [\text{s}^{-1}] \quad (4.20)$$

where $\theta_i = (\theta_{1i} + \theta_{2i})/2$, and $S = \pi R_{ext}^2 \cos\theta_i$ [m²] is the projected area of the upper disk. The equivalent livetime for each bin is:

$$T(\Delta\Omega_i) = N(\Delta\Omega_i) / \dot{N}_{MC}(\Delta\Omega_i) \quad [\text{s}] \quad (4.21)$$

The livetime with its statistical error is computed as the weighted average of the 33 different solid angle regions of $T(\Delta\Omega_i)$, which have the same value, within statistical errors.

¹The first bin is $0^\circ < \theta < 10^\circ$, then 30 bins of 2 degrees are considered. The last two bins are $70^\circ < \theta < 76^\circ$ and $76^\circ < \theta < 85^\circ$, respectively. The bin size was chosen in order to have a constant or at least an adequate statistical sample in each bin.

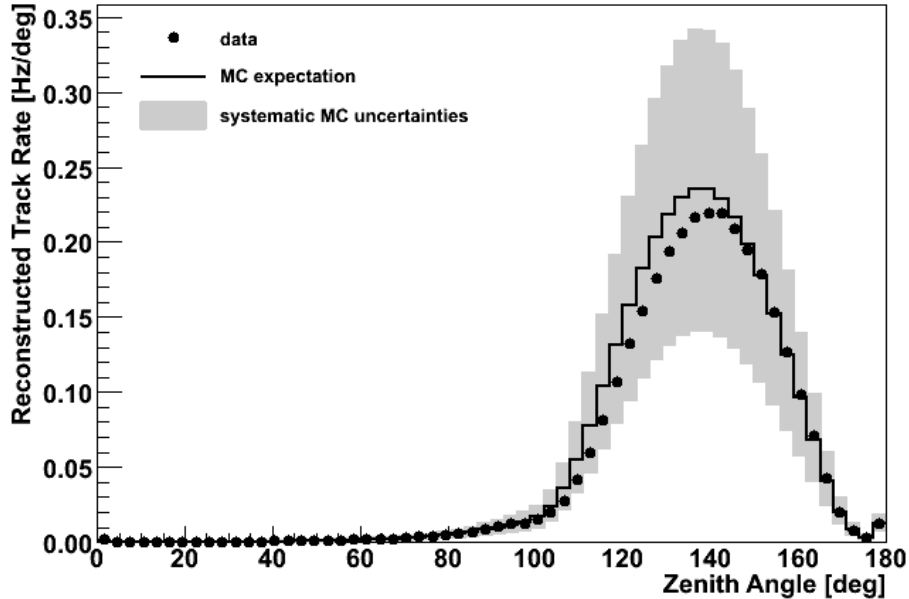


Figure 4.6: Zenith angle distribution of reconstructed tracks. Black points represent data. The solid line corresponds to the simulation with MUPAGE as event generator. The grey band represents the systematic uncertainties, with respect to the solid line.

4.6 Comparison of Angular Distributions with ANTARES data

Using MUPAGE as event generator, the angular distributions of the reconstructed atmospheric muon tracks have been computed. The entire Monte Carlo chain includes the production of Cherenkov light in water, the simulation of the signal on the PMTs, the trigger selection and the application of the reconstruction algorithm, using the codes described in Appendix A.

In order to save computing time, two different samples have been performed, which are the official MUPAGE production available within the ANTARES Collaboration. The first sample includes 312 files with muon multiplicity up to 100, which corresponds to about 1.6×10^9 atmospheric bundles generated on the can surface, with a livetime equivalent to about 30 effective days. The second sample includes 1 file with muon multiplicity between 101 and 1000, which corresponds to 5×10^4 atmospheric bundles generated on the can surface, with a livetime equivalent to about 36 effective days.

To simulate the background noise due to ^{40}K decay and bioluminescence (§ 2.6), the run 38712 acquired on November 18th 2008 has been implemented in the trigger algorithm (§ A.3). For this run, the baseline rate is 63 kHz and the burst fraction is 17%.

To compare the Monte Carlo angular distributions with data, a data sample taken

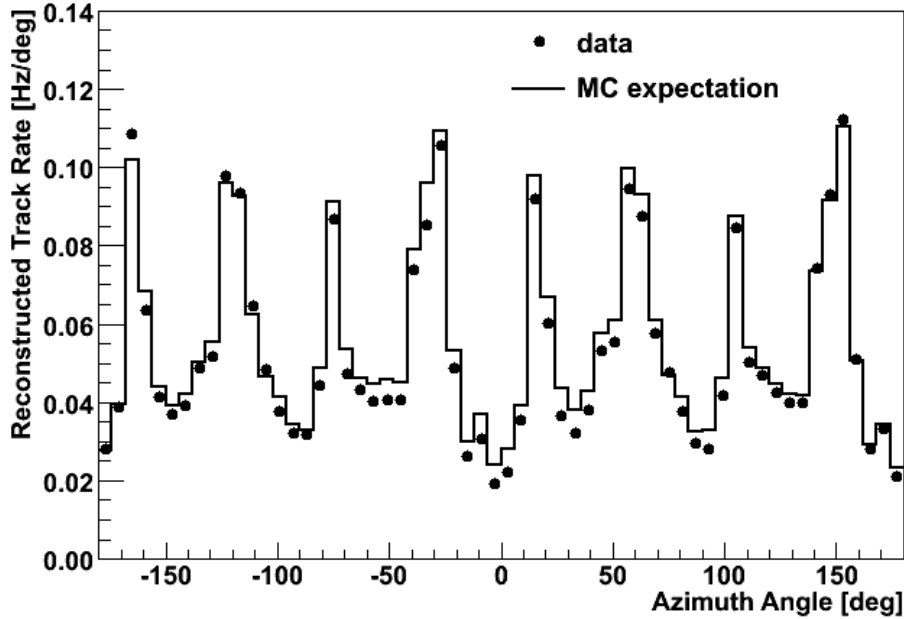


Figure 4.7: Azimuth angle distribution of reconstructed tracks. Black points represent data. The solid line corresponds to the simulation with MUPAGE as event generator.

around November 18th 2008 is considered, in order to avoid biasing due to a different configuration of the detector or a different background. Between all runs acquired on that period, only runs which fulfill the following quality criteria have been selected:

- at least 700 out of 885 installed optical modules are active during a run ($\sim 80\%$);
- the baseline rate (§ 2.6) is below 120 kHz;
- the burst fraction (§ 2.6) is less than 20%.

The 18 selected runs correspond to an active detector time of about 1.2 effective days.

Figure 4.6 shows the zenith angle distribution of the reconstructed tracks. The systematic errors on the Monte Carlo expectations are due to uncertainties in the detector description and in the knowledge of the environmental parameters. In a study made for the 5 Line setup of the ANTARES detector [88], the overall uncertainty on the total number of reconstructed tracks is estimated as $^{+45\%}_{-40\%}$. This evaluation is overestimated for the 12 Line configuration, and a new analysis of systematic uncertainties is in progress. The reconstructed event rate is 3.1 Hz in the data and 3.3 Hz in the Monte Carlo sample.

As mentioned in § 3.2, the uncertainties due to the primary cosmic ray composition and hadronic interaction models (not included in grey band of Figure 4.6) affect the Monte Carlo expectations up to 30%.

Figure 4.7 shows the azimuth angle distribution of the reconstructed tracks. Although the azimuth angle distribution is uniform for atmospheric muons which do not have a favorite direction, the structure of the ANTARES detector (Figure 2.6) clearly favors certain azimuth angles over others. To emphasize this effect, the systematic errors are not included in the plot.

Chapter 5

Ultra High Energy Neutrinos

Assuming that at acceleration sites a fraction of high energy cosmic rays interacts with the ambient matter or photon fields, TeV γ -rays are produced by the π^0 decay, while neutrinos are produced by charged pion decay. This is the so-called *astrophysical hadronic model*. In this framework, the energy spectrum of secondary particles follows the same power-law of the progenitor cosmic rays and it is possible to constrain the expected neutrino flux from sources where γ -rays are observed. Due to this connection between cosmic rays, neutrinos and γ -rays, it is also possible to put upper bounds on the expected neutrino flux from extragalactic sources, since the neutrino generation rate will never exceed the generation rate of high energy protons. Indeed, neutrinos due to their neutral nature cannot be directly accelerated.

In addition to stars, the Galaxy contains interstellar thermal gas, magnetic fields and cosmic rays which have roughly the same energy density. The inhomogeneous magnetic fields diffusively confine the cosmic rays within the Galaxy. Cosmic ray hadronic interaction with the interstellar medium produce a diffuse flux of γ -rays and neutrinos (expected to be equal within a factor of roughly 2). The flux at Earth is expected to be correlated to the gas column density in the Galaxy: the largest emission is expected from directions along the line of sight which intersects most matter [28].

Apart from atmospheric muons, other sources of background for the study of the diffuse neutrino flux are atmospheric neutrinos, which are described in § 5.1. A particular theoretical upper bound on the diffuse neutrino flux, the so-called Waxman-Bahcall limit, is discussed in § 5.2. In a detailed calculation of the upper limit of the diffuse flux of high energy neutrinos, the neutrino oscillation effects (§ 5.3) have to be taken into account. § 5.4 describes the neutrino interactions with matter, while § 5.5 discusses the attenuation of the neutrino flux due to propagation through the Earth.

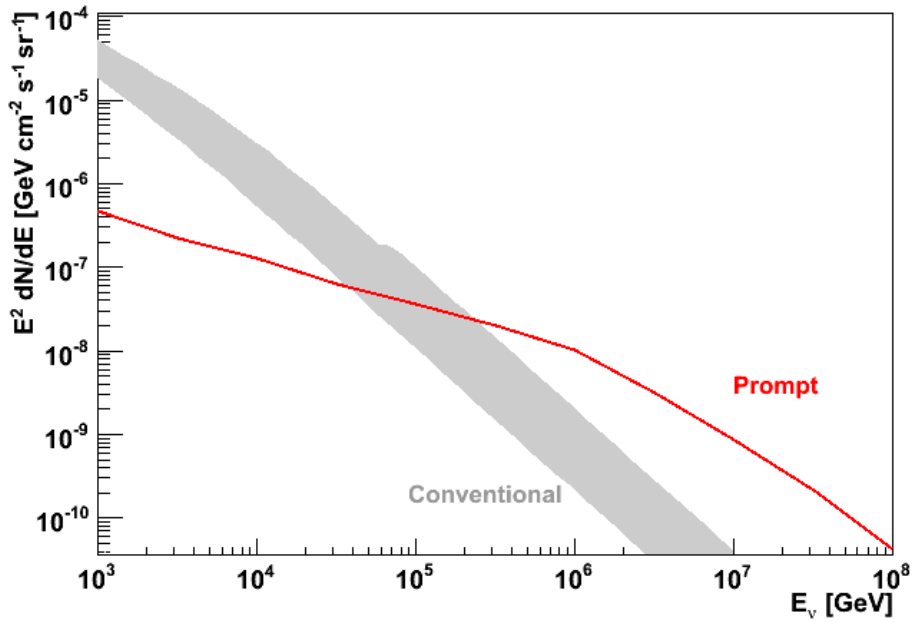


Figure 5.1: Atmospheric *conventional* muon neutrino flux parameterized by Bartol [57] (in gray) and *prompt* neutrino flux according to the RQPM charm production model [90] (in red).

5.1 Atmospheric Neutrinos

Atmospheric neutrinos originate from the interaction of primary cosmic rays with the terrestrial atmosphere (§ 3.1). The decays in flight of charged pions and kaons, Eqs. (3.1), (3.2) and (3.3), often referred to as the *conventional* atmospheric lepton flux, dominates to about 1–10 TeV. Above this energy range, the dominant sources are the semileptonic decays of very short-lived charmed particles like D and Λ , Eqs. (3.4), (3.5) and (3.6). The latter is known as the *prompt* atmospheric lepton flux. Whereas cosmic neutrinos reflect the cosmic ray spectrum near the source ($dN/dE \propto E^{-2}$), as described in § 1.1, the atmospheric neutrino spectrum is proportional to $E^{-3.6}$ (above 100 GeV), almost two powers of the energy steeper than the cosmic ray spectrum.

Currently the most commonly used conventional atmospheric neutrino flux calculation is the Bartol group neutrino flux [57]. The Bartol model assumes that neutrinos travel in the same direction as their primaries.

In [89] a review of different models describes prompt lepton production, including prompt neutrinos. Among these charm production models, the highest prompt neutrino production model is considered in this thesis: the Recombination Quark Parton Model (RQPM) [90]. It is a phenomenological non-perturbative model, taking into account the intrinsic charm contribution, in which a $c\bar{c}$ is coupled to more than one constituent of the

projectile hadron.

Since the prompt lepton flux is almost independent of lepton flavor, detection depth and zenith angle, Figure 5.1 shows just a line using the muon neutrino vertical flux at sea level. Instead, the Bartol flux depends on the lepton flavor as well as the zenith angle and is therefore represented by a shaded band. The lower limit of the band represents the flux from the vertical direction, while the upper limit is the flux from the horizontal direction. Furthermore, the conventional flux takes into account the propagation through the Earth (§ 5.5).

5.2 Diffuse Neutrino Flux

As already mentioned in § 1.4.1, a possible way to observe extragalactic neutrino sources is through the measurement of the cumulative flux in the whole sky. The only way to detect this diffuse flux of high energy neutrinos is by looking for a surplus of high energy events in the measured energy spectrum over the background of the atmospheric neutrinos.

Theoretical models can derive upper bounds on the high energy neutrino flux produced in astronomical sources, by using the observation of the diffuse fluxes of γ -rays and UHECR. One of these bounds, the Waxman-Bahcall (W&B) bound [29] is based on the fluxes of cosmic rays measured at Earth at energies between 10^{16} and 10^{20} eV, and is used as a reference bound on the neutrino flux coming from different extragalactic sources.

W&B pointed out that cosmic ray observations set a model-independent upper bound on the intensity of high energy neutrinos produced by photo-meson interactions in sources with a size not much larger than the proton photo-meson mean free path. This bound applies, in particular, to neutrino production by either AGN or GRBs. It is assumed that the spectral shape of cosmic rays up to the GZK cutoff is $dN/dE \propto E^{-2}$, as typically expected from the Fermi acceleration mechanism. The limit is numerically derived by assuming that all of the energy of the high energy protons produced in the astronomical sources is transferred in photo-pion or nucleon-proton interactions and that the neutrinos produced by the decay of charged pions carry 5% of the proton energy. The W&B limit is considered a rather loose bound, since the charged pion produced by photo-pion interactions actually receives only about 20% of the initial proton energy.

W&B computed the upper limit of muon neutrino ($\nu_\mu + \bar{\nu}_\mu$) flux, already reported in Eq. (1.6) and re-written here for convenience, as:

$$E_\nu^2 \frac{dN_\nu}{dE_\nu} < 4.5 \times 10^{-8} \text{ GeV cm}^{-2} \text{ s}^{-1} \text{ sr}^{-1} \quad (5.1)$$

taking also into account the redshift energy loss of neutrinos.

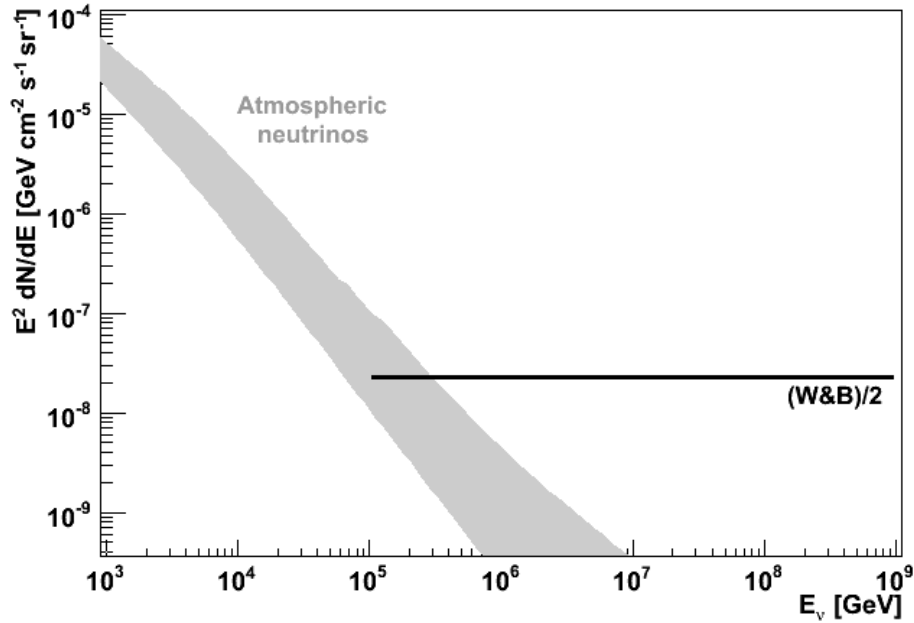


Figure 5.2: Atmospheric conventional and prompt muon neutrino flux (in gray) and Waxman-Bahcall (W&B) upper limit for a E^{-2} diffuse flux of high energy neutrinos of one flavor (in black). The upper limit is divided by two to take into account the neutrino oscillation effects (see Eq. (5.8) in § 5.3).

Using observational constraints, they also showed that neither magnetic fields in the source nor intergalactic magnetic fields affect the upper bound.

Figure 5.2 shows the W&B upper limit for a E^{-2} diffuse flux of high energy muon neutrinos. In order to take into account the neutrino oscillation effects on the flux (described in § 5.3), the upper bound has been divided by two. For comparison, the atmospheric (conventional and prompt) muon neutrino flux (§ 5.1) is shown as a shaded band. This flux takes already into account the propagation through the Earth (§ 5.5). The lower limit of the band represents the flux from the vertical direction, while the upper limit is the flux from the horizontal direction.

5.3 Neutrino Oscillation Effects on the Diffuse Neutrino Flux

As already mentioned in § 1.2, high energy neutrinos are produced in astrophysical sources mainly through the decay of charged pions, e.g. $\pi^+ \rightarrow \mu^+ + \nu_\mu \rightarrow e^+ + \nu_e + \bar{\nu}_\mu + \nu_\mu$ (Eq. 1.5). Therefore, neutrino fluxes of different flavors at the source are expected to be in the ratio ($\nu_l + \bar{\nu}_l$ combined)

$$\nu_e : \nu_\mu : \nu_\tau = 1 : 2 : 0 \quad (5.2)$$

However, neutrino oscillations induce flavor changes while neutrinos propagate in vacuum or in matter. Neutrino oscillations were observed in atmospheric neutrinos, in solar neutrino experiments and on Earth based accelerator and reactor experiments. A complete review about neutrino oscillations can be found e.g. in [91].

If neutrinos have masses, then there is a spectrum of three neutrino mass eigenstates, ν_i ($i = 1, 2, 3$), that are the analogues of the charged lepton mass eigenstates, l ($l = e, \mu, \tau$). The superposition of neutrino mass eigenstates ν_i gives the weak flavor eigenstates ν_l through the elements of the unitary neutrino mixing matrix U , the so-called Pontecorvo-Maki-Nakagawa-Sakata matrix [92]:

$$|\nu_l\rangle = \sum_i U_{li}^* |\nu_i\rangle \quad (5.3)$$

On Earth, all oscillations are averaged out, so that the probability of a neutrino changing flavor from α to β is given by [93]:

$$P(\nu_\alpha \rightarrow \nu_\beta) = \sum_i |U_{\alpha i}^*|^2 e^{-im_i^2 L/2E} |U_{\beta i}|^2 \quad (5.4)$$

where L is the distance traveled by the neutrino from production to detection and E is the neutrino energy. Assuming CPT invariance, the probability for oscillation of an antineutrino is the same as that for a neutrino (except that the mixing matrix U is replaced by its complex conjugate).

In the special case where only two mass eigenstates (e.g. ν_2, ν_3), two flavor eigenstates (e.g. ν_μ, ν_τ), and one mixing angle (e.g. θ_{23}) are involved, the unitary mixing matrix U takes the form

$$U = \begin{matrix} \nu_\mu \\ \nu_\tau \end{matrix} \begin{bmatrix} \nu_2 \cos \theta_{23} & \nu_3 \sin \theta_{23} \\ -\nu_2 \sin \theta_{23} & \nu_3 \cos \theta_{23} \end{bmatrix} \quad (5.5)$$

Hence, the probability that a muon neutrino ν_μ changes flavor in a tau neutrino ν_τ is:

$$P(\nu_\mu \rightarrow \nu_\tau) = \sin^2 2\theta_{23} \sin^2 \left(1.27 \Delta m^2 \frac{L}{E} \right) \quad (5.6)$$

and the survival probability for a pure ν_μ beam is:

$$P(\nu_\mu \rightarrow \nu_\mu) = 1 - \sin^2 2\theta_{23} \sin^2 \left(1.27 \Delta m^2 \frac{L}{E} \right) \quad (5.7)$$

where $\Delta m^2 = m_3^2 - m_2^2$ is in units of eV^2/c^4 , L is in units of km and E is in units of GeV.

According to the neutrino oscillation parameters Δm^2 and the mixing angles θ , the flavor ratio of neutrinos at the astrophysical origin, Eq. (5.2), changes to the flavor ratio observed on Earth as:

$$\nu_e : \nu_\mu : \nu_\tau = 1 : 1 : 1 \quad (5.8)$$

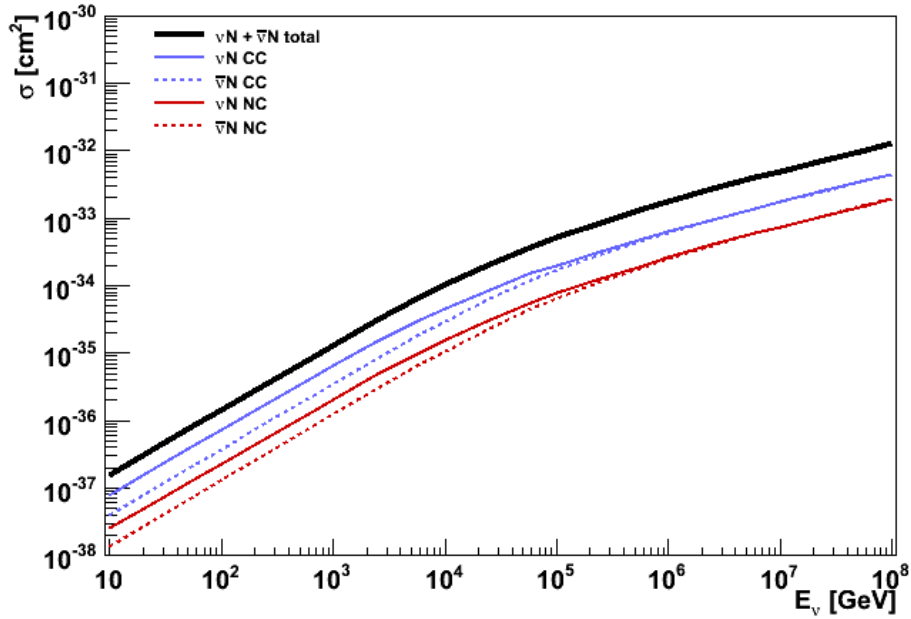


Figure 5.3: Charged current (blue lines) and neutral current (red lines) cross sections for neutrino (solid lines) and antineutrino (dashed lines) interactions on isoscalar nucleon targets, according to the CTEQ6-DIS parton distributions [96]. The thick black solid line represents the sum of the four reactions.

5.4 Neutrino Interactions

Neutrino interactions with matter are to a large extent dominated by the inelastic neutrino scattering on atomic nuclei, for which the cross section is generally several orders of magnitude larger than for the interaction between neutrinos and atomic electrons. An exception to this is the so-called Glashow resonance, which is discussed below.

Neutrinos can interact with a nucleon via weak interactions by exchanging a charged W -boson in the *charged current* (CC) interaction

$$\nu_l + N \rightarrow W^- \rightarrow l^- + X \quad (5.9a)$$

$$\bar{\nu}_l + N \rightarrow W^+ \rightarrow l^+ + X \quad (5.9b)$$

or by exchanging a neutral Z -boson in the *neutral current* (NC) interaction

$$\nu_l + N \rightarrow Z^0 \rightarrow \nu_l + X \quad (5.10a)$$

$$\bar{\nu}_l + N \rightarrow Z^0 \rightarrow \bar{\nu}_l + X \quad (5.10b)$$

where $N \equiv (\text{neutron} + \text{proton})/2$ is an isoscalar nucleon.

Details on calculations of the cross sections for deep inelastic neutrino-nucleon scattering at neutrino energies between 10^9 and 10^{21} eV are presented in [94]. These calculations

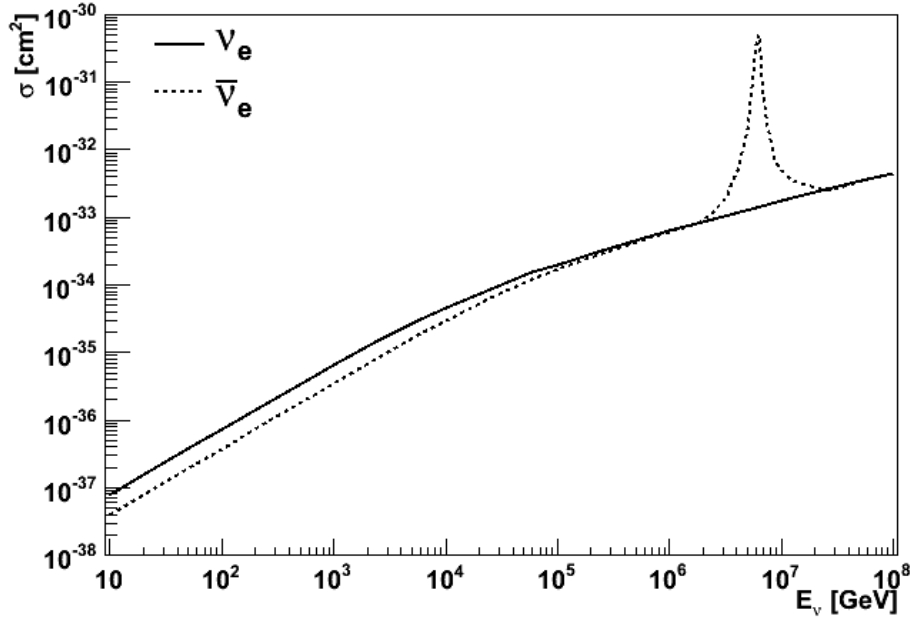


Figure 5.4: Cross sections for electron neutrino interactions (solid line) and for anti-electron neutrino interactions (dashed line) on atomic nuclei and electrons, according to the CTEQ6-DIS parton distributions [96]. The contribution of the neutrino-electron scattering at the Glashow resonance is clearly visible in the antineutrino distribution.

are based on the CTEQ4-DIS (Deep Inelastic Scattering) parton distributions [95]. The current version (CTEQ6 [96]) of the parton distributions takes into account the most recent experimental results, but in the calculations of the deep inelastic scattering does not differ from the previous ones.

Figure 5.3 shows the cross sections for the CC and NC reactions, Eqs. (5.9) and (5.10), of the muon neutrino (solid lines) and anti-muon neutrino (dotted lines) on isoscalar nucleon targets as a function of the neutrino energy E_ν . The thick solid line represents the sum of all reactions. The difference between the neutrino and antineutrino cross sections are due to dynamics of the weak interactions and the dominance of the valence quarks. At low energies the cross sections rise linearly with E_ν . For energies exceeding about 10^4 GeV, the cross sections are damped by the W -boson propagator. For the range of neutrino energies of interest here, the cross sections for reactions involving electron neutrinos are identical to those of muon neutrinos.

Because of the small electron mass, neutrino-electron interactions can generally be neglected with respect to neutrino-nucleon interactions. There is however an exceptional case: resonant formation of the intermediate boson W^- in $\bar{\nu}_e e$ interactions at 6.3 PeV ($E_\nu^{\text{res}} = M_W^2/2m_e = 6.3 \times 10^6$ GeV), also known as the Glashow resonance [97]. Figure 5.4

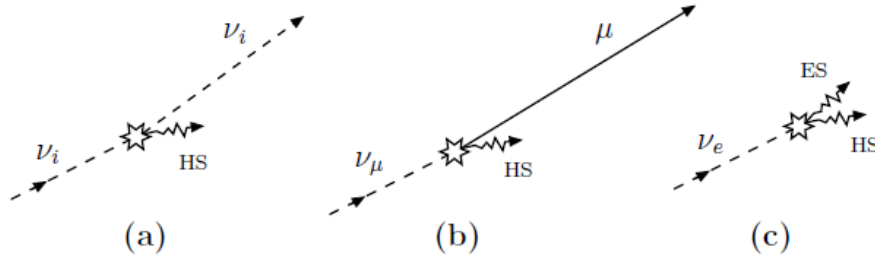


Figure 5.5: Neutrino interaction signatures: ν_i -nucleon NC interaction (a), ν_μ -nucleon CC interaction (b), ν_e -nucleon CC interaction (c).

shows the cross sections for electron neutrino interactions with atomic nuclei and electrons (solid line), in which the neutrino-nucleon interactions dominate, and for anti-electron neutrino interactions with atomic nuclei and electrons (dashed line), in which the contribution of the neutrino-electron interactions rules in the neighborhood of the Glashow resonance.

The NC and CC interactions result in different signatures in the detector, as shown in Figure 5.5. The case of CC interactions of tau neutrinos is not discussed in this thesis. For $E_\nu > 10$ GeV, the interaction will disintegrate the nucleus and produce a hadronic shower (HS). In water, a hadronic shower can travel up to few tens of meters. In the case of an NC interaction, this is the only signal produced, as the outgoing neutrino will escape the detector medium without interacting another time. In the case of a CC interaction, the signature depends on the flavor of the outgoing lepton which is determined by the flavor of the neutrino. In the case of an electron neutrino, the outgoing electron will quickly lose its energy in the medium, resulting in an electromagnetic shower (ES). The spatial dimensions of an electromagnetic shower are similar to a hadronic shower. In the case of a muon neutrino, the outgoing muon has a much larger mass than an electron and a considerable lifetime of $2 \cdot 10^{-6}$ s. This enables a muon to travel up to 10 km before it decays.

5.5 Earth's Opacity to Neutrinos

The rise of the CC and NC cross sections with energy is mirrored in the decrease of the (water-equivalent) interaction length [98]

$$\mathcal{L}_{\text{int}} = \frac{1}{\sigma_{\nu N}(E_\nu) N_A} \quad (5.11)$$

where $N_A = 6.022 \times 10^{23} \text{ cm}^{-3}$ w.e. is Avogadro's number. The energy dependence of the interaction lengths for neutrinos and antineutrinos on nucleons is shown in Figure 5.6.

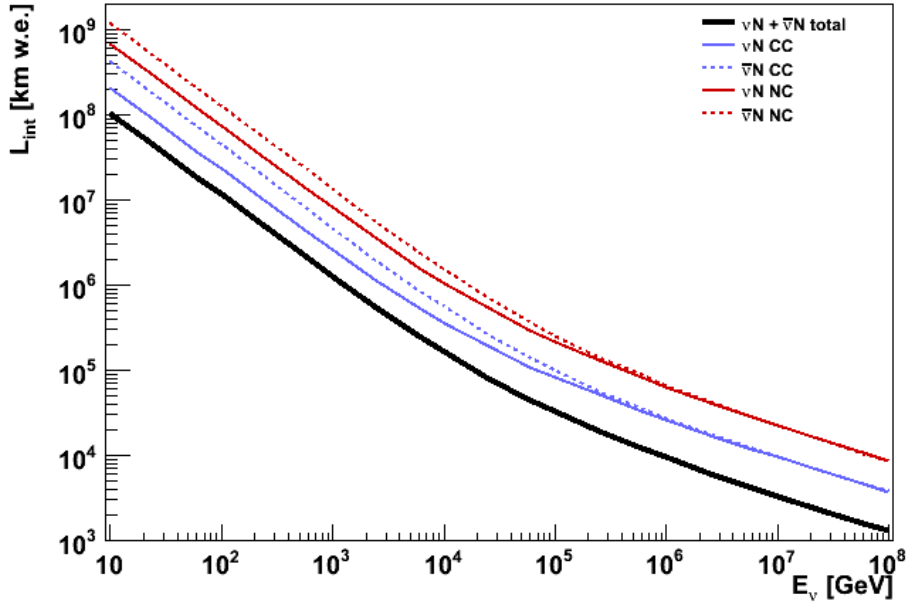


Figure 5.6: Charged current (blue lines) and neutral current (red lines) interaction lengths for neutrino (solid lines) and antineutrino (dashed lines) on nucleon targets, computed with the CTEQ6-DIS parton distributions [96]. The thick black solid line represents the sum of the four reactions.

Due to the smaller cross section of NC interactions, the corresponding interaction length is larger than the CC interaction one.

At the Glashow resonance, the reaction $\bar{\nu}_e e \rightarrow W^- \rightarrow X$ significantly attenuates an anti-electron neutrino beam propagating through the Earth. The water-equivalent interaction length is evaluated as

$$\mathcal{L}_{\text{int}}^{(e)} = \frac{1}{\sigma_{\bar{\nu}_e e}(E_\nu)(10/18)N_A} \quad (5.12)$$

where $(10/18)N_A$ is the number of electrons in a mole of water.

To good approximation, the Earth may be regarded as a spherically symmetric ball with a complex internal structure consisting of a dense inner and outer core and a lower mantle of medium density, covered by a transition zone, lid, crust and oceans [99]. A convenient representation of the density profile of the Earth is given by the Preliminary Earth Model [100], plotted in Figure 5.7.

The Earth's diameter exceeds the total interaction length of neutrinos with energy higher than about 10 TeV (Figure 5.8). Thus, neutrinos with higher energies preferentially enter the detector at larger zenith angles. In the interval $2 \times 10^6 \text{ GeV} \leq E_\nu \leq 2 \times 10^7 \text{ GeV}$, resonant $\bar{\nu}_e e$ scattering adds dramatically to the attenuation of anti-electron neutrinos. At resonance, the interaction length due to the reaction $\bar{\nu}_e e \rightarrow W^- \rightarrow X$ is 60 km w.e. There-

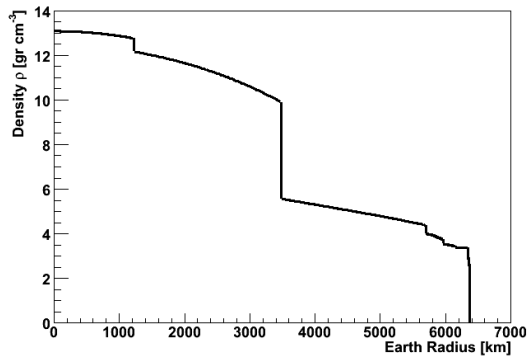


Figure 5.7: Density profile of the Earth according to the Preliminary Earth Model [100].

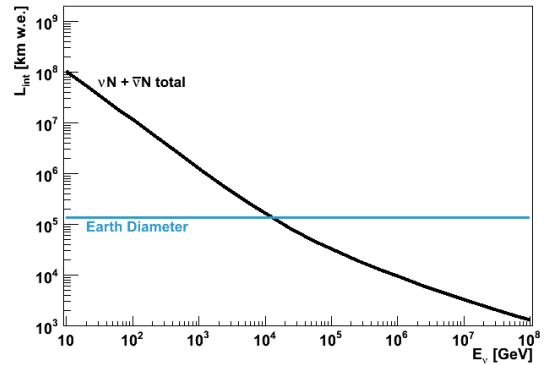


Figure 5.8: Total interaction lengths for (anti)neutrino-nucleon interactions. The diameter of the Earth, according to the parameterization in Figure 5.7, is also shown.

fore, the resonance is effectively extinguished for anti-electron neutrinos that traverse the Earth.

Chapter 6

Diffuse Neutrino Flux Analysis

To study the sensitivity of the ANTARES detector to a diffuse flux of high energy neutrinos which produce showers in the detector, specific selection criteria have to be defined in order to discard the background signal. The background signal is represented by atmospheric muons and neutrinos, while the signal comprises cosmic neutrinos.

Specific Monte Carlo samples have been generated to simulate the background and the signal, which are described in § 6.1. The selection criteria for reconstructed events to reject the background signal are discussed in § 6.2. These criteria do not discriminate upward going from downward going events, leaving the signal isotropically distributed over 4π . After the selection criteria have been applied to the Monte Carlo data samples, a comparison between atmospheric muons and a sample of real data has been performed (§ 6.3). To conclude, § 6.4 presents efficiencies and purities of the selected signal events.

6.1 Monte Carlo Samples

This section describes the different Monte Carlo data samples that have been generated to perform the study of the diffuse flux of high energy neutrinos. The atmospheric muons as well as the atmospheric and cosmic neutrinos have been specifically produced for this analysis. Regarding the atmospheric muon neutrinos, the official Monte Carlo production as used within the ANTARES Collaboration has been applied.

To simulate the optical background due to ^{40}K decay and bioluminescence (§ 2.6), data run 38712 acquired on November 18th 2008 has been applied to the simulation of the trigger algorithm (§ A.3). For this run, the baseline rate is 63 kHz and the burst fraction is 17%.

6.1.1 Atmospheric Muons

A dedicated simulation of atmospheric muons has been performed for this analysis, which subsequently became an official production available within the ANTARES Collaboration.

The atmospheric muon flux is about six orders of magnitude larger than the atmospheric neutrino flux (Figure 3.1) and represents the most abundant signal seen by a neutrino telescope. Although the computing time required by MUPAGE (Chapter 4) is very small with respect to a full Monte Carlo simulation of atmospheric muons, the subsequent steps in the Monte Carlo analysis chain (Appendix A), such as the Cherenkov light production and the detector response, are very time consuming¹.

A study which compares the muon bundle energy with the number of reconstructed hits has shown that, if the number of reconstructed hits is greater than 60 (minimum number of reconstructed hits in an event of cosmic muon or electron neutrinos), the energy of an atmospheric muon bundle is greater than a few TeV. Therefore, the atmospheric muon flux has been generated with an energy threshold of 1 TeV and an equivalent livetime of 1 year. The energy threshold is the minimum energy of all muons in the bundle. Hence, if the bundle comprises a single muon, this muon will have an energy of at least 1 TeV. On the other hand, if the bundle comprises multiple muons, the sum of all the muon energies will be larger than at least 1 TeV.

In order to save further computing time, the generation have been divided in 6 ranges of muon multiplicity. Table 6.1 reports the number of generated events for each muon multiplicity range as well as the number of events surviving after the application of the trigger criteria (§ A.3) and of the event reconstruction, using the BBFit reconstruction algorithm described in § A.4. After the reconstruction, the six muon multiplicity samples have been summed in a unique sample (**Total** in Table 6.1).

6.1.2 Atmospheric CC Muon Neutrinos

For the Monte Carlo sample of charged current atmospheric muon neutrinos, the official production available within the ANTARES Collaboration has been used. This production takes into account the conventional atmospheric neutrino flux (Bartol [57], § 5.1) and it has been generated with an energy spectrum proportional to $E^{-1.4}$ in order to increase the statistics. The `genhen` program (§ A.1.2) assigns for each generated event 3 weights,

¹The computing time required to produce the other official MUPAGE production available within the ANTARES Collaboration (described in § 4.6), which corresponds to an equivalent livetime of 30 days, was 11 days for the MUPAGE generation and 488 days for the Cherenkov light production and the detector response (on a 2.33 GHz computer, using Scientific Linux 4).

Range of Muon Multiplicity	Generated	Triggered	Reconstructed
1	7.08×10^8	2.79×10^7 (4%)	2.21×10^7 (3%)
2	4.34×10^8	2.67×10^7 (6%)	2.23×10^7 (5%)
3	2.45×10^8	1.93×10^7 (8%)	1.67×10^7 (7%)
4 – 10	3.88×10^8	4.18×10^7 (11%)	3.80×10^7 (10%)
11 – 100	5.40×10^7	8.88×10^6 (16%)	8.41×10^7 (16%)
101 – 1000	5.50×10^5	1.49×10^5 (27%)	1.43×10^7 (26%)
Total	1.83×10^9	1.25×10^8 (7%)	1.08×10^8 (6%)

Table 6.1: Number of events in the atmospheric muon samples, in order to simulate an equivalent livetime of 1 year, after generation, trigger selection and reconstruction. The given percentages refer to the number of generated events (first column).

which are described in detail in § A.1.2. Using the weight $\mathbf{w3}$, it is possible to reobtain the flux that was used in the generation with its appropriate energy spectrum which is proportional to $E^{-3.6}$. Furthermore, it is also possible to re-weight the events adding the prompt (e.g. RQPM [90]) flux to the conventional flux.

The (anti)neutrino Monte Carlo data samples have been generated isotropically over 4π with an energy range between 10 and 10^7 GeV. In order to save computing time, the production has been divided in 4 groups: upward going neutrino and antineutrino, and downward going neutrino and antineutrino.

Table 6.2 reports the number of generated events for each sample as well as the number of events surviving after the application of the trigger criteria (§ A.3) and the reconstruction, using the BBFit reconstruction algorithm described in § A.4.

Figure 6.1 shows the energy distribution of the four categories of atmospheric CC muon neutrinos, after weighting the events according to the atmospheric conventional and prompt flux. The flux of reconstructed antineutrinos (dashed lines) is smaller than for

Particle	Generated	Triggered	Reconstructed
up-going ν_μ	9.0×10^{11}	1.05×10^6 (1×10^{-6})	9.60×10^5 (1×10^{-6})
up-going $\bar{\nu}_\mu$	4.0×10^{11}	4.90×10^5 (1×10^{-6})	4.46×10^5 (1×10^{-6})
down-going ν_μ	9.0×10^{11}	4.17×10^6 (5×10^{-6})	3.63×10^6 (4×10^{-6})
down-going $\bar{\nu}_\mu$	8.9×10^{11}	4.43×10^6 (5×10^{-6})	3.86×10^6 (4×10^{-6})
Total	3.1×10^{12}	1.01×10^7 (3×10^{-6})	8.89×10^6 (3×10^{-6})

Table 6.2: Number of events in the atmospheric CC muon neutrino samples, after generation, trigger selection and reconstruction. The given percentages refer to the number of generated events (first column).

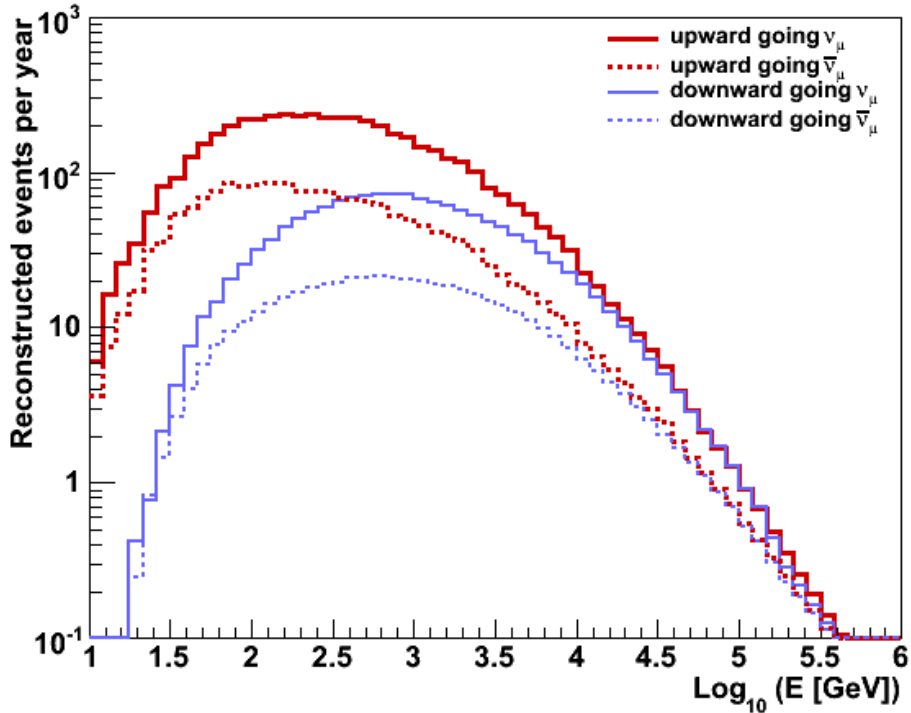


Figure 6.1: Energy distribution of atmospheric CC muon neutrinos. The thick red lines represent upward going neutrinos, while the thin blue lines represent downward going neutrinos.

neutrinos (solid lines), because they have a smaller interaction cross section (§ 5.4). The flux of reconstructed downward going (anti)neutrinos (thin blue lines) at low energies is smaller than for upward going (anti)neutrinos (thick red lines), due to the PMT orientation in the ANTARES detector (§ 2.2). The PMTs look downwards with an inclination of 45° with respect to the vertical, as shown in Figure 2.4. At energies larger than roughly 40 TeV, when the Earth starts to be opaque for neutrinos (§ 5.5), the downward going and the upward going neutrinos give almost the same contribution.

6.1.3 CC Electron Neutrinos

A dedicated production of charged current electron neutrinos has been generated taking into account the conventional (Bartol [57]) and the prompt (RQPM [90]) flux (§ 5.1). In order to increase the statistics at high energies, it has been generated with energy spectrum proportional to $E^{-1.4}$. As already mentioned, the use of the weight $\mathbf{w3}$ calculated by the `genhen` program and described in § A.1.2, gives back the selected flux of atmospheric neutrinos with its corresponding energy spectrum proportional to $E^{-3.6}$. Furthermore, to simulate a cosmic neutrino flux, e.g. according to Waxman-Bahcall (§ 5.2), the generated

events must simply be weighted with

$$\mathbf{w2} \cdot (E^{-2} \cdot 4.5 \times 10^{-8}) \text{ GeV cm}^{-2} \text{ s}^{-1} \text{ sr}^{-1}$$

Hence, the same Monte Carlo data sample can be used to reproduce either the background due to atmospheric electron neutrinos or the signal of cosmic electron neutrinos.

The (anti)neutrino Monte Carlo data samples have been generated with energy range between 10^4 and 10^8 GeV and are isotropic over 4π . Since the computing time of the *geasim* program (which produces the Cherenkov light and simulates the detector response) increases at increasing neutrino energies, as described in § A.2.2, the generation has been divided in 4 ranges of energy: $10^4 - 10^5$ GeV, $10^5 - 10^6$ GeV, $10^6 - 10^7$ GeV and $10^7 - 10^8$ GeV. Separate samples for upward going neutrino and antineutrino, and downward going neutrino and antineutrino have been generated, in order to not introduce biases when the events are weighted afterwards.

Table 6.3 reports the number of generated events for each sample as well as the number of events surviving after the application of the trigger criteria (§ A.3) and the reconstruction, using the BBFit reconstruction algorithm (§ A.4).

Figure 6.2 shows the energy distribution of the four categories of atmospheric CC electron neutrinos, after each event has been weighted according to the atmospheric energy spectrum. The peak around 6.3 PeV for antineutrinos (dashed lines) is the so-called Glashow resonance, described in § 5.4. The contribution of downward going neutrinos (thin blue lines) is larger than the contribution of upward going neutrinos (thick red lines) because of the Earth's opacity at this energy range (§ 5.5). Note that antineutrinos at the energy of the Glashow resonance should not be able to traverse the Earth, since at those energies their interaction length is 60 km w.e. However, as can be seen from Figure 6.2, they are present in the Monte Carlo simulation. These unphysical neutrinos are caused

Particle	Generated	Triggered	Reconstructed
up-going ν_e	2.14×10^5	1.50×10^5 (70%)	1.49×10^5 (70%)
up-going $\bar{\nu}_e$	1.98×10^5	1.36×10^5 (69%)	1.34×10^5 (68%)
down-going ν_e	2.20×10^5	1.48×10^5 (67%)	1.46×10^5 (66%)
down-going $\bar{\nu}_e$	2.03×10^5	1.35×10^5 (67%)	1.33×10^5 (66%)
Total	8.36×10^5	5.69×10^5 (68%)	5.62×10^5 (67%)

Table 6.3: Number of events in the CC electron neutrino samples, after generation, trigger selection and reconstruction. The given percentages refer to the number of surviving events with respect to the number of generated events (first column).

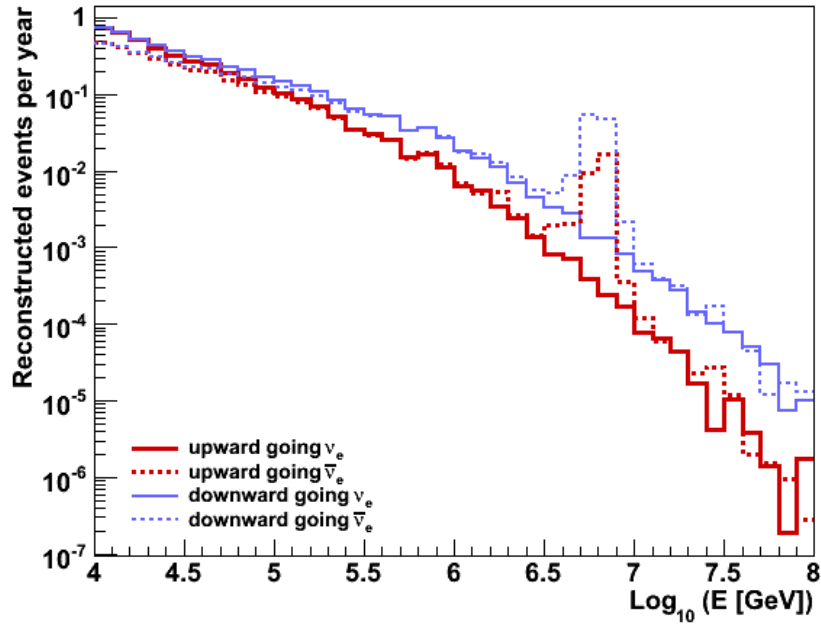


Figure 6.2: Energy distribution of reconstructed atmospheric CC (anti-)electron neutrinos. The thick red lines represent upward going, while the thin blue lines represent downward going (anti)neutrinos. The peak around 6.3 PeV for antineutrinos (dashed lines) is the so-called Glashow resonance, described in § 5.4.

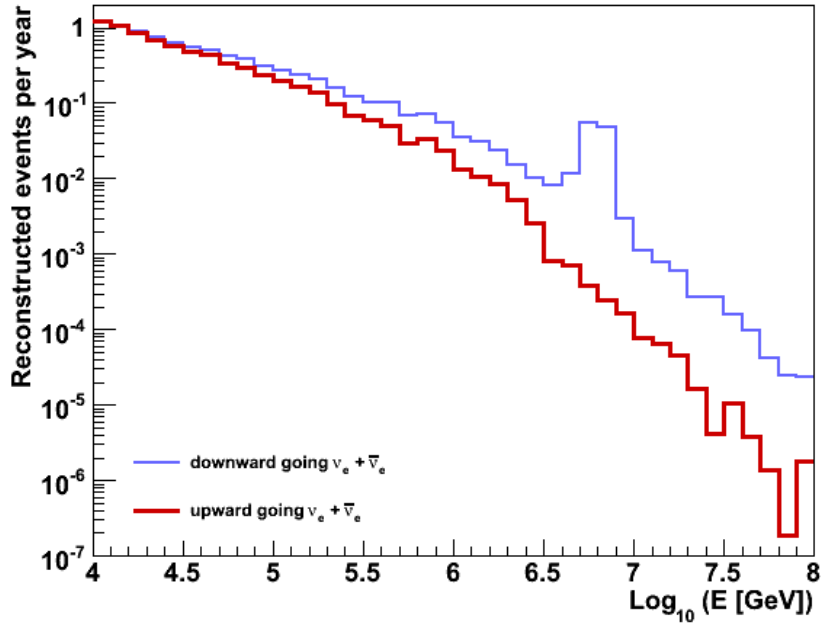


Figure 6.3: Energy distribution of reconstructed atmospheric CC (anti-)electron neutrinos, after the exclusion of wrongly generated upward going anti-electron neutrinos (see text for details). The thick red lines represent upward going neutrinos and antineutrinos, while the thin blue lines represent downward going neutrinos and antineutrinos.

by an error in the computation of the Earth's absorption of anti-electron neutrinos. Since before the deadline of this thesis it was not possible to redo the simulation, upward going anti-electron neutrinos with energies larger than 3×10^6 GeV have been excluded. Furthermore, even if downward going anti-electron neutrinos around the Glashow resonance could be a little bit overestimated, this possible effect is not taken into account. Figure 6.3 shows the energy distribution of upward going (red thick line) and downward going (thin blue line) atmospheric (anti-)electron neutrinos after the exclusion of upward going anti-electron neutrinos with energies larger than 3 PeV.

6.1.4 NC Neutrinos

Although a dedicated production of neutral current neutrinos has been generated, unexpected behavior has been noticed in the sample which will require further investigations. Hence, the contribution of the NC interactions have been excluded from the following analysis.

6.2 Rejection of the Background Signal

The background signal to cosmic high energy neutrinos identified by showers is mainly due to the atmospheric muons and to atmospheric neutrinos.

In this section, a novel technique to identify the signal from the background is developed. It is based on the application of a number of selection criteria on different variables with respect to the reconstructed events in the Monte Carlo data samples described in the previous section (§ 6.1).

Since the events are reconstructed with BBFit algorithm (§ A.4), two categories of events have to be discarded from the following analysis: events with less than 5 hits and events with $\cos \theta = \pm 1$. The first exclusion is due to the fact that no fit is attempted for events which have less than 5 hits. The second one is due to the fact that the reconstruction algorithm does not always converge towards a definite set of values for all fitting parameters. In this case the program sets the value of the reconstructed zenith angle cosine ($\cos \theta$) equal to 1 or -1 .

Although most of the background signal is due to atmospheric muons which are downward going, it has been preferred to avoid a cut on the particle direction. This choice is mainly due to preserve the isotropy over 4π of the signal. This decision is motivated by the fact that at the considered neutrino energies, the amount of downward going cosmic neutrinos is larger than the number of upward going neutrinos because of the Earth's

Particle	Events per year
Atmospheric μ	9.18×10^7
Atmospheric ν_μ	8.56×10^3
Atmospheric ν_e	15.2
$E^{-2} \nu_e$	36.5

Table 6.4: Number of expected events per year at reconstruction level, before any cut, for background and for the signal given by Eq. (6.1).

opacity (§ 5.5).

Table 6.4 shows the number of expected events per year for each Monte Carlo sample. The cosmic electron neutrinos ($E^{-2} \nu_e$) have been weighted according to the flux

$$E_\nu^2 \frac{dN_\nu}{dE_\nu} = 10^{-7} \text{ GeV cm}^{-2} \text{ s}^{-1} \text{ sr}^{-1} \quad (6.1)$$

Note that this normalization is irrelevant in the definition of selection criteria, or on the computation of the ANTARES sensitivity.

6.2.1 Number of lines

The first cut that have been applied concerns the number of lines used to reconstructed an event, referred to as *nline*. Most of the atmospheric muons are reconstructed with two lines (about 77%), as shown in Figure 6.4. Hence only events with *nline* > 2 have been selected.

6.2.2 Fit Quality Parameters

A cut on the fit quality parameter Q (Eq. A.14) can be applied by taking advantage of the different topology of the events. The atmospheric muons and neutrino-induced muons are reconstructed as tracks (§ A.4.1.1), while the electromagnetic showers induced by CC electron neutrinos are reconstructed as bright points (§ A.4.1.2).

The quantity *chi2* refers to the fit quality parameter Q divided by the number of degrees of freedom. A cut on the difference between the bright point *chi2* (*bchi2*) and the track *chi2* (*tchi2*) allows the rejection of a further roughly 22% of reconstructed atmospheric muons, as shown in Figure 6.5. Hence, only events with *bchi2* - *tchi2* < 1 have been selected.

Figure 6.5 shows some peculiarities. A peak between -1 and 0 for the atmospheric CC muon neutrinos (dash-dotted line), and one peak between -25 and -22 in the cosmic electron neutrino distribution (in gray). The peak in the atmospheric CC muon neutrino distribution, shown in more detail in Figure 6.6, is due to downward going events (thin

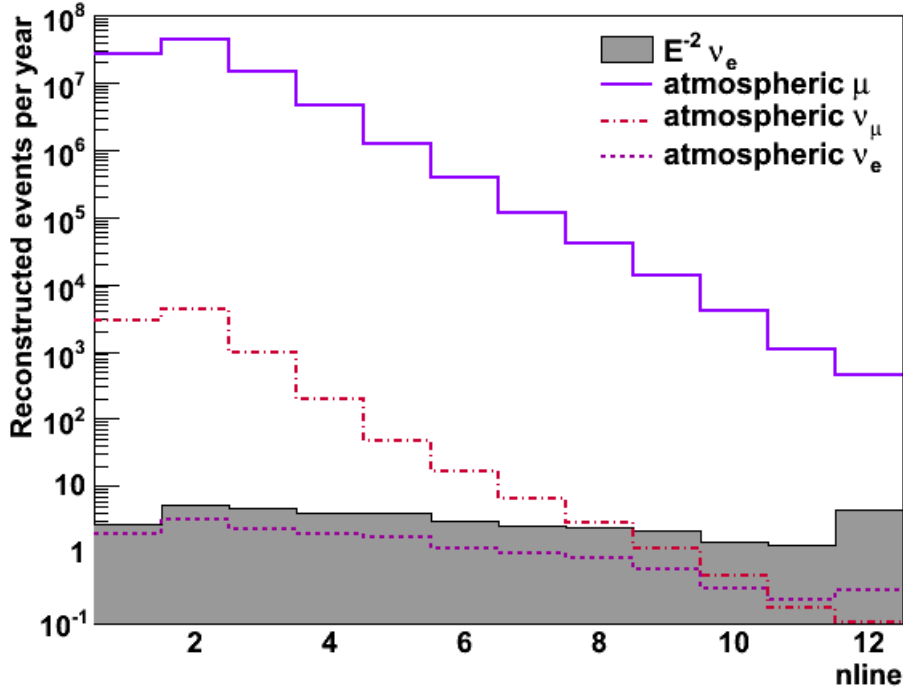


Figure 6.4: Number of reconstructed events per year as a function of the number of detector lines used in the reconstruction. The events are cosmic electron neutrinos (in gray), atmospheric muons (solid line), atmospheric CC muon neutrinos (dash-dotted line) and atmospheric CC electron neutrinos (dashed line). As can be seen, for a significant fraction of the cosmic electron neutrinos all detector lines are present.

blue line). These events, after the $nline > 2$ cut, have more probability to be reconstructed as bright points than as tracks (i.e. $bchi2 < tchi2$). This is even more accentuated at low energies (up to a few TeV). A possible explanation concerns the PMT orientation of the ANTARES detector (§ 2.2), where the PMTs look downwards with an inclination of 45° with respect the vertical (see Figure 2.4). The peak in the astrophysical CC electron neutrino distribution is due to the Glashow resonance (§ 5.4) in the downward going antineutrino distributions, as shown in more detail in Figure 6.7.

6.2.3 Amplitude

The last cut based on the total amplitude is intended to totally exclude the contribution of the atmospheric muons.

As explained in § 2.4.1, when the amplitude of a PMT signal exceeds 0.3 photoelectrons, the signal is read out and digitized by the Analogue Ring Sampler (ARS). As described in § 2.5.2, prior to deployment, a study has shown that all ARSs behave in the same way [51]. During data taking, special data runs are taken to measure the so-called

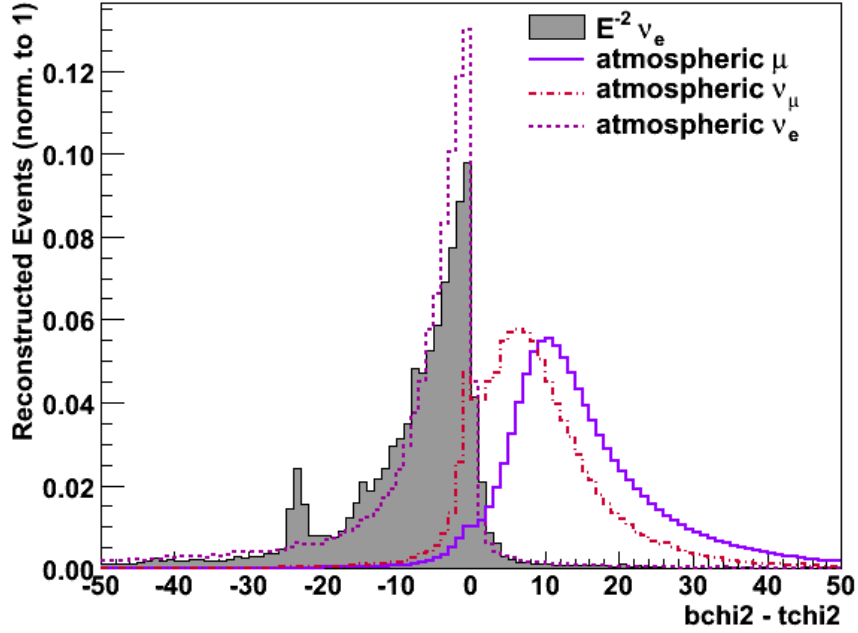


Figure 6.5: Distributions of the difference between the bright point χ^2 and the track χ^2 . The figure shows four distributions which are all normalized to unit area and which contain only events with $nline > 2$: cosmic electron neutrinos (in gray), atmospheric muons (solid line), atmospheric CC muon neutrinos (dash-dotted line) and atmospheric CC electron neutrinos (dashed line).

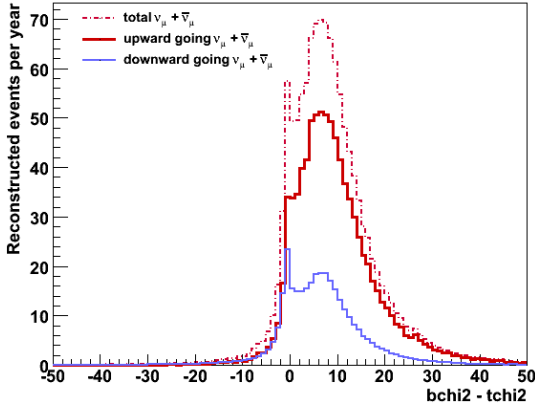


Figure 6.6: Number of reconstructed atmospheric CC muon (anti)neutrinos per year (after the $nline > 2$ cut) as function of the difference between the bright point χ^2 and the track χ^2 . The thin blue line represents the downward going events and the thick red line the upward going events; the sum of them is the dash-dotted line.

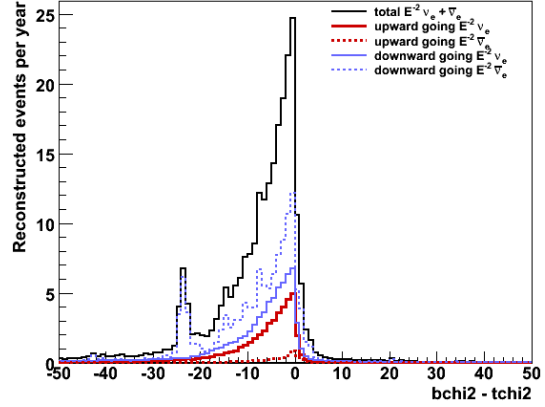


Figure 6.7: Number of reconstructed astrophysical CC electron (anti)neutrinos per year as function of $b\chi^2 - t\chi^2$. In thick red lines the upward going neutrinos and thin blue lines the downward going neutrinos. The antineutrinos are in dashed lines. The total contribution of these four categories is represented by the black line.

pedestal of the Analogue-to-Voltage Converter (AVC) as well as the position of the single photoelectron peak. These quantities are used to estimate the charge over the full dynamical range of the AVC, which is used to convert the analogue charge measurements of the PMT signals into photoelectron units.

The BBFit reconstruction algorithm approximates each storey as a space point centered on a vertical detector line. After the application of time and charge calibrations (§ 2.5), the hits in the event are time ordered and merged on each storey if closer than 20 ns. In this case, the time of the first hit is taken and the charges are summed.

The total amplitude is the sum of the amplitudes of all the hits in an event (in photoelectrons) and is referred to as *amp*. Table 6.5 shows the number of atmospheric muons per year which pass different selection criteria on the variable *amp*. With the selection criterion $amp > 2300$ p.e. no atmospheric muons survive.

Cut	Events per year
$amp > 500$ p.e.	7414
$amp > 1000$ p.e.	408
$amp > 1500$ p.e.	48
$amp > 2000$ p.e.	7
$amp > 2100$ p.e.	3
$amp > 2200$ p.e.	2
$amp > 2300$ p.e.	0

Table 6.5: Number of expected atmospheric muons per year which pass different *amp* selection criteria.

6.2.4 Summary of the Selection Criteria

Table 6.6 shows the number of surviving events per year for background and signal (last column) after each subsequent selection criterion.

Cuts	Atm. μ	Atm. CC ν_μ	Atm. CC ν_e	$E^{-2} \nu_e$
No cut	9.18×10^7	3.56×10^3	15.2	36.5
$nline > 2$	2.12×10^7	1.22×10^3	10.2	28.8
$bchi2 - tchi2 < 1$	1.06×10^6	2.05×10^2	9.70	27.0
$amp > 2300$ p.e.	0	7.51×10^{-3}	0.37	5.2

Table 6.6: Event rate per year after each subsequent selection criterion.

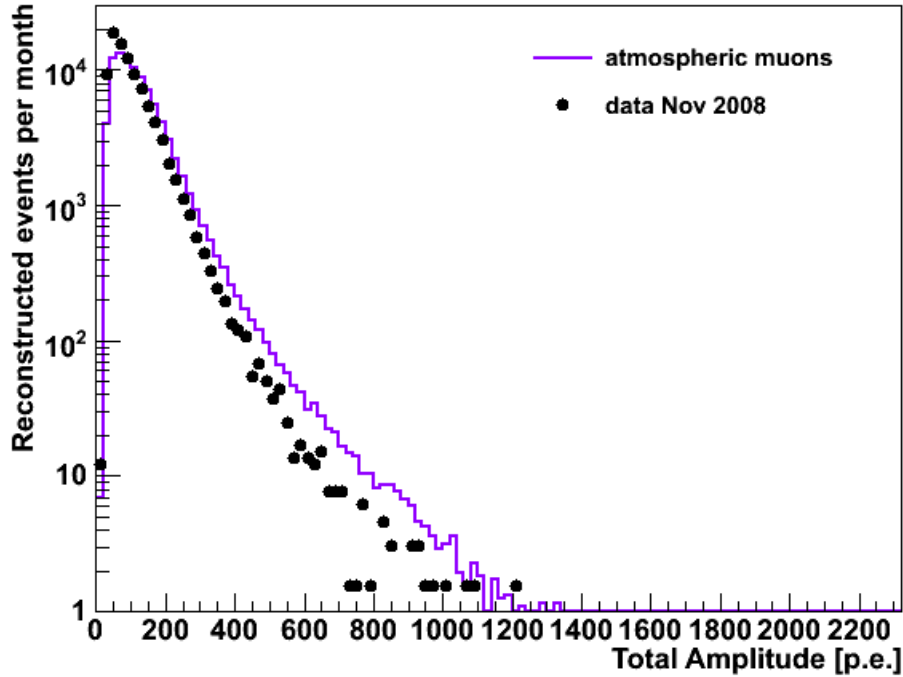


Figure 6.8: Distribution of the sum of the amplitudes of all the hits in an event: total amplitude (in photoelectron). The reconstructed events per month have passed the $nline > 2$ and the $bchi2 - tchi2 < 1$ cuts: atmospheric muons (solid line) and selected data of November 2008 (black points).

6.3 Comparison between Monte Carlo Atmospheric Muons and Data

The comparison between Monte Carlo atmospheric muons and data is only done outside the so-called *black box* region. In this region, only events that pass the first two cuts (i.e. $nline > 2$ and $bchi2 - tchi2 < 1$) are selected, while the events that pass the last cut (i.e. $amp > 2300$ p.e.) are excluded.

The data set comprises the data acquired in the month of November 2008. This choice is due to the fact that in the Monte Carlo samples the optical background has been simulated using data run 38712 acquired on November 18th 2008. The chosen data set must have on average the same detector configuration as used in the Monte Carlo simulations, such as the number of active OMs, baseline rate and burst fraction (§ 2.6). Hence, only runs fulfilling the so-called *silver* quality criteria have been selected:

- at least 700 out of 885 installed optical modules are active during a run ($\sim 80\%$);
- the baseline rate is below 120 kHz;

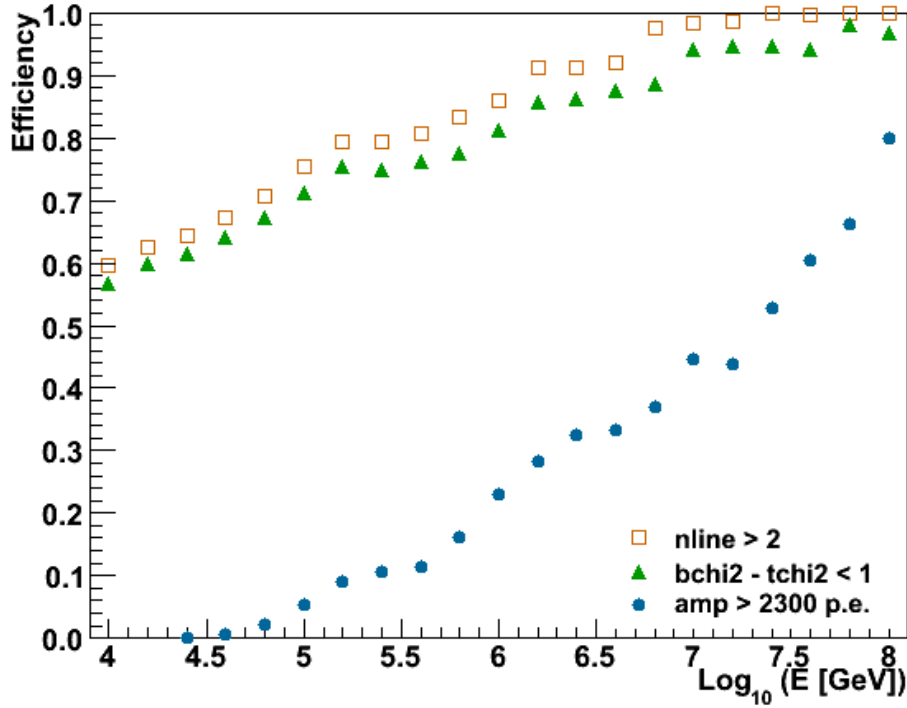


Figure 6.9: Efficiencies of the selection criteria as a function of the generated neutrino energy.

- the burst fraction is less than 40%.

The 258 selected data runs¹ correspond to an active detector time of about 20 effective days.

Figure 6.8 shows a comparison between the total amplitude distributions of Monte Carlo atmospheric muons and data after the $nline > 2$ and $bchi2 - tchi2 < 1$ selection criteria. The Monte Carlo atmospheric muon simulation seems to overestimate the total amplitude of the signal. Hence setting a selection criterion at $amp > 2300$ p.e. can be considered as a conservative choice.

6.4 Efficiencies and Purities of the Selection Criteria

The selection efficiency is defined as the fraction of reconstructed signal events, i.e. astrophysical electron neutrinos, which pass a selection criterion:

$$\text{Efficiency} = \frac{N_{cut}^{signal}}{N^{signal}} \quad (6.2)$$

Figure 6.9 shows the efficiencies of each subsequent selection criterion as a function of the generated neutrino energy.

¹Silver runs from data run 36850 to data run 37470.

The selection purity is defined as the fraction of reconstructed signal events which pass a selection criterion over the total number (signal and background) of reconstructed events which pass the same selection criterion:

$$\text{Purity} = \frac{N_{cut}^{signal}}{N_{cut}^{signal} + N_{cut}^{background}} \quad (6.3)$$

Efficiencies and purities for cosmic electron neutrinos ($E^{-2} \nu_e$), after each subsequent selection criterion, are shown in Table 6.7.

Cuts	$E^{-2} \nu_e$	
	Efficiency	Purity
$nline > 2$	0.79	1.4×10^{-6}
$bchi2 - tchi2 < 1$	0.74	2.5×10^{-5}
$amp > 2300$ p.e.	0.14	0.93

Table 6.7: Cumulative efficiencies and purities of the signal events after each selection criterion applied in this analysis.

Chapter 7

Sensitivity to the Diffuse Neutrino Flux through Electromagnetic Showers

After the identification of suitable selection criteria which reject most of the background signal described in Chapter 6, the sensitivity of the ANTARES detector to the diffuse flux of high energy electron neutrinos which induce electromagnetic showers is estimated in § 7.1 for a detector livetime of 1 year. Some considerations regarding the ANTARES running configurations from December 7th 2007 until December 31st 2009 are discussed in § 7.2. Therefore, the Monte Carlo electron neutrino samples are adapted to reproduce the real detector setups (§ 7.3). In § 7.4, the realistic ANTARES sensitivity for 335 active days is calculated and subsequently compared to other experiments. Finally, § 7.5 discusses the outlook of this analysis.

7.1 Diffuse Neutrino Flux Sensitivity

With the selection criteria applied in the previous chapter, the background signal due to atmospheric muons has been totally eliminated. Furthermore, the background signal due to atmospheric CC muon neutrinos can also be neglected since it is three order of magnitude smaller than the signal, as shown in Table 6.6. The only background signal which survives the cuts is due to atmospheric CC electron neutrinos with an expected rate n_b of 0.37 events per year. For the signal, due to astrophysical CC electron neutrinos, a hypothetical flux of $E_\nu^2 \Phi = 10^{-7} \text{ GeV cm}^{-2} \text{ s}^{-1} \text{ sr}^{-1}$ was assumed, leading to an expected rate n_s of 5.2 events per year.

The sensitivity is defined as the average upper limit on the diffuse flux of neutrinos that would be obtained by an ensemble of experiments with the expected background and

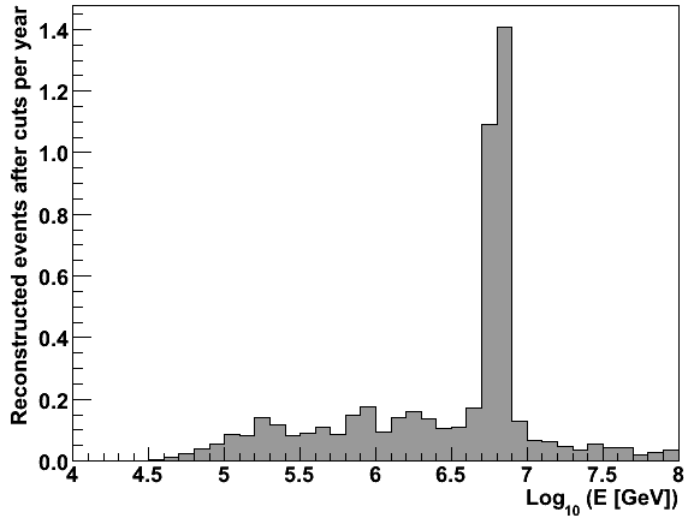


Figure 7.1: Energy spectra of cosmic (anti-)electron neutrino events, $E^{-2}(\nu_e + \bar{\nu}_e)$, that pass all the selection criteria. The peak between $10^{6.7}$ and $10^{6.9}$ GeV is due to the Glashow resonance for downward going anti-electron neutrinos.

no true signal. The average upper limit is the sum of the expected upper limits at 90% confidence level in the Feldman-Cousins unified approach [101], weighted by their Poisson probability of occurrence

$$\bar{\mu}_{90}(n_b) \equiv \sum_{n_{obs}=0}^{\infty} \mu_{90}(n_{obs}, n_b) \frac{(n_b)^{n_{obs}}}{(n_{obs})!} e^{-n_b} \quad (7.1)$$

where n_b is the expected number of background events and n_{obs} is the number of observed events. Over an ensemble of identical experiments, the upper limit on the expected signal flux $\Phi(E)$ corresponds to the set of selection criteria that minimizes the so-called model rejection factor $\bar{\mu}_{90}/n_s$ [102], and hence minimizes the average flux upper limit that would be obtained over the hypothetical experimental ensemble

$$\bar{\Phi}(E)_{90} \equiv \Phi(E) \frac{\bar{\mu}_{90}}{n_s} \quad (7.2)$$

In this analysis, the expected background n_b is the event rate of the atmospheric CC electron neutrino flux, which corresponds to 0.37 events per year. Therefore, the average upper limit is $\bar{\mu}_{90}(0.37) = 2.75$. Since n_s is equal to 5.2 events per year and the flux $E_\nu^2 \Phi(E) = 10^{-7} \text{ GeV cm}^{-2} \text{ s}^{-1} \text{ sr}^{-1}$, the diffuse electron neutrino flux sensitivity is

$$E_\nu^2 \Phi_{90\%CL} = 5.3 \times 10^{-8} \text{ GeV cm}^{-2} \text{ s}^{-1} \text{ sr}^{-1} \quad (7.3)$$

with the central 90% of the E^{-2} signal found between the energies of $10^{5.2}$ and $10^{7.2}$ GeV, as shown in Figure 7.1.

7.2 The Real Detector

The sensitivity to the diffuse flux of high energy neutrinos calculated in Eq. (7.3) refers to the ANTARES detector livetime of 1 year, with all the 12 lines and with an average of 712 active OMs out of 885. The number of active OMs is taken from data run 37218, which is used in the simulation of the trigger algorithm used to process the Monte Carlo data samples described in § 6.1. However, the real detector has different configurations which change run by run.

From December 7th 2007, when Lines 6 – 10 were connected, until December 31st 2009 the detector has acquired data in different setups (Table 2.2) with 10 active lines, 9 active lines and 12 active lines. To estimate the percentage of effective days for each configuration, only runs which fulfill the so-called *silver* quality criteria have been selected:

- at least 80% of working optical modules are active during a run;
- the baseline rate (§ 2.6) is below 120 kHz;
- the burst fraction (§ 2.6) is less than 40%.

To satisfy the first condition, the minimum number of active OMs for the 9Line configuration is 500, for the 10Line configuration is 571, while for the 12Line is 700. Figure 7.2 shows the distributions of the number of active OMs in the 3081 selected runs¹. These runs correspond to an active detector time of about 335 effective days.

The range of active OMs, the number of selected runs and the equivalent number of effective days are reported in Table 7.1 for each configuration.

Detector Setup	Active OMs	Number of Runs	Effective Days
9Line	500 – 570	945	136.1 (40.6%)
10Line	571 – 700	1167	128.4 (38.4%)
12Line	700 – 885	969	70.0 (21.0%)

Table 7.1: Range of active OMs, number of selected runs, equivalent number of effective days and percentage with respect to the total 335 days for each detector configuration.

To estimate a more realistic diffuse neutrino flux sensitivity, the Monte Carlo data samples can be processed to reproduce these 3 detector setups and then summed together taking into account the different livetimes.

¹Silver runs from data run 30508 to data run 45536.

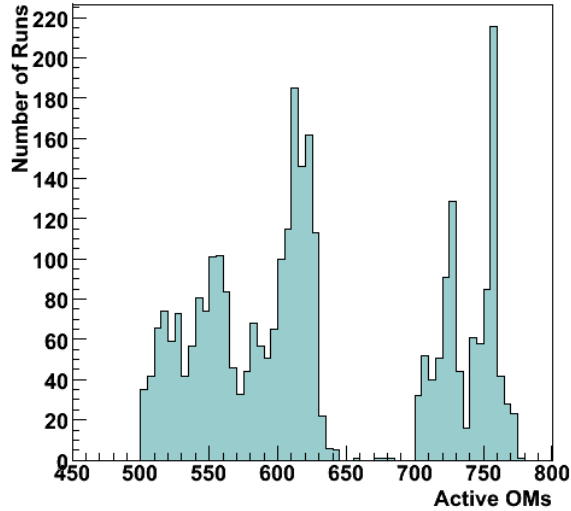


Figure 7.2: Distribution of the number of active optical modules in the 3081 considered runs.

7.3 Monte Carlo Samples for Different ANTARES Setups

Since the background signal due to atmospheric muons and atmospheric muon neutrinos has been already rejected with the selection criteria described in § 6.2 and optimized for the 12Line configuration, there is no need to reprocess them for the other two ANTARES configurations. Using the same selection criteria defined with the 12Line setup on a detector with a smaller number of OMs (9 and 10Line), the rejection of the background is even more conservative. Therefore, only the CC electron neutrino sample (§ 6.1.3) has to be reprocessed in order to take into account the new detector configurations.

7.3.1 9Line Configuration

To simulate an average of 540 active OMs, the `geasim` output files of the Monte Carlo CC electron neutrino samples (§ 6.1.3) have been processed in the simulation of the trigger algorithm (§ A.3) using data run 33341 acquired on April 3rd 2008 to simulate the optical background (§ 2.6). For this run, the baseline rate is 55 kHz and the burst fraction is 16%.

For the 9Line setup, the number of generated events for each Monte Carlo sample, the number of events surviving after the application of the trigger criteria and the number of reconstructed events are summarized in Table 7.2. As usual, the BBFit reconstruction algorithm as described in § A.4 was used. This table is equivalent to Table 6.3 for the 12Line configuration.

Particle	Generated	Triggered	Reconstructed
up-going ν_e	2.14×10^5	1.45×10^5 (68%)	1.43×10^5 (67%)
up-going $\bar{\nu}_e$	1.98×10^5	1.42×10^5 (66%)	1.40×10^5 (65%)
down-going ν_e	2.20×10^5	1.31×10^5 (65%)	1.28×10^5 (64%)
down-going $\bar{\nu}_e$	2.03×10^5	1.30×10^5 (64%)	1.25×10^5 (63%)
Total	8.36×10^5	5.49×10^5 (66%)	5.38×10^5 (64%)

Table 7.2: Number of events in the CC electron neutrino samples, after generation, trigger selection for the 9Line configuration and reconstruction. The given percentages refer to the number of surviving events with respect to the number of generated events (first column).

7.3.2 10Line Configuration

To simulate an average of 604 active OMs, the same *geasim* output files of the Monte Carlo CC electron neutrino samples have been processed in the simulation of the trigger algorithm (§ A.3) using data run 32185 acquired on February 2nd 2008 to simulate the optical background (§ 2.6). For this run, the baseline rate is 55 kHz and the burst fraction is 15%.

For the 10Line setup, the number of generated events for each Monte Carlo sample, the number of events surviving after the application of the trigger criteria and the number of the reconstructed events with BBFit algorithm are summarized in Table 7.3. It has to be noted that the trigger criteria adopted during data acquisition with the 10Line configuration are slightly different than the ones used for the other two setups. The so-called T3 trigger (§ A.3) has been activated in the online trigger algorithm since March 2008, while the run used to simulate the detector status (and the optical background) is taken from the previous month. However, even if in the Monte Carlo samples this trigger is not active, this should have no effect on this analysis because the majority of the signal induces hits in all the detector lines and will be totally collected by the 3N trigger. Only for relatively low energy events this is not the case. Hence, the Monte Carlo samples are adequate also for the subsequent periods of the 10Line configuration in which the T3 trigger was operating.

7.4 Diffuse Neutrino Flux Analysis for Different Setups

The selection criteria defined for the 12Line configuration (§ 6.2) are applied to these new Monte Carlo samples of CC electron neutrinos. It has to be remarked that upward going anti-electron neutrinos with energies higher than 3 PeV are excluded because the

Particle	Generated	Triggered	Reconstructed
up-going ν_e	2.14×10^5	1.41×10^5 (66%)	1.40×10^5 (66%)
up-going $\bar{\nu}_e$	1.98×10^5	1.39×10^5 (64%)	1.38×10^5 (63%)
down-going ν_e	2.20×10^5	1.27×10^5 (63%)	1.26×10^5 (63%)
down-going $\bar{\nu}_e$	2.03×10^5	1.26×10^5 (62%)	1.25×10^5 (61%)
Total	8.36×10^5	5.33×10^5 (64%)	5.29×10^5 (63%)

Table 7.3: Number of events in the CC electron neutrino samples, after generation, trigger selection for the 10Line configuration and reconstruction. The given percentages refer to the number of surviving events with respect to the number of generated events (first column).

Glashow resonance was not included in the Earth's absorption probability. The hypothetical flux of the signal, due to astrophysical CC electron neutrinos, is assumed again as $E_\nu^2 \Phi = 10^{-7} \text{ GeV cm}^{-2} \text{ s}^{-1} \text{ sr}^{-1}$.

Table 7.4 shows the number of reconstructed atmospheric and cosmic electron neutrino events per year for the 3 ANTARES configurations (namely 9Line, 10Line and 12Line) before any selection criterion and after all the selection criteria. The cumulative efficiencies for the signal (Eq. 6.2) are 11% for the 9Line setup, 14% for the 10Line and the 12Line setups. The cumulative purities (Eq. 6.3) are 95% for the 9Line setup, 94% for the 10Line and 93% for the 12Line setup.

The three Monte Carlo samples are then summed, taking into account that ANTARES has collected data for 136.1 active days in the 9Line configuration, for 128.4 active days in the 10Line configuration and for 70.0 active days in the 12Line configuration, with the specifications summarized in Table 7.1.

The expected number of background events n_b due to atmospheric CC electron neutrino flux corresponds to 0.27 events per year, with an average upper limit $\bar{\mu}_{90}(0.27) = 2.67$. Assuming as usual a hypothetical cosmic neutrino flux of $E_\nu^2 \Phi = 10^{-7} \text{ GeV cm}^{-2} \text{ s}^{-1} \text{ sr}^{-1}$, the expected signal n_s is equal to 4.4 events per year. Therefore, the sensitivity to the

Cuts	9Line setup		10Line setup		12Line setup	
	Atm. CC ν_e	$E^{-2} \nu_e$	Atm. CC ν_e	$E^{-2} \nu_e$	Atm. CC ν_e	$E^{-2} \nu_e$
No cut	13.6	33.9	13.2	33.3	15.2	36.5
All cuts	0.19	3.8	0.29	4.5	0.37	5.2

Table 7.4: Event rate per year of reconstructed events (i.e. atmospheric and cosmic CC electron neutrinos) for 9Line, 10Line and 12Line configurations before any selection criterion and after all the selection criteria.

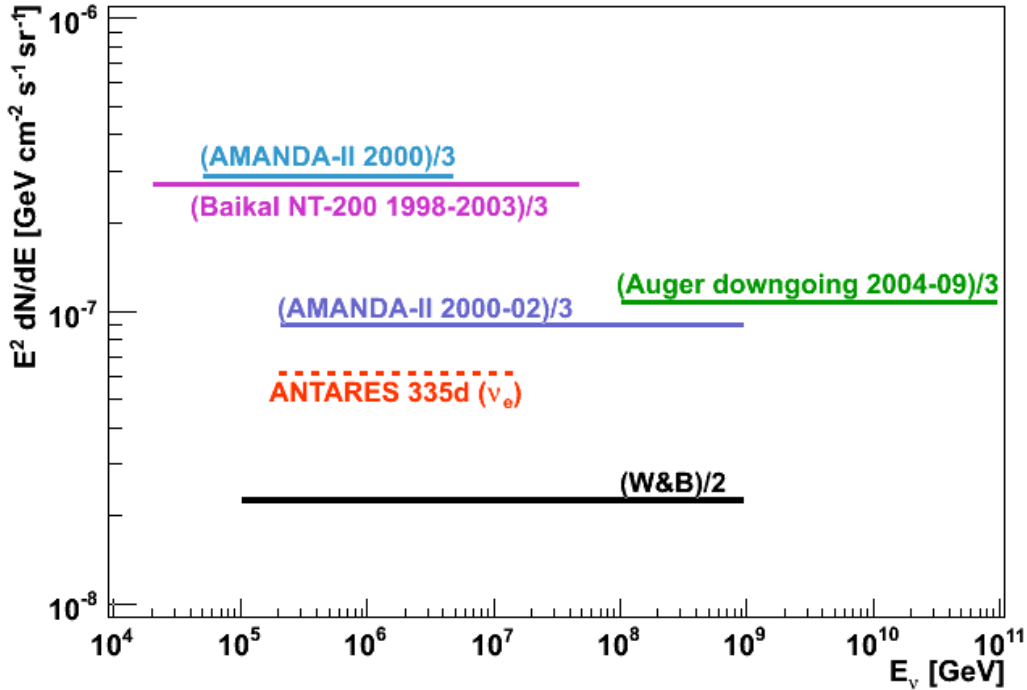


Figure 7.3: Diffuse flux sensitivity at 90% confidence level to isotropic electromagnetic shower events in 335 active days of the ANTARES detector (dash-dotted line) as determined in this analysis, in comparison with the predicted Waxman-Bahcall upper bound [29] (thick solid line) and with experimental upper limits (thin solid lines): AMANDA-II [103, 104], Baikal [105] and Auger [106]. The fractions of these limits are explained in the text.

diffuse flux of high energy neutrinos and antineutrinos through electromagnetic showers in 335 days of livetime of the ANTARES detector is

$$E_\nu^2 \Phi_{90\%CL} = 6.1 \times 10^{-8} \text{ GeV cm}^{-2} \text{ s}^{-1} \text{ sr}^{-1} \quad (7.4)$$

with the central 90% of the E^{-2} signal found between the energies of $10^{5.3}$ and $10^{7.2}$ GeV. The energy spectra of cosmic electron neutrino events that pass all the selection criteria is similar to Figure 7.1.

Figure 7.3 shows the diffuse flux sensitivity computed in Eq. (7.4) in comparison with the theoretical Waxman-Bahcall (W&B) upper limit (§ 5.2). The original value of this bound (Eq. 5.1) is calculated for a flux of muon neutrinos but can be transformed into a bound on the flux of electron neutrinos because of neutrino oscillation effects between the source and the Earth (§ 5.3). The neutrino flavor ratio observed at Earth is $\nu_e : \nu_\mu : \nu_\tau = 1 : 1 : 1$ (Eq. 5.8). Therefore, the W&B upper limit has to be divided by two. Similarly, the experimental results, which are derived with respect to all three neutrino flavors, are divided by three and compared to the single-flavor result obtained in

this thesis. The AMANDA-II neutrino telescope in Antarctica ice reported two upper limits: the first one (AMANDA-II 2000 [103]) refers to a period of 197 active days between February and November 2000; the second one (AMANDA-II 2000-02 [104]) refers to a period of roughly 459 active days between February 2000 and November 2002. The diffuse all-flavor neutrino flux of the Baikal underwater Cherenkov detector NT200 [105] has been derived using data collected in 1038 active days between April 1998 and February 2003. The array of water-Cherenkov detectors of the Pierre Auger Observatory has also placed a limit on the diffuse all-flavor neutrino flux [106] using data collected from January 2004 and February 2009. It has to be noticed that the Auger limit has been calculated only taking into account downward going neutrinos.

The result of Eq. (7.4) is a factor of about 1.5 lower than the upper limit placed by AMANDA-II [104] for 456.8 days of livetime. The sensitivity for a single-flavor flux given by AMANDA-II for the same livetime period is of $6.0 \times 10^{-8} \text{ GeV cm}^{-2} \text{ s}^{-1} \text{ sr}^{-1}$, assuming a mean of 0.43 background events and a data expectation of 0.33 event. The two results are of same order of magnitude as expected due the similarity of the instrumented volume sizes. AMANDA-II analysis concentrated on ultra high energy neutrino events at the horizon, while in this analysis all directions are considered.

7.5 Conclusion and Outlook

In this thesis, a novel technique to identify shower-like events from track-like events has been developed. Using suitable selection criteria, a sensitivity to the diffuse flux of high energy neutrino events which induce showers in the ANTARES detector has been calculated. This sensitivity is lower than the upper limit placed by other experiments, in particular AMANDA-II which has a size comparable with the ANTARES one, because no cut on the direction of the incoming particles has been made, but isotropic electromagnetic shower events are considered.

In the future, this technique will be applied also to the Monte Carlo samples of (anti)neutrinos interacting via neutral current (NC) reactions. The selection criteria optimized for the charge current (CC) electron neutrinos should be valid also for NC interactions because of the similar behavior of hadronic and electromagnetic showers in the ANTARES detector. The NC interactions will increase the number of signal as well as background events by a relative small fraction. Indeed, for NC anti-electron neutrinos there is no Glashow resonance; the cross sections for NC reactions for the considered energy ranges are roughly 40% smaller than the cross sections for CC reactions; approximately

50% of the energy is carried out by the secondary neutrino and the remaining energy goes to particles which travel longer distances in water than electrons.

As the main background rejecting criterion involves the total amplitude of the hits in an event (§ 6.2.3), a more detailed study of the charge of the hits is useful. The dedicated data-taking runs which are used to perform the charge calibration (§ 2.5.2) can be used to test the real response of the detector at events with such large amplitudes (> 2300 p.e.).

Finally, using the selection criteria optimized for the Monte Carlo samples, the search for the diffuse flux of high energy neutrinos and antineutrinos which induce showers will be done with the data collected by ANTARES. Hence, the ANTARES effective area with respect to shower-like events has to be evaluated, and an energy estimator has to be developed.

Appendix A

ANTARES Analysis Chain

In this appendix, a description of the ANTARES analysis chain is presented, as far as it was used for the presented study. § A.1 describes the Monte Carlo event generators of atmospheric muons, and of atmospheric and cosmic neutrinos. The Cherenkov light production and the detector simulation are described in § A.2. The implementation of the optical background in Monte Carlo simulations and the trigger selections are introduced in § A.3. Finally, the reconstruction algorithm is presented in § A.4.

A.1 Monte Carlo Event Generators

The ANTARES analysis chain starts with the generation of muons or neutrinos reaching the *can* surface¹ of the ANTARES detector.

The dimensions of the can are computed by adding 2.5 absorption lengths λ_{abs} (§ 2.1) to the instrumented volume. Hence, the ANTARES can size is:

$$\begin{cases} H_{can} = 587.09 \text{ m} \\ R_{can} = 238.68 \text{ m} \end{cases}$$

For this analysis, atmospheric muons are generated with the MUPAGE code, while neutrinos are generated with the *genhen* code.

A.1.1 MUPAGE

The MUPAGE code [56] has been described in details in Chapter 4. This analysis uses the latest version of MUPAGE (v2²).

As described in § 4.1, the ANTARES can in MUPAGE has to be extended in order to accept peripheral muons. Hence the radius of the can becomes $R_{can} = 338.68 \text{ m}$.

¹The can is a virtual cylinder surrounding the active volume of a generic underwater/ice neutrino telescope.

²Official version v2 corresponds to v3r4 within the ANTARES Collaboration.

Note that MUPAGE generates the events according to their abundance, and therefore no weighting of the events is needed. Each set of events corresponds to a certain livetime (§ 4.5) in units of seconds. Hence to obtain the event rate (in Hz), the number of events has to be divided by the calculated livetime.

A.1.2 Genhen

The atmospheric neutrino flux reaching the can surface of the ANTARES detector is simulated with the FORTRAN code `genhen` [107]. The latest version of `genhen` (v6r4 within the ANTARES Collaboration) allows to generate all neutrino flavors with NC or CC interactions, according to the CTEQ6-DIS [96] parton distribution functions (described in § 5.4). The Glashow resonance for (anti-)electron neutrinos as well as the propagation through the Earth of upward going (anti)neutrinos (§ 5.5) are also taken into account.

The output of `genhen` includes the kinematics information of the primary neutrino: its energy, flavor, direction, position of the interaction vertex and of the long-lived secondary particles produced in the interaction.

The program provides the possibility to generate events according to different models of the atmospheric conventional neutrino flux, such as the Bartol flux [57], as well as the prompt flux, such as the RQPM [90]. The differential flux of atmospheric neutrinos chosen in the generation is implemented in the weight **w3** as Φ . The weights of each event are defined as:

w1: contains the can volume [m^3].

w2: contains the generation weight. For the generation of neutrino interactions, which are flat in cosine of zenith angle and flat in $E^{-\gamma}$:

$$\mathbf{w2} = \mathbf{w1} \cdot I_{\theta} \cdot I_E \cdot E^{\gamma} \cdot \sigma(E) \cdot \rho N_A \cdot P_{Earth} \cdot F \quad (\text{A.1})$$

where I_{θ} [sr] is the angular phase factor $2\pi[\cos(\theta_{max}) - \cos(\theta_{min})]$; I_E is the energy phase space factor $(E_{max}^{1-\gamma} - E_{min}^{1-\gamma})/(1-\gamma)$ if $\gamma \neq 1$, or $\ln(E_{max}/E_{min})$ for $\gamma = 1$; the factor E^{γ} takes into account that the generation has been done flat in $E^{-\gamma}$, hence $I_E \cdot E^{\gamma}$ is measured in GeV; $\sigma(E)$ [m^2] is the total neutrino cross section for neutrino energy E ; ρN_A is the number of target nucleons per m^3 ; P_{Earth} is the probability for the neutrino to traverse the Earth (depending on energy and zenith angle); and F is the number of seconds per year [s/year].

Hence, **w2** has the following units: $\text{GeV m}^2 \text{ s sr year}^{-1}$.

w3: is defined as

$$\mathbf{w3} = \mathbf{w2} \cdot \Phi \quad (\text{A.2})$$

where Φ is the differential flux of neutrinos (in units of $\text{GeV}^{-1} \text{m}^{-2} \text{s}^{-1} \text{sr}^{-1}$) as selected during the generation (e.g. the Bartol flux) before penetrating the Earth. Therefore, **w3** has the simple units [year^{-1}] which can be understood as a ‘rate per year’.

Therefore, weighting the generated events with **w3**, one has the number of atmospheric neutrino events per year according to the generated flux Φ (e.g. the Bartol flux). While, to obtain the number of astrophysical neutrino events per year, the generated events have to be weighted with $\mathbf{w2} \times E^{-2} \times$ a cosmic neutrino flux, such as the Waxman-Bahcall (§ 5.2).

A.2 Cherenkov Light Production and Detector Simulation

The tracking of particles through the ANTARES active volume, the production of Cherenkov light by charged particles and the detector response, such as the signal digitization (§ 2.4.1), are simulated using the KM3 package in the case of muons. The `geasim` code is used for all other particles.

A.2.1 KM3

The KM3 package of FORTRAN codes [108] allows for a full simulation of the ANTARES response to the passage of high energy muons including the effect of photon scattering in the water. As the number of photons emitted along the muon trajectory is large, the simulation of the light production is very time consuming. For this reason, a set of tables storing amplitude and time of Cherenkov photons hitting the PMTs is created. They are constructed taking into account the water properties of the ANTARES site (light absorption length and scattering model), the characteristics of the OMs (geometry and efficiency, § 2.2) and the position, distance and orientation of an OM with respect to a given muon track.

For this analysis, the latest version of KM3 (v3r6 within the ANTARES Collaboration) has been used.

A.2.2 Geasim

The tracking of particles other than muons is done with the `geasim` package which is based on GEANT 3.21 [109]. All relevant physics processes that can occur during the passage

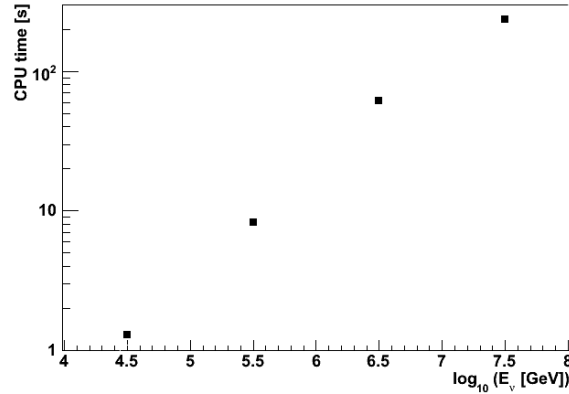


Figure A.1: Average CPU time for one event in `geasim` as a function of the neutrino energy.

of particles through the water are taken into account, as well as the characteristics of the OMs (geometry and efficiency, § 2.2). However, scattering effects are not simulated; the number of photons is only decreased according to the attenuation length.

For hadronic showers, no parameterizations are implemented and every single particle in the shower is tracked down to the Cherenkov level. This is very time consuming and energy dependent. As shown in Figure A.1, the average CPU time¹ necessary to process one event in the simulation of this thesis rises almost exponentially with energy. The average CPU time is determined by processing at least 300 events for each decade of energy.

The significant processing time makes the production of events above roughly 10 PeV a considerable task. There are also some known errors in the cross sections from GEANT 3. The authors of `geasim` therefore do not recommend the usage above 100 TeV, although events have been produced within this work up to energies of 100 PeV without displaying any obvious flaws other than technical ones².

For this analysis, the latest version of `geasim` (v4r10 within the ANTARES Collaboration) has been used.

A.3 Trigger Selection

In order to identify potentially interesting events, an online trigger algorithm [110] is applied to real data. The trigger algorithm search for hits which are causally connected and/or have a sufficiently large amplitude. When the trigger conditions are fulfilled, a

¹Using a 2.33 GHz computer and Scientific Linux 4.

²For example, the maximum number of tracking steps (10000) is reached for some of the showers produces at the highest energies, and the program simply discards the track. Hence not all tracks are followed down to the Cherenkov level.

so-called *physics event* is built.

The trigger conditions define a L0 hit as a hit with amplitude larger than 0.3 p.e. An L1 hit is defined either as 2 L0 hits in coincidence within 20 ns in two OMs of the same storey or as a single L0 hit with an amplitude larger than 3 p.e.

The most common applied selection criteria are referred to as 3D-scan Trigger (shortened as 3N) and/or 2T3 Trigger (shortened as T3). The 3N Trigger requires at least 5 causally connected L1 hits. A 1T3 cluster is defined as 2 L1 hits in adjacent or next-to-adjacent storeys, in coincidence within 100 ns or 200 ns, respectively. The T3 trigger seeks for time coincidence between two 1T3 clusters, in the whole detector, within 2.2 μ s. These two 1T3 clusters can be located on the same detector line or on different lines. In the former case, 3 L1 hits on three adjacent storeys can lead to a triggered event.

An offline code (TriggerEfficiency [111]) is dedicated to the treatment of Monte Carlo events. It adds the background hits due to ^{40}K and bioluminescence (§ 2.6) and applies the same trigger criteria defined in the online trigger, to select candidate events in the Monte Carlo samples. The background added to Monte Carlo samples is taken from data to reproduce the real acquisition conditions such as the number of active OMs, low efficiency PMTs, baseline rate and bursts due to bioluminescence.

A.4 Reconstruction Algorithm

Several reconstruction algorithms are available to process (real and Monte Carlo) triggered events in the ANTARES analysis chain. A brief description of the results on the neutrino event reconstruction can be found in [112]. The analysis described in this thesis uses the so-called BBFit reconstruction algorithm [113], which is included in the BBdisp package. The latest version of this package (v3r5 within the ANTARES Collaboration) has been used.

As an official documentation of BBFit is not available yet, a description of this strategy is presented here.

The BBFit algorithm is based on a chisquare-like minimization and is designed to reconstruct muon tracks as well as so-called *bright point* events. A bright point is a point-like light source which emits a single light flash (assumed as isotropic) at a given moment. The model of a bright point applies not only to artificial light sources such as LED and laser beacons (§ 2.5.1), but also to sparks (as have been occasionally observed in some optical modules) and to light from hadronic and electromagnetic showers, for which the spatial extension of the shower is significantly smaller than the typical size of the detector.

BBFit approximates each storey as a space point centered on a vertical detector line. After the application of time and charge calibrations (§ 2.5), the hits in the event are time ordered and merged on each storey if closer than 20 ns. In this case, the time of the first hit is taken and the charges are summed. In order to augment the weight of coincidences with respect to single high charge pulses, the total charge is further increased by 1.5 p.e. if the hits originate from different OMs of the same storey. All hits, merged or single, having a minimal charge of 2.5 p.e. are defined as step-1 hits. Next, a selection analogous to the Trigger T3 requirements (§ A.3) is applied: A cluster of step-1 hits requires the presence of 2 step-1 hits within 80 ns on two adjacent storeys or within 160 ns on next-to-adjacent storeys. Only detector lines having at least one cluster are considered in the prefit selection, in order to avoid the attribution of isolated noise hits to a track. Finally, at least 5 hits in the whole detector lines are required to start the fit.

A.4.1 Fitting Procedure

If all selected hits are on a single detector line, a reconstruction algorithm for single line is started, otherwise multi-line fit procedure is applied. The analysis presented in this thesis uses only the multi-line fit as described in the following.

A.4.1.1 Particle Track

A particle track is considered as a straight line in space (multiple scattering and other effects which could deviate the particle from its straight trajectory are ignored). The particle is assumed to move with the speed of light in vacuum. All space-time points \vec{p} on the track can be parameterized as

$$\vec{p}(t) = \vec{q}(t_0) + c(t - t_0)\vec{v} \quad (\text{A.3})$$

where $\vec{q}(t_0)$ is the particle position at time t_0 and \vec{v} represents the track direction. The track can be defined by a total of 5 parameters: three values to fix \vec{q} for a given time and two angles to define \vec{v} . Considering an exactly vertical detector line along the z -axis, i.e. given by $(0, 0, z)$, from purely geometrical considerations the point of closest approach between the detector line and the particle track can be defined. The point of closest approach along the z -axis is

$$z_c = \frac{q_z - v_z(\vec{q} \cdot \vec{v})}{1 - v_z^2} \quad (\text{A.4})$$

through which the particle passes at time

$$t_c = t_0 + \frac{q_z v_z - (\vec{q} \cdot \vec{v})}{c(1 - v_z^2)} \quad (\text{A.5})$$

at a distance

$$d_c = q\sqrt{p_x^2(t_c) + p_y^2(t_c) + (p_z(t_c) - z_c)^2} \quad (\text{A.6})$$

If the track is exactly vertical, i.e. parallel to the detector line (condition $|v_z| > 0.9999$ in the code), then $t_c = t_0$ and $z_c = q_z$ are chosen.

To build a fitting function it is necessary to know the arrival time t_γ of a Cherenkov photon at the detector line position $(0, 0, z)$, its corresponding travel path d_γ and its inclination with respect to the detector line $\cos \theta_\gamma$:

$$d_\gamma(z) = \frac{n}{\sqrt{n^2 - 1}} \sqrt{d_c^2 + (z - z_c)^2(1 - v_z^2)} \quad (\text{A.7})$$

$$t_\gamma(z) = (t_c - t_0) + \frac{1}{c} \left[(z - z_c) v_z + \frac{n^2 - 1}{n} d_\gamma(z) \right] \quad (\text{A.8})$$

$$\cos \theta_\gamma(z) = (1 - v_z^2) \frac{z - z_c}{d_\gamma(z)} + \frac{v_z}{n} \quad (\text{A.9})$$

These equations hold exactly for Cherenkov photons of a given wavelength. Dispersion and group velocity effects, as well as delays due to light scattering in a medium, are ignored. A refractive index $n = 1.38$ is used in the code.

A.4.1.2 Bright Point

A bright point is defined by four parameters: its position \vec{q} and its time t_0 . In analogy with the definitions of the point of closest approach as done for particle tracks, it is straightforward to see that for a bright point $z_c = q_z$, $t_c = t_0$ and

$$d_c = \sqrt{q_x^2 + q_y^2} \quad (\text{A.10})$$

The photon arrival time t_γ , its travel length d_γ and its angle with respect to a given arrival point z along the detector line can thus be determined in analogy to the case of a particle track:

$$d_\gamma(z) = \sqrt{d_c^2 + (z - q_z)^2} \quad (\text{A.11})$$

$$t_\gamma(z) = t_0 + \frac{n}{c} d_\gamma \quad (\text{A.12})$$

$$\cos \theta_\gamma(z) = \frac{z - q_z}{d_\gamma} \quad (\text{A.13})$$

As for particle tracks, it is assumed that all photons have one particular wavelength, such that a refractive index of $n = 1.38$ is appropriate.

A.4.1.3 Fit Function

The fitting function exploits the time difference between the hit times t_i and the expected arrival times of photons from the track or bright point t_γ , as in a standard χ^2 fit. Furthermore, the expected amplitude versus distance relation of the measured hit amplitudes a_i is used.

$$Q = \sum_{i=1}^{N_{hit}} N_{hit} \left[\frac{(t_\gamma - t_i)^2}{\sigma_i^2} + \frac{a(a_i) d(d_\gamma)}{\langle a \rangle d_0} \right] \quad (\text{A.14})$$

The timing error σ_i is set to 10 ns for $a_i > 2.5$ p.e. and to $\sigma_i = 20$ ns otherwise. These values might seem large with respect to the transit time spread of 1.3 ns for the ANTARES PMTs, but have been confirmed by exploring the time residuals of typical track fits.

The second term is not organized as a difference between theoretical value and measured amplitude in order to avoid penalties from large theoretical amplitudes. Instead, the chosen form gives a penalty to the combination of high amplitude and large distance. The product is normalized by the average amplitude $\langle a \rangle$ to compensate for the fact that higher energy tracks or showers will produce more light at the same distance. The normalization $d_0 = 50$ m serves to balance the weight between the two terms. Hit amplitudes a_i and photon travel distances d_γ are not taken directly from the calibrated detector measurements. The amplitudes are first corrected for the angular acceptance of the storey. A very simple form can be numerically derived from the arrangement of the OMs in a storey and the corresponding angular acceptance function of a single OM. This leads to a corrected hit amplitude a'_i of

$$a'_i = \frac{2a_i}{\cos \theta_\gamma + 1} \quad (\text{A.15})$$

The average amplitude $\langle a \rangle$ is calculated from these corrected hit amplitudes

$$\langle a \rangle = \frac{1}{N_{hit}} \sum_1^{N_{hit}} a'_i \quad (\text{A.16})$$

To be used in the fit function, the amplitudes are further modified

$$a(a_i) = \frac{a_0 a'_i}{\sqrt{a_0^2 + a_i'^2}} \quad (\text{A.17})$$

The function $a(a_i)$ introduces an artificial saturation such that for $a'_i \ll a_0$ one finds back $a \simeq a'_i$, whereas for $a'_i \gg a_0$, one gets $a \simeq a_0$: the saturation value of $a_0 = 10$ p.e. This limits the influence of the large dispersion in the dynamic ranges of the different modules which is currently not simulated.

A similar trick is applied to the photon travel distance

$$d(d_\gamma) = \sqrt{d_1^2 + d_\gamma^2} \quad (\text{A.18})$$

For large distances $d_\gamma \gg d_1$ one finds back $d \simeq d_\gamma$, whereas for very small distances $d_\gamma \ll d_1$ one gets $d \simeq d_1$ with $d_1 = 5$ m. This avoids an excessive pull of the fit object towards the detector line.

The somewhat arbitrary choice of introducing Eqs. (A.17) and (A.18) can be justified by the following consideration. The intensity of Cherenkov light decreases linearly with distance (ignoring dispersion and similar effects). Thus one can write $a'_i d_\gamma = a_0 d_1$, which corresponds to the observation that about 50 p.e. can be measured for a minimally ionizing particle at 1 m distance, or equivalently 1 p.e. is seen at a distance of 50 m. Using this identity, one can show that $a(a'_i) d(d_\gamma) = a'_i d_\gamma$, i.e. the two functions have absolutely no effect on the product of amplitude times distance.

A.4.1.4 Minimization Procedure

The MIGRAD function of the MINUIT package [114] is used to perform the actual minimization. Eqs. (A.7), (A.8), (A.9), (A.11), (A.12) and (A.13) are used to obtain d_γ , t_γ , $\cos \theta_\gamma$ for a given particle track or bright point. A loop is performed over all detector lines which have selected hits, and for each line a coordinate transformation is done to place the line at the nominal position $(x, y) = (0, 0)$. After minimization, the value of the fit quality Q divided by the number of degrees of freedom is retained for further analysis and it is stored in the resulting n-tuple. The covariance matrix is not used.

The multi-line bright point fit is insensitive to the choice of its initial parameters which are simply fixed to constant values: $\vec{q} = (0, 0, 250)$ m and $t_0 = 0$. The multi-line track fit requires a prefit, however. The usual ‘DUMAND’ prefit is used, which represents a linear fit through the positions of the hits while allowing for a variable particle speed. The result of the prefit is not used for further analysis.

A.4.2 Event Display

The BBdisp package includes also an application (BBdispfil) which fills a two-dimensional event display. For each detector line, the horizontal axis indicates hit time (in ns) and the vertical axis shows the height above the seabed of the fired storey (in m).

In this appendix, two examples of the event display are shown. Both of them refer to the reconstruction of Monte Carlo events. In practice, this 2-D event display is used to check in real time the acquisition of data events.

Figure A.2 shows an example of a downward going Monte Carlo muon, which is reconstructed as a track. The value (in degrees) of the reconstructed zenith angle is displayed in the top-left corner and it is compared with the value of the generated zenith angle in the Monte Carlo sample (so-called MC truth). If the zenith angle has a value larger than 90 degrees the event is downward going, otherwise it is upward going. In this specific example, the muon is reconstructed on 10 out of 12 detector lines. In each display, corresponding to each detector line, the black crosses represent hits in a time window of $3 \mu\text{s}$ around the trigger, full circles indicate hits participating in the trigger and open boxes designate those hits which have been used in the fit.

Figure A.3 shows an example of an upward going Monte Carlo electron neutrino, which is reconstructed as a bright point. In the bright point case, the reconstruction algorithm does not compute any zenith angle for construction. It is therefore impossible to evaluate if the event was originally downward or upward going. In this specific example, the electron neutrino is reconstructed on 11 out of 12 detector lines.

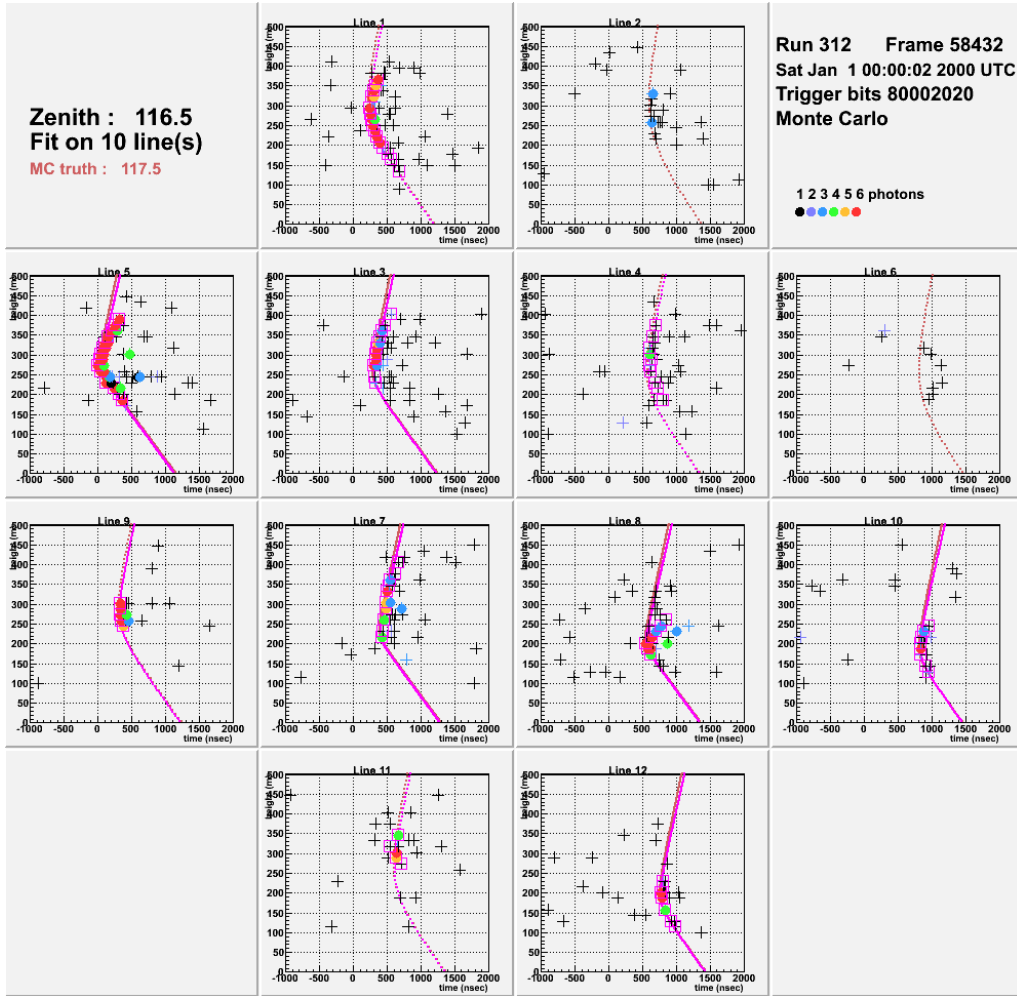


Figure A.2: A downward going Monte Carlo muon reconstructed as a track on 10 out of 12 detector lines. The value (in degrees) of the reconstructed zenith angle is displayed in the top-left corner and it is compared with the value of the generated zenith angle in the Monte Carlo sample ('MC truth'). In each display, the curve shows the signature of the reconstructed muon track, i.e. the z -position of the Cherenkov cone with respect to the seabed, as a function of the time. The black crosses represent hits in a time window of $3 \mu\text{s}$ around the trigger, full circles indicate hits participating in the trigger and open boxes designate those hits which have been used in the fit.

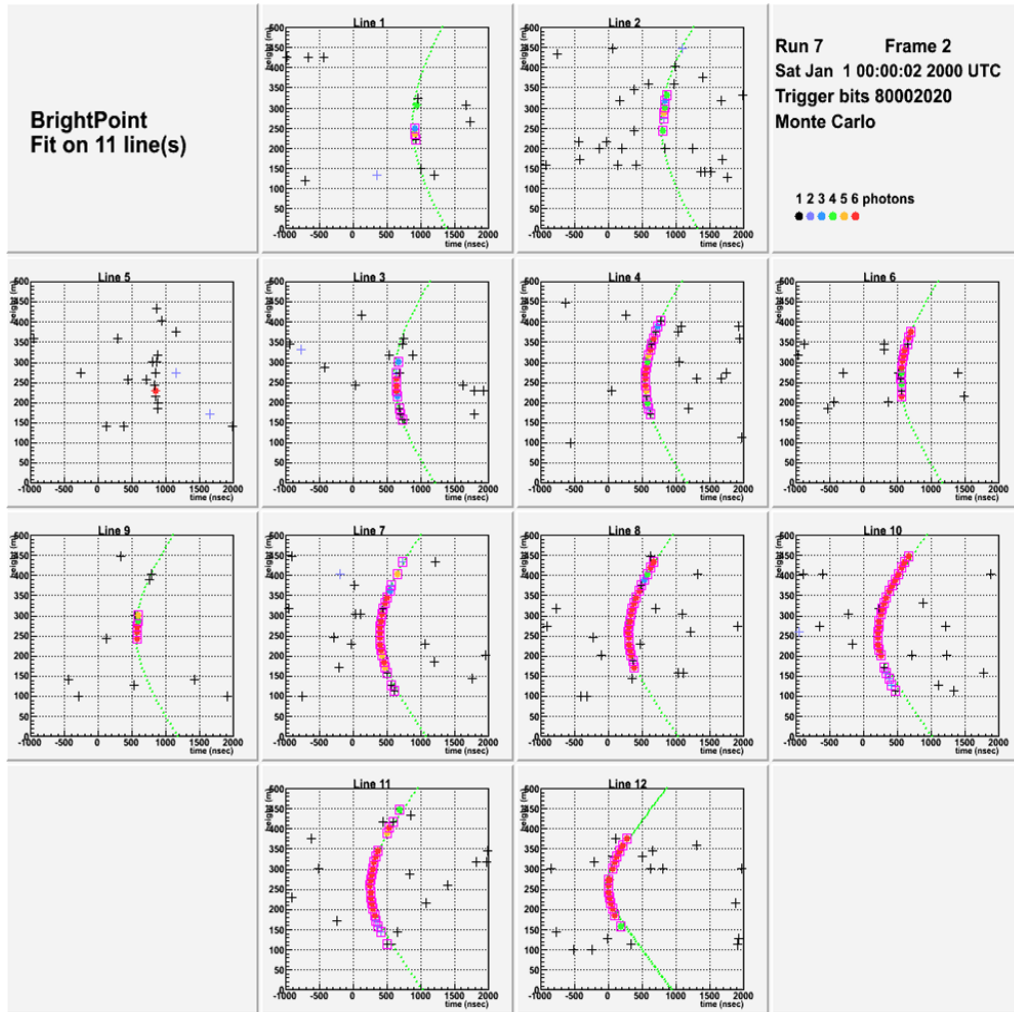


Figure A.3: An upward going Monte Carlo electron neutrino reconstructed as a bright point on 11 out of 12 detector lines. In each display, the curve shows the signature of the reconstructed shower event, i.e. the z -position of the Cherenkov cone with respect to the seabed, as a function of the time. The black crosses represent hits in a time window of $3 \mu\text{s}$ around the trigger, full circles indicate hits participating in the trigger and open boxes designate those hits which have been used in the fit.

References

- [1] M.A. MARKOV, On high energy neutrino physics, *Proceedings of the 10th Int. Conf. on High Energy Physics*, Rochester, NY, U.S.A. (1960).
- [2] C. AMSLER et al. (Particle Data Group), Astrophysics and Cosmology, 24. Cosmic Rays, *Phys. Lett. B* **667**, 254-260 (2008).
- [3] V.L. GINZBURG, Y.M. KHAZAN, V.S. PTUSKIN, Origin of Cosmic Rays: Galactic models with halo, *Astrophysics and Space Science* **68**, 295-314 (1980).
- [4] D.J. BIRD et al. (HiRes Collaboration), The cosmic ray energy spectrum observed by the Fly's Eye, *Astrophys. J.* **424**, 491-502 (1994).
- [5] F. HALZEN, D. HOOPER, High-energy neutrino astronomy: the cosmic ray connection, *Rep. Prog. Phys.* **65**, 1025-1078 (2002).
- [6] A.A. PENZIAS, R.W. WILSON, A Measurement of excess antenna temperature at 4080-Mc/s, *Astrophys. J.* **142**, 419-421 (1965).
- [7] K. GREISEN, End to the Cosmic Spectrum?, *Phys. Rev. Lett.* **16**, 748-750 (1966).
- [8] G.T. ZATSEPIN, V.A. KUZ'MIN, Upper Limit of the Spectrum of Cosmic Rays, *JETP Lett.* **4**, 78-80 (1966).
- [9] M. NAGANO, A.A. WATSON, Observation and implications of the ultrahigh-energy cosmic rays, *Rev. Mod. Phys.* **72**, 689-732 (2000).
- [10] J. ABRAHAM et al. (Pierre Auger Collaboration), Correlation of the Highest-Energy Cosmic Rays with Nearby Extragalactic objects, *Science* **318**, 938-943 (2007);
- J. ABRAHAM et al. (Pierre Auger Collaboration), Correlation of the highest-energy cosmic rays with the positions of nearby active galactic nuclei, *Astropart. Phys.* **29**, 188-204 (2008);
- J.D. HAGUE (for the Pierre Auger Collaboration), Correlation of the Highest Energy Cosmic Rays with Nearby Extragalactic Objects in Pierre Auger Observatory Data, *Proceedings of the 31st ICRC*, Łódź, Poland (2009).
- [11] M. TAKEDA et al. (AGASA Collaboration), Energy determination in the Akeno Giant Air Shower Array experiment, *Astropart. Phys.* **19**, 447-462 (2003).
- [12] R.U. ABBASI et al. (HiRes Collaboration), First Observation of the Greisen-Zatsepin-Kuzmin Suppression, *Phys. Rev. Lett.* **100**, 101101 (2008).
- [13] J. ABRAHAM et al. (Pierre Auger Collaboration), Observation of the Suppression of the Flux of Cosmic Rays above 4×10^{19} eV, *Phys. Rev. Lett.* **101**, 061101 (2008);
- F. SCHÜSSLER (for the Pierre Auger Collaboration), Measurement of the cosmic rays energy spectrum above 10^{18} eV using the Pierre Auger Observatory, *Proceedings of the 31st ICRC*, Łódź, Poland (2009).
- [14] F. AHARONIAN et al., High energy astrophysics with ground-based gamma ray detectors, *Rep. Prog. Phys.* **71**, 096001 (2008).
- [15] V. BEREZINSKY et al., Astrophysics of Cosmic Rays, North-Holland, Amsterdam, The Netherlands (1990).
- [16] C. STEGMANN et al., Potential neutrino signals in a northern hemisphere neutrino telescope from galactic gamma-ray sources, *Astrophys. Space Sci.* **309**, 429-433 (2007).
- [17] E. FERMI, On the Origin of the Cosmic Radiation, *Phys. Rev.* **75**, 1169-1174 (1949).
- [18] E. DE OÑA WILHELMI (for the H.E.S.S. Collaboration), Status of the H.E.S.S. telescope, *AIP Conf. Proc.* **1112**, 16-22 (2009).

- [19] R.A. ONG et al., Highlight Talk: Recent Results from VERITAS, *Proceedings of the 31st ICRC*, Łódź, Poland (2009), e-Print: [arXiv:0912.5355](https://arxiv.org/abs/0912.5355) [astro-ph.HE].
- [20] E. CARMONA (for the MAGIC Collaboration), Results from the MAGIC gamma-ray telescope, *J. Phys.: Conf. Ser.* **171**, 012046 (2009).
- [21] F. AHARONIAN, The Very-High-Energy Gamma-Ray Sky, *Science* **315**, 70-72 (2007).
- [22] M.C. GONZALEZ-GARCIA, F. HALZEN, S. MOHAPATRA, Identifying Galactic PeVatrons with neutrinos, *Astropart. Phys.* **31**, 437-444 (2009).
- [23] F.L. VILLANTE, F. VISSANI, Method to extract the primary cosmic ray spectrum from very high energy γ -ray data and its application to SNR RX J1713.7-3946, *Phys. Rev. D* **76**, 125019 (2007).
F.L. VILLANTE, F. VISSANI, How precisely can neutrino emission from supernova remnants be constrained by gamma ray observations?, *Phys. Rev. D* **78**, 103007 (2008).
- [24] A. LEVINSON, E. WAXMAN, Probing Microquasars with TeV Neutrinos, *Phys. Rev. Lett.* **87**, 171101 (2001).
- [25] C. DISTEFANO et al., Neutrino Flux Predictions for Known Galactic Microquasars, *Astrophys. J.* **575**, 378-383 (2002).
- [26] H.J. VÖLK, P.L. BIERMANN, Maximum energy of cosmic-ray particles accelerated by supernova remnant shocks in stellar wind cavities, *Astrophys. J.* **333**, L65-L68 (1988).
- [27] A.M. HILLAS, The Origin of Ultra-High-Energy Cosmic Rays, *Ann. Rev. Astron. Astrophys.* **22**, 425-444 (1984).
- [28] T. CHIARUSI, M. SPURIO, High-Energy Astrophysics with Neutrino Telescope, *Eur. Phys. J. C* **65**, 649-701 (2010).
- [29] E. WAXMAN, J. BAHCALL, High energy neutrinos from astrophysical sources: An upper bound, *Phys. Rev. D* **59**, 023002 (1998);
J. BAHCALL, E. WAXMAN, High energy astrophysical neutrinos: The upper bound is robust, *Phys. Rev. D* **64**, 023002 (2001).
- [30] P.L. BIERMANN, The origin of the highest energy cosmic rays, *J. Phys. G: Nucl. Part. Phys.* **23**, 1-27 (1997).
- [31] B.L. FANAROFF, J.M. RILEY, The morphology of extragalactic radio sources of high and low luminosity, *Mon. Not. Roy. Astron. Soc.* **167**, 31-36 (1974).
- [32] E. BOLDT, P. GHOSH, Cosmic rays remnants of quasars?, *Mon. Not. Roy. Astron. Soc.* **307**, 491-494 (1999).
- [33] P. MESZAROS, Gamma-ray bursts, *Rep. Prog. Phys.* **69**, 2259-2321 (2006).
- [34] E. WAXMAN, Cosmological Gamma-Ray Bursts and the Highest Energy Cosmic Rays, *Phys. Rev. Lett.* **75**, 386-389 (1995).
- [35] P. SAPIENZA, G. RICCOBENE, High-energy neutrino astronomy, *Riv. Nuovo Cimento* **32**, 591-650 (2009).
- [36] A. LOEB, E. WAXMAN, The cumulative background of high energy neutrinos from starburst galaxies, *JCAP* **05**, 003 (2006).
- [37] P. BHATTACHARJEE, G. SIGL, Origin and Propagation of Extremely High Energy Cosmic Rays, *Phys. Rep.* **327**, 109-247 (2000).
- [38] P. BHATTACHARJEE, C.T. HILL, D.N. SCHRAMM, Grand Unified Theories, Topological Defects, and Ultrahigh-Energy Cosmic Rays, *Phys. Rev. Lett.* **69**, 567-570 (1992).
- [39] T. WEILER, Resonant Absorption of Cosmic-Ray Neutrinos by the Relic-Neutrino Background, *Phys. Rev. Lett.* **49**, 234-237 (1982);
T.J. WEILER, Cosmic-ray neutrino annihilation on relic neutrinos revisited: a mechanism for generating air showers above the Greisen-Zatsepin-Kuzmin cutoff, *Astropart. Phys.* **11**, 303-316 (1999).
- [40] R. ENGEL, D. SECKEL, T. STANEV, Neutrinos from propagation of ultrahigh energy protons, *Phys. Rev. D* **64**, 093010 (2001).

- [41] E. WAXMAN, Extra galactic sources of high energy neutrinos, *Phys. Scripta* **T121**, 147-152 (2005).
- [42] P.A. ČHERENKOV, Visible Radiation Produced by Electrons Moving in a Medium with Velocities Exceeding that of Light, *Phys. Rev.* **52**, 378-379 (1937).
- [43] J.D. JACKSON, Classical Electrodynamics, 3rd Ed., John Wiley and Sons, Inc., New York, NY, U.S.A. (1998).
- [44] P. COYLE (for the ANTARES Collaboration), Highlight Talk: The ANTARES Deep-Sea Neutrino Telescope: Status and First Results, *Proceedings of the 31st ICRC*, Łódź, Poland (2009), e-Print: [arXiv:1002.0754](https://arxiv.org/abs/1002.0754) [astro-ph.HE].
- [45] <http://maps.google.com>
- [46] P. AMRAM et al. (ANTARES Collaboration), The ANTARES optical module, *Nucl. Instrum. Methods A* **484**, 369-383 (2002).
- [47] J.A. AGUILAR et al. (ANTARES Collaboration), The data acquisition system for ANTARES neutrino telescope, *Nucl. Instrum. Methods A* **570**, 107-116 (2007).
- [48] <http://root.cern.ch>
- [49] M. AGERON et al. (ANTARES Collaboration), The ANTARES Optical Beacon System, *Nucl. Instrum. Methods A* **578**, 498-509 (2007).
- [50] J.A. AGUILAR et al. (ANTARES Collaboration), Measurement of the atmospheric muon flux with a 4 GeV threshold in the ANTARES neutrino telescope, *Astropart. Phys.* **33**, 86-90 (2010).
- [51] B. BARET (for the ANTARES Collaboration), Charge Calibration of the ANTARES high energy neutrino telescope, *Proceedings of the 31st ICRC*, Łódź, Poland (2009), e-Print: [arXiv:0908.0810](https://arxiv.org/abs/0908.0810) [astro-ph.IM].
- [52] A.M. BROWN (for the ANTARES Collaboration), Positioning system of the ANTARES Neutrino Telescope, *Proceedings of the 31st ICRC*, Łódź, Poland (2009), e-Print: [arXiv:0908.0814](https://arxiv.org/abs/0908.0814) [astro-ph.IM].
- [53] J. BRUNNER, Upgrade of K40 simulation, ANTARES-PHYS-2006-005.
- [54] C. FORTI et al., Simulation of atmospheric cascades and deep-underground muons, *Phys. Rev. D* **42**, 3668-3689 (1990).
- [55] Y. BECHERINI et al., A parameterisation of single and multiple muons the deep water or ice, *Astropart. Phys.* **25**, 1-13 (2006).
- [56] G. CARMINATI et al., Atmospheric MUons from Parametric formulas: a fast Generator for neutrino telescopes (MUPAGE), *Comput. Phys. Commun.* **179**, 915-923 (2008); M. BAZZOTTI et al., An update of the generator of atmospheric muons from parametric formulas (MUPAGE), *Comput. Phys. Commun.* **181**, 835-836 (2010).
- [57] V. AGRAWAL et al., Atmospheric neutrino flux above 1 GeV, *Phys. Rev. D* **53**, 1314-1323 (1996); G.D. BARR et al., Three-dimensional calculation of atmospheric neutrinos, *Phys. Rev. D* **70**, 023006 (2004).
- [58] K. GREISEN, Cosmic Ray Showers, *Ann. Rev. Nucl. Part. Sci.* **10**, 63-108 (1960).
- [59] L. PASQUALI, M.H. RENO, Tau neutrino fluxes from atmospheric charm, *Phys. Rev. D* **59**, 093003 (1999).
- [60] T.S. SINEGEVSKAYS, S.I. SINEGOVSKY, Prompt muon contribution to the flux underwater, *Phys. Rev. D* **63**, 096004 (2001).
- [61] P. LE COULTRE, The L3+Cosmics experiment, *Nuclear Phys. B (Proc. Suppl.)* **122**, 161-169 (2003).
- [62] S.I. NIKOLSKY, J.N. STAMENOV, S.Z. USHEV, Composition Of Cosmic Radiation At Energies Approximately 10^{15} eV And Above, *Sov. Phys. JETP* **60**, 10-21 (1984) [*Zh. Eksp. Teor. Fiz.* **87**, 18-36 (1984)].
- [63] J.R. HÖRANDEL, On the knee in the energy spectrum of cosmic rays, *Astropart. Phys.* **19**, 193-220 (2003).
- [64] A. FASSÒ et al., The physics models of FLUKA: status and recent developments, *Proceedings of CHEP 03*,

- La Jolla, CA, U.S.A. (2003), e-Print: [arXiv:physics/0306162](https://arxiv.org/abs/physics/0306162).
- [65] M. AMBROSIO et al. (MACRO Collaboration), High energy cosmic ray physics with underground muons in MACRO. I. Analysis methods and experimental results, *Phys. Rev. D* **56**, 1407 (1997); M. AMBROSIO et al. (MACRO Collaboration), High energy cosmic ray physics with underground muons in MACRO. II. Primary spectra and composition, *Phys. Rev. D* **56**, 1418 (1997).
- [66] J. RANFT, Dual parton model at cosmic ray energies, *Phys. Rev. D* **51**, 64 (1995).
- [67] B. WIEBEL-SOOTH et al., Cosmic Rays. VII. Individual element spectra: prediction and data, *Astron. Astrophys.* **330**, 389-398 (1998).
- [68] A.D. PANOV et al., The results of ATIC-2 experiment for elemental spectra of cosmic rays, *Bull. Rus. Acad. Sci.: Phys.* **71**, 494 (2007).
- [69] V.A. DERBINA et al. (RUNJOB Collaboration), Cosmic-ray spectra and composition in the energy range of 10-1000 TeV per particle obtained by the RUNJOB experiment, *Astrophys. J.* **628**, L41-L44 (2005).
- [70] T. ANTONI et al., KASKADE measurements of energy spectra for elemental groups of cosmic rays: Results and open problems, *Astropart. Phys.* **24**, 1-25 (2005).
- [71] S.P. SWORDY, D.B. KIEDA, Elemental composition of cosmic rays near the knee by multiparameter measurements of air shower, *Astropart. Phys.* **13**, 137-150 (2000).
- [72] J.W. FOWLER et al., A measurement of the cosmic ray spectrum and composition at the knee, *Astropart. Phys.* **15**, 49-64 (2001).
- [73] D.V. CHERNOV et al., Primary energy spectrum and mass composition determined with the TUNKA EAS Cherenkov array, *Int. J. Mod. Phys. A* **20**, 6799-6801 (2005); N.M. BUDNEV et al., Cosmic Ray Energy Spectrum and Mass Composition from 10^{15} to 10^{17} eV by Data of the Tunka EAS Cherenkov Array, *Proceedings of the 29th ICRC*, Pune, India (2005), e-Print: [arXiv:astro-ph/0511215](https://arxiv.org/abs/astro-ph/0511215).
- [74] M. NAGANO et al., Energy spectrum of primary cosmic rays between $10^{14.5}$ and 10^{18} eV, *J. Phys. G: Nucl. Part. Phys.* **10**, 1295-1314 (1984).
- [75] G. BATTISTONI et al., Study of the high energy cosmic ray cascades using the dual parton model, *Astropart. Phys.* **3**, 157-184 (1995).
- [76] P. ANTONIOLI et al., A three-dimensional code for muon propagation through the rock: MUSIC, *Astropart. Phys.* **7**, 357-368 (1997).
- [77] CH. BERGER et al. (Fréjus Collaboration), Experimental study of muon bundles observed in the Fréjus detector, *Phys. Rev. D* **40**, 2163-2171 (1989).
- [78] T.K. GAISSER, Cosmic Rays and Particle Physics, Cambridge University Press, Cambridge, U.K. (1990).
- [79] M. AMBROSIO et al. (MACRO Collaboration), High statistics measurement of the underground muon pair separation at Gran Sasso, *Phys. Rev. D* **60**, 032001 (1999).
- [80] M. SPURIO et al., A parameterisation of the flux and energy spectrum of single and multiple muons in deep water/ice, *Proceedings of the 31st ICRC*, Łódź, Poland (2009), e-Print: [arXiv:0910.4259](https://arxiv.org/abs/0910.4259) [hep-ph].
- [81] M. BAZZOTTI (for the ANTARES Collaboration), Measurement of the atmospheric muon flux with the ANTARES detector, *Proceedings of the 31st ICRC*, Łódź, Poland (2009), e-Print: [arXiv:0911.3055](https://arxiv.org/abs/0911.3055) [astro-ph.HE].
- [82] I.A. BELOLAPTIKOV et al., The Baikal underwater neutrino telescope: Design, performance, and first results, *Astropart. Phys.* **7**, 263-282 (1997).
- [83] P. DESIATI, K. BLAND (for the AMANDA Collaboration), Response

- of AMANDA-II to Cosmic Ray Muons, *Proceedings of the 28th ICRC*, Tsukuba, Japan (2003).
- [84] G. CARMINATI et al., MUPAGE: a fast atmospheric MUon GEnerator for neutrino telescopes based on PArametric formulas, *Proceedings of the 31st ICRC*, Łódź, Poland (2009), e-Print: [arXiv:0907.5563](https://arxiv.org/abs/0907.5563) [astro-ph.IM]
- [85] J. VON NEUMANN, Various techniques used in connection with random digits, Monte Carlo Method, in A.S. Householder, G.E. Forsythe, and H.H. Germond, eds., National Bureau of Standards Applied Mathematics Series, N. 12 (Washington, D.C.: U.S. Government Printing Office, 1951): 36-38.
- [86] M. MATSUMOTO, T. NISHIMURA, Mersenne Twister: A 623-dimensionally equidistributed uniform pseudo-random number generator, *ACM Trans. on Modeling and Computer Simulation* **8**, 3-30 (1998).
- [87] H. GOLDSTEIN, *Classical Mechanics*, 2nd Ed., Addison-Wesley, Cambridge, MA, U.S.A. (1980).
- [88] J.A. AGUILAR et al. (ANTARES Collaboration), Zenith distribution and flux of atmospheric muons measured with the 5-line ANTARES detector, Submitted to *Astropart. Phys.*
- [89] C.G.S. COSTA, The prompt lepton cookbook, *Astropart. Phys.* **16**, 193-204 (2001).
- [90] E.V. BUGAEV et al., Prompt Leptons in Cosmic Rays, *Nuovo Cimento* **12**, 41-73 (1988).
- [91] C. GIUNTI, Neutrino flavour states and the quantum theory of neutrino oscillations, *J. Phys. G: Nucl. Part. Phys.* **34**, R93-R109 (2007).
- [92] Z. MAKI, M. NAKAGAWA, S. SAKATA, Remarks on the Unified Model of Elementary Particles, *Progr. Theor. Phys.* **28**, 870-880 (1962);
B. PONTECORVO, Neutrino Experiments and the Problem of Conservation of Leptonic Charge, *Sov. Phys. JETP* **26**, 984-988 (1968) [*Zh. Eksp. Teor. Fiz.* **53**, 1717-1725 (1967)].
- [93] C. AMSLER et al. (Particle Data Group), Standard Model and Related Topics, 13. Neutrino Mass, Mixing, and Flavor Change, *Phys. Lett.* **B667**, 163-171 (2008).
- [94] R. GANDHI et al., Neutrino interactions at ultrahigh energies, *Phys. Rev.* **D58**, 093009 (1998).
- [95] H.L. LAI et al. (CTEQ Collaboration), Improved parton distributions from global analysis of recent deep inelastic scattering and inclusive jet data, *Phys. Rev.* **D55**, 1280-1296 (1997).
- [96] J. PUMPLIN et al. (CTEQ Collaboration), New generation of parton distributions with uncertainties from global QCD analysis, *JHEP* **07**, 012 (2002).
- [97] S.L. GLASHOW, Resonant Scattering of Antineutrinos, *Phys. Rev.* **118**, 316-317 (1960).
- [98] R. GANDHI et al., Ultrahigh-energy neutrino interactions, *Astropart. Phys.* **5**, 81-110 (1996).
- [99] A. BOLT, *Inside the Earth*, Freeman, San Francisco, CA, U.S.A. (1982).
- [100] A. DZIEWONSKI, Earth Structure, Global, in: *The Encyclopedia of Solid Earth Geophysics*, David E. James ed., Van Nostrand Reinhold, New York, NY, U.S.A. (1989), as cited in [98].
- [101] G.J. FELDMAN, R.D. COUSINS, Unified approach to the statistical analysis of small signals, *Phys. Rev.* **D57**, 3873-3889 (1998).
- [102] G.C. HILL, K. RAWLINS, Unbiased cut selection for optimal upper limits in neutrino detectors: the model rejection potential technique, *Astropart. Phys.* **19**, 393-204 (2003).
- [103] M. ACKERMANN et al. (AMANDA Collaboration), Search for neutrino-induced cascades with AMANDA, *Astropart. Phys.* **22**, 124-138 (2004).
- [104] M. ACKERMANN et al. (IceCube Collaboration), Search for ultra-high-energy neutrinos with AMANDA-II, *Astrophys. J.* **675**, 1014-1024 (2008).

-
- [105] V. AYNUTDINOV et al., Search for a diffuse flux of high-energy extraterrestrial neutrinos with the NT200 neutrino telescope, *Astropart. Phys.* **25**, 140-150 (2006).
- [106] J. TIFFENBERG (for the Pierre Auger Collaboration), Limits on the diffuse flux of ultra high energy neutrinos set using the Pierre Auger Observatory, *Proceedings of the 31st ICRC*, Łódź, Poland (2009),
- [107] D.J.L. BAILEY, Genhen: Extension of “genneu” for high energy neutrino interactions, ANTARES-SOFT-2000-005.
- [108] D.J.L. BAILEY, KM3 v2r1: User Guide, ANTARES-SOFT-2002-006.
- [109] GEANT program manual, CERN program library long writeup W5013, CERN (1993).
- [110] M. DE JONG, The ANTARES Trigger Software, ANTARES-SOFT-2005-005.
- [111] M. DE JONG, The TriggerEfficiency program, ANTARES-SOFT-2009-001.
- [112] A. HEIJBOER (for the ANTARES Collaboration), Reconstruction of Atmospheric Neutrinos in Antares, *Proceedings of the 31st ICRC*, Łódź, Poland (2009), e-Print: [arXiv:0908.0816](https://arxiv.org/abs/0908.0816) [astro-ph.IM]
- [113] J. BRUNNER, The BBFit Reconstruction Algorithm, ANTARES-SOFT-2009-003.
- [114] F. JAMES, M. ROOS, Minuit - a system for function minimization and analysis of the parameter errors and correlations, *Comput. Phys. Commun.* **10**, 343-367 (1975).

Summary

This thesis is devoted to the search for a diffuse high energy neutrino flux through shower events with the ANTARES neutrino telescope which is taking data at a depth of 2475 m in the Mediterranean Sea. The main goal of ANTARES is the detection of high energy cosmic neutrinos produced in astrophysical objects such as Supernova Remnants, Active Galactic Nuclei and Gamma-Ray Bursts. A neutrino can be detected by measuring the Cherenkov light emitted by the charged particles produced after the neutrino interacts with the seawater or with the rock under the seabed. The amplitudes and arrival times of the light signals are measured by a three-dimensional array of 885 photomultiplier tubes, with a volume of approximately 0.01 km³.

Depending on the type of neutrino interaction, different secondary particles are generated resulting in different topologies. Muons induced by charged current muon neutrino interactions produce a track that can be considered as a straight line in space. Electron neutrinos induced by charged current electron neutrino interactions generate an electromagnetic shower. Neutral current interactions produce a hadronic shower. Both electromagnetic and hadronic showers can be considered as point-like light sources, because the spatial extension of the Cherenkov light they generate is significantly smaller than the typical size of the detector. Taking advantage of these topologies, shower events can be discerned from muon tracks.

In this thesis, an in-depth study of atmospheric muons has been done. Since the flux of these particles is about six orders of magnitude larger than the atmospheric neutrino flux, they represent the majority of the signal seen by a neutrino telescope. A Monte Carlo event generator of atmospheric muons, known as MUPAGE, has been developed from parametric formulae which reproduce the flux and the energy spectrum of underwater/ice atmospheric muons and take into account the multiplicity of muons produced in the same cosmic ray interaction. The main feature of MUPAGE relies on the tiny computing time – with respect to a full Monte Carlo generation – required to simulate a long period of active detector time. Since the generation is based on parametric formulae, the model of

primary cosmic rays as well as hadronic interactions in the atmosphere cannot be changed afterwards. Nevertheless, due to the importance of rejecting atmospheric muons in this study, Monte Carlo samples with larger livetime have been preferred to smaller samples with a more accurate reproduction of the atmospheric muon flux.

In the context of this thesis, selection criteria have been defined to reject the background signal due to track events. The expected isotropic rate for atmospheric electron neutrinos is determined as 0.37 events per year. Assuming a hypothetical cosmic electron neutrino flux of $E_\nu^2 \Phi = 10^{-7} \text{ GeV cm}^{-2} \text{ s}^{-1} \text{ sr}^{-1}$, 5.2 events per year are expected. The sensitivity to diffuse high energy neutrino flux through shower events at a 90% confidence level is

$$E_\nu^2 \Phi_{90\%CL} = 5.3 \times 10^{-8} \text{ GeV cm}^{-2} \text{ s}^{-1} \text{ sr}^{-1}$$

for one year of data taking in ANTARES, assuming a detector efficiency of roughly 80%. The central 90% of the E^{-2} signal lies between generated energies of $10^{5.2}$ and $10^{7.2}$ GeV.

The ANTARES detector is acquiring data in different configurations with a detector efficiency between about 56% and 88%. Taking into account these various setups, a more realistic estimate of the sensitivity for 335 days of detector livetime (from December 7th 2007 until December 31st 2009) gives

$$E_\nu^2 \Phi_{90\%CL} = 6.1 \times 10^{-8} \text{ GeV cm}^{-2} \text{ s}^{-1} \text{ sr}^{-1}$$

with the central 90% of the E^{-2} signal found between generated energies of $10^{5.3}$ and $10^{7.2}$ GeV.

With the study made in this thesis, the feasibility to detect diffuse cosmic neutrino flux which induces showers in the ANTARES neutrino telescope has been demonstrated as well as the competitiveness with the results obtained by other neutrino detectors.

Acknowledgements

L'essenziale è invisibile agli occhi.
Le Petit Prince - Antoine de Saint-Exupéry

Così sono anche i neutrini. E questo lavoro di tesi non sarebbe stato possibile senza l'aiuto di molte persone.

I primi ringraziamenti vanno sicuramente al gruppo di Bologna con cui ho avuto il piacere di trascorrere questi ultimi 5 anni. A Maurizio Spurio che mi ha sempre instancabilmente seguito, che mi ha insegnato come fare fisica e sempre mi ha incoraggiato a diventare indipendente, anche quando la strada era più ardua del solito. Grazie per aver sempre creduto nelle mie possibilità.

Ad Annarita Margiotta che sarà sempre il mio modello da seguire per l'equilibrio con cui affronta tutti i giorni l'essere donna e mamma senza sacrificare una carriera scientifica di successo. Grazie per tutti i momenti spesi insieme, dalle discussioni di fisica a quelle di vita vissuta.

A Giorgio Giacomelli per avermi trasmesso una parte della sua immensa conoscenza.

A Stefano Cecchini per le lunghe rasserenanti chiacchierate nel suo ufficio o in un ristorante a La Seyne-sur-Mer. Grazie per avere sempre avuto tempo per me nel tuo modo piacevolmente scherzoso.

A Marco Bazzotti, Simone Biagi e Tommaso Chiarusi miei prodi compagni di viaggio in questa lunga odissea chiamata dottorato.

I really want to thank the NIKHEF group for all the time I have spent in Amsterdam. Met name Maarten de Jong, hij heeft zeker een briljante geest. Bedankt dat je de tijd vond om samen met mij met de fysica te 'spelen' en om me altijd welkom te laten voelen.

I also want to thank the entire ANTARES Collaboration, because it has been a pleasure to work with you and spent such a nice time discovering physics as well as European towns. A special thanks goes to Jürgen Brunner for the endless suggestions he always gave to me. Du hast mir das Beste gesagt, dass ANTARES zu meinem Privatleben korreliert. Ich werde es nie vergessen.

Passando agli amici, che sono tanti e non possono essere tutti citati in poche righe, alcuni meritano una menzione d'onore. Inizierò da Letizia Tesei, impagabile amica nel

corso di tanti anni, certamente pieni di sacrifici ma pur sempre magnifici grazie a te.

A Leone Cavicchia che in questi ultimi mesi bolognesi si è preso cura di me come un fratello. Però, scusa, che tempo farà tra 30 anni? Dici che nevicata?

Aan Aart Heijboer, bron van inspiratie en gelach. Vergeet niet dat we nog samen moeten gaan zingen in de Casablanca.

To Corey Reed, with whom I am still walking downtown in Berlin, talking about nothing and everything. See you in LA, dude.

A Giulia Vannoni che non ha avuto paura a sostenere un'amicizia tra Bologna e Parigi, con fughe ad Amsterdam e a Firenze e con tutte le nostre notti brave in ogni città in cui finissimo per lavoro.

Al mio giovane ed inesperto fratellino Claudio Bogazzi di cui sono tanto fiera. Non basterebbero tutte le pagine di questa tesi per dirti quanto ti sono grata di tutti i nostri momenti insieme.

Ad Eduard Simioni che era con me nel momento in cui ho deciso di prendere in mano la mia vita, camminando su un sottile strato di ghiaccio. Tu per me sarai sempre mulini a vento visti con Lizzy.

All'Italian gang che ci ha incoraggiato tutte nei nostri primi mesi ad A'dam. A carina Serena Oggero che mi ha sempre dato tanta allegria e che con la sua folta bionda chioma 'tanto vale'. A carina Chiara Farinelli, mia infallibile spia con la sua celebre espressione da 'the importance of being'. Carine, i chilometri non ci separeranno mai.

Aan carino Gabriël Valentino Ybeles Smit, half Nederlands, half Duits, half Spaans en half Italiaans. Twee personen, een groot hart. Het is de tijd die we samen doorbrachten, op welke manier dan ook, waardoor onze vriendschap zo belangrijk en waardevol is.

Ad Elsa Callini semplicemente per come è. A Bologna, a Milano o a Pasadena sei sempre splendida.

A Federico Filippini che c'è sempre stato e sempre ci sarà perché un amico così ti capita una sola volta nella vita.

Aan mijn nieuwe familie, de Lims, die me verwelkomen als dochter of zus vanaf het allereerste begin. Ik ben zo trots om een nieuw familielid te zijn.

Alla mia famiglia che ormai si è rassegnata ad avermi sempre lontana da casa ma che è sempre vicina a me nel mio cuore. Grazie per avermi lasciato libera di seguire la mia strada, con bagagli pieni delle ottime cose che mi avete insegnato e senza paura di cadere.

Aan Gordon Lim omdat you are just too good to be true. Onze perfecte fit glinstert als het roze zand van onze geheime plek. Waar your heart is beating, amore, dat is de plek waar ik thuis ben.